Isolation and Characterization of Circulating Biomarkers to Predict Patient Outcomes in Late-Stage Non-Small Cell Lung Cancer

by

Emma Purcell

A dissertation submitted in partial fulfillment
of the requirements for the degree of
Doctor of Philosophy
(Chemical Engineering)
in the University of Michigan
2021

Doctoral Committee:

Professor Sunitha Nagrath, Chair
Professor Joerg Lahann
Professor Deepak Nagrath
Professor Nithya Ramnath
Professor Peter Tessier

Emma Purcell

eapurcel@umich.edu

ORCID iD: 0000-0003-4653-4756

Dedication

To Mom, Dad, Fran, and Charlie. Thank you for all the years of love and support.

Acknowledgements

First, I would like to thank my advisor, Dr. Sunitha Nagrath for all her support and guidance. I joined Sunitha's lab because of her infectious positivity and desire to help cancer patients and cannot be happier with that decision. She taught me how to be an independent researcher and mentor students, all while keeping a positive attitude and a smile on my face. I can never express how grateful I am for Sunitha's support to reach for my dreams.

I would also like to thank my committee- Dr. Deepak Nagrath, Dr. Peter Tessier, Dr. Joerg Lahann, and Dr. Nithya Ramnath for all their suggestions, feedback, and encouragement over the last five years. Your questions and comments have made me a better researcher and have given me the skills to critically approach my work and the work of my peers.

I would especially like to thank the mentors I have had over the years at Michigan, specifically Dr. Shruti Jolly and Dr. Nithya Ramnath. Your support and encouragement have been instrumental in helping me become the researcher I am. You have shown me how to be a dedicated, assertive women in science, while still being compassionate and empathetic, and I strive to hold your spirit for collaboration and mentorship through my career.

From the Department of Radiation Oncology, I would like to thank the amazing clinical coordinators, Jen Thomas, and Michelle Castle, without whom this research would not be possible. Additionally, thank you to Chris Maurino for keeping up the database of clinical information and answering all my questions. Thank you to Dr. Ted Lawrence, Dr. Kyle Cuneo, and Dr. Caitlin Shonewolf for the research guidance and clinical perspective on my research.

I would like to thank the members of the Bailey lab for their amazing collaboration on the droplet microfluidic CAR-Wash project. Thank you to Nico Mesyngier for listening to my crazy ideas and connecting us with Claire Cook. Many thanks to Dr. Ryan Bailey for his encouragement to pursue this project cooked up by students. Finally, I am so grateful to have worked with Claire Cook, CAR-Wash expert, and collaborator extraordinaire.

I also would like to thank the amazing core facilities at the University of Michigan and all the help and support they have provided. Special thanks go out to Pilar Herrera-Fierro, Kevin Owen, and Sandrine Martin at the Lurie Nanofabrication Facility. Also, a big thank you to The Advanced Genomics Core and the Bioinformatics Core, with a special thanks to Rebecca Tagett for her guidance and patience with our microarray analysis.

I would like to acknowledge my funding sources, primarily the NIH T32: Microfluidics in Biomedical Sciences Training Program (MBSTP) at the University of Michigan.

I would like to thank the members of the Nagrath Lab, both current and past, for all the guidance, help, and good times had. I'd like to thank Dr. Molly Kozminsky, Dr. Ting-Wen Lo, Dr. Mina Zeinali, and Dr. Yoon-Tae Kang for their training and mentorship. To Zeqi Nui, Heather Fairbairn, Maddy Grzeski and the rest of the GO Chip team, there is no one I would have wanted to work with more than you. To the amazing students who I have had the privilege of working with and mentoring: Jess Jana, Abbie Radomski, Anna Kaehr, Maddy Grzesik, Nayri Carman, Carly Prast, I will miss our shenanigans and thank you for all the work you have done.

Graduate school was both challenging and rewarding, and I would not be where I am today without my amazing friends. Alex Adams, Kaylee Smith, Brittany Rupp, Dr. Sarah Owen, Zeqi Niu, Elizabeth Wilson, Cailin Buchanan, thank you for the support and fun through the last five years.

Table of Contents

List of Tables

List of Figures

Abstract

This work hypothesizes that the molecular characterization of extracellular vesicles (EVs) and circulating tumor cells (CTCs), biomarkers found in peripheral blood draws, can be used to monitor, and predict, treatment efficacy and patient outcomes in lung cancer.

First, microfluidic EV isolation technologies were developed, and EV protein characterization assays were adapted for use with these technologies. Isolation strategies included (1) Annexin V-phosphatidylserine binding to capture tumor-derived EVs on the device surface and (2) isolating natural killer (NK) cell-derived EVs by first capturing NK cells followed by on-chip EV biogenesis. Western blot protein analyses were optimized for these technologies to verify the presence of EV-specific proteins (CD9, FLOT1, HLA-C) along with cell type-specific proteins (CD56). Finally, the DICE device was developed to both isolate EVs and characterize select EV-Proteins (CD9, Vimentin, EGFR) on-chip.

Building off the developed EV characterization methods, EGFR mutations were detected longitudinally in both EV-RNA and EV-Protein from 10 metastatic NSCLC patients. For these patients, identifying the presence of sensitizing (exon 19 del, L858R) and resistance (T790M) EGFR mutations informs sensitivity to tyrosine kinase inhibitors. We demonstrated the presence of exon 19 del and L858R mutations within EV-Protein, marking the first study that demonstrates the presence of these mutations in patient-derived EVs. At the EV-RNA level, exon 19 del mutations were detected in 88% (n=7/8) patients and an increase in mutation burden mirrored disease progression and a decrease mirrored stable disease in 100% (n=5/5) of patients and in 86% (n=12/14) samples. We additionally profiled 2 patients for L858R and T790M

mutations, however the detection was more modest at 60% (n=6/10) and 30% (n=3/10) samples, respectively. As such, EV-RNA exon 19 del mutation burden has the potential to inform treatment decisions in a subpopulation of metastatic NSCLC patients.

In a cohort of 26 stage III NSCLC patients, CTCs were isolated from all 26 patients using the microfluidic graphene oxide (GO) chip at six timepoints during radiation and immunotherapy therapies. Significantly, it was found that having a decrease in CTCs of less than 75% between pre-treatment and week 4 of radiation therapy is predictive of significantly shorter progression free survival time, 7 months vs 21 months stable monitoring time (p=0.005, log-rank test). Additionally, evaluation of PD-L1 expression on the CTCs demonstrated that having a higher proportion of PD-L1 CTCs before starting treatment was a potential indicator of metastatic potential (p=0.057, log-rank test). Finally, microarray mRNA analysis demonstrated that CTCs develop a more aggressive, proliferative phenotype during radiation treatment.

Finally, to assess the heterogeneity of EV biogenesis for applications in NK-EV therapeutics, the droplet microfluidic CellMag-CARWash system was adapted to isolate single NK-92MI cells bound with anti-CD56 Dynabeads. It was found that the CellMag-CARWash isolates cells that have 3+ Dynabeads attached, with an overall efficiency of 58% ± 7 (n=4), while calculations indicate that 1.8 beads should be needed to isolate cells. From a mixed cell population, the CellMag-CARWash isolated NK cells with 95% ± 2 (n=4) purity, achieving an isolation efficiency of 42% ± 14 (n=3). Prolonged droplet stability was demonstrated, and cell viability is 50% after 24 hours in droplets.

Taken together, these technological advancements represent necessary developments to move liquid biopsies from the lab to the clinic. These novel isolation and characterization strategies will need to continue to be tested in pilot cohorts and validated in larger cohorts.

Chapter 1 Introduction

1. 1 Non-small cell lung cancer (NSCLC)

Approximately 190,000 people were diagnosed with non-small cell lung cancer (NSCLC) in 2020. While localized, NSCLC has a survival rate of 63% and while regional, the survival rate is 35%, however when the cancer becomes metastatic the survival rate drops to 7%.[1] Personalized, precision treatment will revolutionize the way we treat cancer, allowing each patient to receive only the treatments most likely to lead to positive outcomes. Having highly personalized, precise treatments are particularly critical in lung cancers when patients most often are diagnosed with late-stage disease because early symptoms are mistaken for infection or effects of previous years of smoking.

Current first line treatment for unresectable stage III, NSCLC patients is combination chemotherapy and radiation treatment, **Figure 1-1.**[2] Recent advancements have led to the use of antibodies against programmed death ligand 1 (PD-L1) as a checkpoint inhibitor to stop the deactivation of T-cells associated with PD-1-PD-L1 interactions.[3] The PD-1 cascade is the body's pathway to turn off CD8 T-cells after their activation as a part of an immune response. Tumors, however, have high presentation PD-1, resulting in the inactivation of the very T-cells that would kill the tumor cells.[4] In 2017, the PACIFIC Trials demonstrated that providing durvalumab, anti-PD-L1+ immunotherapy, following chemoradiation in stage III NSCLC patients led to an increase in progression free survival time from 5.6 months for patients receiving placebo to 16.8 months for patients receiving durvalumab.[5] However, there is little

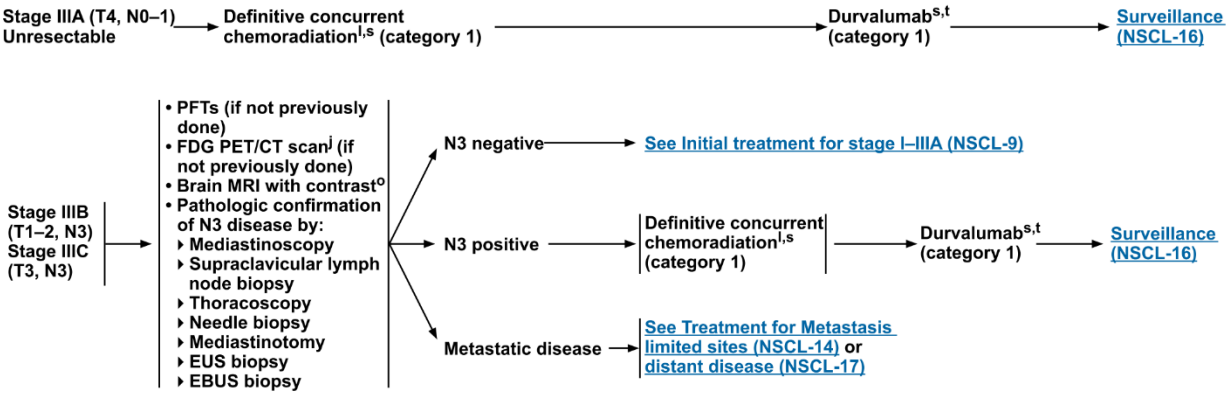

Figure 1-1 Flowchart for unresectable stage III NSCLC treatment from National Comprehensive Cancer Network Guidelines Version 3.2020 Non-Small Cell Lung Cancer

understanding as to which patients will benefit from durvalumab, as the PD-L1 expression on the primary tumor is not taken into account.

In metastatic, or stage IV, NSCLC, patients qualify for targeted therapies if their primary lung tumor has specific mutations in the epidermal growth factor receptor (EGFR) or, less commonly, ALK, ROS1, or BRAF, **Figure 1-2.**[2] Three EGFR targeting drugs are a set of small molecules termed tyrosine kinase inhibitors (TKIs), targeting tyrosine kinases, the class of enzyme to which EGFR belongs. These drugs, however, are either only effective or are

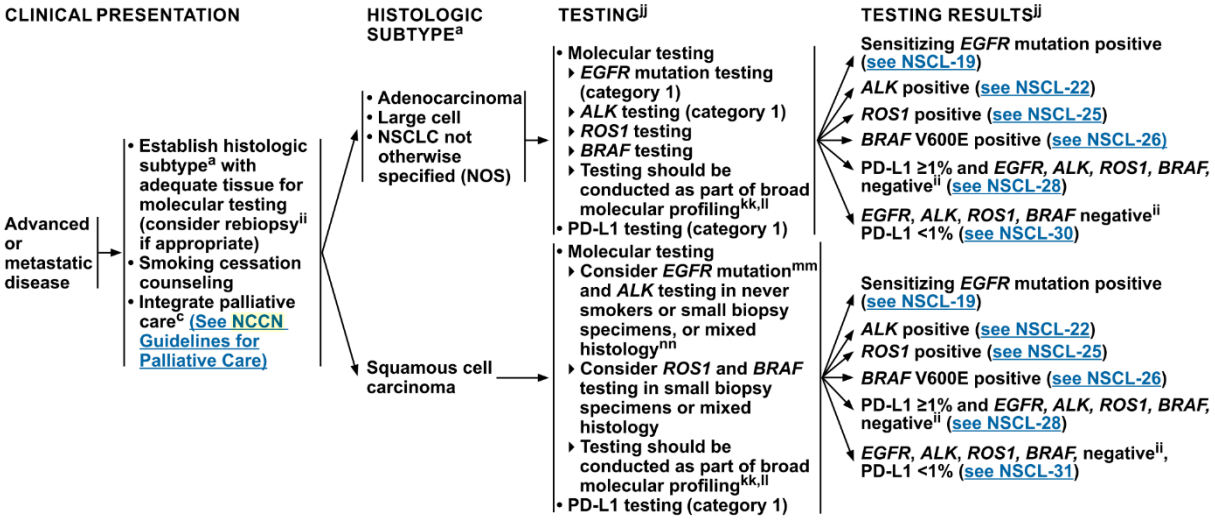

Figure 1-2 Flowchart for stage IV NSCLC treatment from National Comprehensive Cancer Network Guidelines Version 3.2020 Non-Small Cell Lung Cancer.

significantly more effective if the tumor has specific EGFR mutations, such as an exon 21 L858R substitution mutation or an exon 19 deletion.[6] For patients on the common targeted therapies erlotinib and gefitinib, drug resistance occurs in as little as nine months, with over half of those resistances coming as a result of the T790M mutation.[7–9] In 2015, the FDA approved osimertinib, a third generation TKI therapy for patients who already have T790M mutations in their EGFR. Resistance, however, still occurs in the form of another acquired mutation in exon 20, C797S.[10]

In both stage III and stage IV NSCLC, there is a critical need for precise knowledge of a patient's tumor to allow for the best possible treatment plans. In stage III, current treatment is not based on molecular information of the patient's tumor, and there is an urgent need to determine which patients will benefit from the current standard treatments. Conversely, in stage IV, there are a myriad of treatment options based on the molecular profile of the tumor, however, monitoring methods, including tumor biopsy, are minimally repeatable, which means treatment can not accurately reflect changing tumors.

1. 2 Liquid Biopsy: the role of biomarkers in NSCLC

Monitoring and molecular characterization of patients' disease allows clinicians to determine the best treatment options. Many groups have proposed a liquid biopsy to identify a biomarker in a peripheral blood draw which would be used for the early diagnosis and monitoring of cancer. Several potential targets have been identified for such a liquid biopsy, the most common of which are circulating tumor DNA (ctDNA), circulating tumor cells (CTCs), and extracellular vesicles (EVs).[11,12,13] Information about CTCs and EVs can be found in detail below, but briefly, ctDNA is a subset of cell free DNA that has been shed from the primary tumor to circulate in the bloodstream. ctDNA is mainly released by apoptotic or necrotic tumor

cells and contains the genetic signature, including mutations, of their cancer cells of origin.[14,15] Elevated DNA fragment concentrations have been observed in the blood of cancer patients, suggesting that this metric may be useful for diagnosis.[16] However, to precisely predict tumor behavior, assess treatment efficacy, and determine mutational load, it is necessary to determine the proportion of aberrant vs. wild-type DNA and thoroughly characterize the tumor-derived DNA.[17] Additionally, because ctDNA is shed primarily by dying cells, ctDNA may not be shed from the most aggressive, invasive, or treatment resistant cells.

We hypothesize that the molecular characterization of biomarkers, found in a simple peripheral blood draw, can be used to monitor, and predict treatment efficacy and patient outcomes in lung cancer. It is critical that we develop highly specific, accurate, low-cost testing techniques to allow for repeated testing and continued monitoring of NSCLC patients.

1.2.1 Extracellular vesicles (EVs)

The first biomarker of interest, extracellular vesicles (EVs) are group of nanovesicles, approximately 50-1000nm in diameter, that are released into the blood stream through exocytosis.[18] While several subtypes of EVs that have been discovered, clear nomenclature is still being developed in the field.[19] One of the most common subtypes, exosomes, have been recently renamed as smallEVs, sEVs, or simply EVs as defined by a specific size range of 50-200nm for particle sizes.

EVs are uptaken by distant cells after excretion, allowing for cell-cell communication and the transfer of cellular information.[20–22] EVs have been found to play many roles in normal cellular communication, as well as in cancer. One of these roles is inhibiting normal immune response to allow for tumor growth or immune evasion.[18] It has been demonstrated by Liu et al. in mice that EVs have the ability to increase tumor growth by inhibiting the cytolytic function of

natural killer (NK) cells.[23] EVs have also been shown to mediate CD8+ T cell apoptosis through the expression of the Fas ligand, providing another route for tumor immune evasion.[24] In addition to immune cell evasion, EVs have been implicated in the formation of the pre-metastatic niche. Costa-Silva et al. found that pancreatic ductal adenocarcinoma (PDAC) derived exosomes induced liver pre-metastatic niche formation in mice, followed by increased liver tumor burden. This cascade began with uptake of PDAC EVs by Kupffer cells, a macrophage in the liver, which caused the excretion of growth factors and the upregulation of fibronectin.[25]

A second up-and-coming area of EV research, EV engineering for drug delivery, hasled to many groups developing novel EV engineering solutions to deliver standard anti-tumor drugs, such as chemotherapies or immunotherapies.[26] For example, EVs extracted from NSCLC cells were embedded with doxorubicin (DOX), a well-known chemotherapy, and conjugated with gold nanoparticles. These 'nanosomes' were used to deliver drugs to lung cancer cell lines and non-tumorigenic lung fibroblasts. Compared with free DOX delivery, the nanosomes had higher toxicity against cancer cells, while the effects of DOX on healthy cells were reduced[27]. One group developed hyaluronic acid functionalized extracellular vesicles using lipid-grafting that are loaded with DOX to overcome multidrug resistance in breast cancer cell lines.[28]

EVs have also been recently used to deliver novel therapeutics, including siRNA and CRISPR/Cas-9 to specifically induce cell death *in vivo* and *in vitro,* respectively.[29,30] Modifying the exosomal surface, in addition to loading a therapeutic agent, allows researchers to target specific organs or cell type, such as the brain.[31] One group genetically modified EVs to express a cardiac-targeting peptide on the surface, which increased EV delivery and uptake in the hearts of mice.[32] A final therapeutic target for EV delivery are miRNAs.[33] An exciting application of miRNA delivery is the potential to treat therapy-resistant tumors; it was found that delivery of

miR-21 inhibitor in conjunction with chemotherapy using engineered EVs reversed drug resistance in chemoresistant colon cancer cells.[34]

Engineered EVs can either originate from cell culture cells, or donor cells from either patient or a specifically matched donor. Recently, groups have begun looking to other sources of EVs such as EV-like nanosomes derived from edible plants, because of their safety without the challenges of using human-derived EVs.[35] These vesicles are isolated using ultracentrifugation with density gradient, loaded with therapeutics, and then validated using mouse models by delivering the nanosomes orally or intravenously.[36] One group used grapefruit-derived nanovesicles to deliver chemotherapy and anti-inflammatory drugs and coated nanovesicles with activated leucocyte membranes to enter inflammatory sites.[37]

Despite their promise, therapeutic applications of EVs are in the very early stages of development, and thus far, low production, purification, and recovery rates have hindered their widespread appreciation.[38] To see EVs adopted in the clinic, it will be critical to thoroughly validate the methods for EV delivery and loading while further characterizing the off-target effects.

Finally, EVs contain proteins, miRNA, mRNA, and DNA fragments, which play a role in the transfer of information from parent cell to distant cells.[39] However, this also allows EVs to be used in diagnostic and prognostic assays, as they carry molecular cargoes from their cells of origins. Several groups have determined specific miRNA and protein compositions in EVs that have potential as diagnostic markers for non-small cell lung cancer. For example, in a cohort of stage I and II adenocarcinoma patients, there were similar signatures between exosomal miRNA and miRNA from the primary tumor. Additionally, it was found that from a peripheral blood

draw, cancer patients had an exosomal concentration of 2.85 mg/mL compared to only 0.77 mg/mL in a comparable healthy control group.[40]

While EVs offer the potential to indirectly profile their cells of origin, they can be challenging to isolate and characterize because of their size. For EVs to become clinically relevant, isolation workflows need to be developed that yield highly pure EVs and allow for highly sensitive downstream applications.

1.2.2 Circulating tumor cells (CTCs)

A second common biomarker, circulating tumor cells (CTCs) are cells shed from primary tumors that circulate in the bloodstream and may extravasate into peripheral locations in the body, causing metastasis.[41] CTCs are incredibly rare cells, frequently only 10-100 per mL of blood, making it challenging to isolate and interrogate them. CTCs contain proteins, miRNA, and RNA that can be quantified, allowing for understanding of the originating tumor.[42] It has been found for many cancers, including non-small cell lung cancer, that quantity of CTCs as well as contents of CTCs, such as mRNA and miRNA can be correlated to progression-free survival, overall survival, and disease stage. [42–45] For example, in metastatic breast cancer, it was found that patients with fewer than 5 CTCs per 7.5 mL of blood had a better prognosis than their counterparts with higher CTC counts.[42] CTC isolation technologies have advanced rapidly since the discovery of CTCs in the 1960s, although the FDA has only approved one technology, CellSearch™, for clinical use. For research purposes, immunoaffinity microfluidic devices, inertial microfluidic devices, filtration, magnetic sorting and many other methods have been developed allowing for increased characterization opportunities.[11]

Ultimately, there are many different biomarkers that could be used to populate a liquid biopsy for the early detection or characterization of cancers. Although there have been many

advances in technologies for CTC isolation and characterization that have allowed them to start to gain traction in clinical settings, the clinical applications of EVs are still in the early stages of discovery.

1. 3 Extracellular vesicle (EV) isolation and characterization strategies

1.3.1 Conventional isolation strategies

Conventional EV isolation strategies include differential ultracentrifugation (UC),[46] UC paired with density gradient,[47] filtration,[48,49] size exclusion chromotagraphy,[50] and polymer precipitation kits.[51] These methods are known to have different compatibility with downstream assays. For example, UC without a gradient has been shown to have lower EV yield, but high purity when performing protein analyses compared with polymer precipitation methods.[52] Conversely, polymer precipitation kits have been shown to lead to high contamination but also high yield of small RNAs compared to UC.[47,52] Conventional strategies have many common challenges, including yield, purity, specificity, cost of machinery, and processing time.

1.3.2 Microfluidic EV isolation technologies

There is great interest in the development of microfluidic-based platforms for EV isolation and profiling to address many of the challenges of conventional isolation strategies. These technologies commonly take one of two forms: (1) on-chip EV isolation followed by off-chip EV characterization or (2) on-chip EV isolation along with on-chip EV profiling. These two types of technologies have different uses and applications. For example, on-chip analysis is commonly used to profile EVS for a small panel of proteins or RNAs, whereas off-chip analyses allow for high-throughput assays such as RNA-seq or proteomics.

Technologies that feature on-chip isolation and characterization have become more common in recent years, but they are still much less common than purely isolation devices. The benefit of this type of device is in their potential ease of use along with decrease loss of sample during sample process. In one example, Wu et al. deployed a novel nanomaterial and microfluidic based EV characterization technology coined "templated plasmonics for exosomes (TPEX)."[53] In this method, samples were introduced into the device, followed by incubation and dual labeling of samples with fluorescent aptamers and gold nanoparticles. After the development of in situ gold nanoshells, changes in fluorescence intensity and absorbance signal are monitored. For in situ profiling of EV markers, EVs derived from six cancer cell lines were spiked into human serum, and analyzed the expression of CD63, CD24, MUC1, and EpCAM. The output from the TPEX compared to conventional ELISA showed to be a better match to pure exosomes. In a second, unique approach to on-chip EV analysis, Liu et al. introduced their droplet-based single-exosome-counting enzyme-linked immunoassay (droplet digital ExoELISA).[54] Their device encapsulates antibody-conjugated bead complex with exosomes inside a mineral oil droplet. After incubation, an enzyme reporter on catalyzes the substrate (fluorescein-di-β-D-galactopyranoside) and produces a fluorescent signal, leading to the quantification of a single exosome. As the output result of clinical samples from this device is in accordance with other studies, it has been proposed that it can be used as diagnostic device.

EV capture on-chip followed by off-chip characterization is still the most common strategy for EV analysis. Immunoaffinity-based approaches are the most frequent methods used in these devices for EV capture. These technologies capture EVs on a surface based on the presence of specific EV-proteins or lipids. The substrate for isolation can be either magnetic beads or internal surfaces functionalized with antibodies or aptamers targeting exosomal markers

like CD9,[55] EPCAM,[55–58] CD63,[57–61] CD81,[62] phosphatidylserine (PS),[63] and other markers.[64] For example, Hisey et al developed a device using anti-EpCAM and anti-CD9 coated onto herringbone structures to isolate and release exosomes from ovarian cancer.[55] Their results show a nearly 5-fold higher yield compared to UC. A common challenge of these technologies is that it can be problematic to remove EVs from the device, such as would be necessary to perform functional studies.

Microfluidics offer exciting platforms for EV isolation and characterization. However, it is critical to thoroughly validate these novel technologies. Because of their small size and low cargo concentrations, EV characterization methods following isolation using microfluidics need to have high sensitivity.

1.3.3 Unmet need for approaches to characterize EVs

The number of EV isolation and characterization workflows have skyrocketed in the last number of years. However, for these assays to become clinically relevant, it is critical to thoroughly characterize the isolated EVs. While EV classification has become an active area of research in recent years, there is still much debate about how the field classifies different populations of vesicles. Of the EV excreted by cells, exosomes or sEVs are 50-200 nm in diameter, whereas microvesicles or apoptotic bodies are larger, >500nm.[65] Other identifying features of different EV subtypes are their cargo, including RNA, DNA, proteins, and other molecules. Commonly, EVs between 50-200 nm are isolated and tested for purity as defined by a series of characterizations, including morphology, size, concentration, and protein composition.[66]

The most frequent methods to probe EV morphology and overall purity are microscopy-based, including atomic force microscopy,[67] transmission electron microscopy,[68] and field

emission scanning electron microscopy.[67] These assays are looking to find EVs that are spherical in shape and of a consistent size—finding vesicles of a wide range of sizes can indicate less pure isolations. Additionally, imaging scans can show other contaminants like protein aggregates, which are common in poorly isolated EVs.

To study EV size distribution, optical methods such as dynamic light scattering and nanoparticle tracking analysis (NTA) are performed.[69] The most common tool to perform NTA is the Nanosight technology (Malvern), however the ZetaView (Particle Metrix) has become more popular recently. These technologies are based on measuring the size and concentration of nanoparticles based on their Brownian motion. The Nanosight has been found to yield more accurate particle sizes, whereas the ZetaView yields a more accurate and repeatable particle concentration.[70]

Finally, researchers need to demonstrate the presence of specific proteins to validate purity and type of vesicles isolated.[19] These assays look for specific sets of proteins, including elevated expression of several tetraspanins (CD9, CD63, CD81) to demonstrate the presence of EVs. Additionally, EVs need to be probed for cell type-specific proteins along with secondary and tertiary EV purity proteins. Protein analysis is frequently achieved through antibody-based assays like ELISA and western blotting.[69] These assays need fairly high protein concentrations, which can be challenging to achieve from EVs. It is critical to validate all EV-protein workflows for novel isolation devices to ensure that the isolated EVs are pure and of the correct size and morphology.

1.3.4 Downstream strategies for EV profiling

Outside of determining the presence and purity of exosomes in a sample, common downstream applications of EV isolation include RNA,[40,71,72] DNA,[73] protein,[74,75] and metabolite

profiling.[76] RNA characterization is commonly performed using reverse transcription-qPCR, microarrays, or RNA-sequencing. While standard protein profiling techniques are commonly used, increased technological capacities have led to a rise of flow cytometry-based profiling techniques.[77] Other proteomics strategies such as sodium dodecyl sulfate-polyacrylamide (SDS-PAGE) gel electrophoresis followed by liquid chromatography-tandem mass spectrometry (GeLC–MS/MS),[78] and matrix-assisted laser desorption ionization time-off-light (MALDI-TOF),[79,80] have become more prevalent.

While many novel applications and profiling techniques are being developed for EVs, many of these techniques have yet to be applied to microfluidic isolation workflows. There is a need to validate many of these more complex analysis methods in conjunction with microfluidic EV isolation to ensure the EVs and EV cargoes are not damaged during isolation or isolated in too low of a quantity for downstream use.

1. 4 EVs as potential biomarkers for NSCLC

As previously stated, EVs originate from all cell types—including tumor cells. These tumor derived EVs have been suggested as biomarkers for cancer by many groups. EVs are profiled largely for two purposes, diagnostics, and prognostics (or treatment monitoring). For clinical diagnostic and prognostic studies, various EV metrics have been proposed, ranging from the quantity of EVs to the presence of specific cargoes within the EVs. A critical benefit of EVs compared to circulating tumor DNA (ctDNA), another common biomarker, is their various cargoes; where ctDNA is restricted to DNA analyses, EVs carry an array of cargoes, including RNA, DNA, protein, and lipids.[81] Identifying specific molecular targets within EVs will allow clinicians to monitor patients non-invasively while also providing highly personalized treatment.

Finally, EVs are significantly more stable in blood compared to ctDNA, allowing for ease of study and fewer storage restrictions.[82,83]

1.4.1 Cancer prognostics

Using EVs for prognostics can be challenging, as there are currently no ways to isolate purely TDEVs. As such, researchers commonly look for molecular signatures found within the EVs to predict patient outcomes or treatment efficacy. miRNAs are the most commonly profiled EV marker for prognostic and treatment monitoring applications; specific miRNA signatures being predictive of worse survival in lung[84], liver[85,86], colorectal[87], glioma[88], and prostate[89] cancers. miRNA abundance and expression have also been found to be diagnostic compared to healthy controls; lung cancer patients had dramatically higher miRNA expression[40] and unique signatures[90] compared to a healthy populations. Prognostic signatures of EV-mRNA or other long RNA have been shown to be predictive of worse survival in several cancers including NSCLC,[91] and HCC.[72] EVs have also been suggested for diagnostic assays for specific tumor genotypes; Manda et al. developed a PCR assay to detect EGVR-VIII in high-grade gliomas in serum exosomes.[92]

Similarly, EV proteins have been suggested for diagnostic and prognostic assays in many cancers including lung[93,94], breast[95], and pancreatic[96] cancers. For example, one study used a sandwich-ELISA (enzyme-linked immunosorbent assay)-based assay and defined a 30 marker-panel to distinguish late stage patients with NSCLC from a healthy population.[97] Similarly, a pilot study analyzed EV protein surface markers to measure chemotherapeutic responses in women newly diagnosed with breast cancer.[98] Sanfeld-Paulsen et al. used their previously developed Extracellular Vesicle Array to capture exosomes using antibodies printed in an array on epoxy-coated slides from 276 different patients with NSCLC. They then quantified the

number of exosomes captured by each antibody to cite surface protein expression in the given sample of exosomes. They found 100% of patients in their cohort expressed common exosome markers CD9 and 81, but more interestingly they found one surface marker that showed correlation with overall survival, CD171.[93,97] Although potentially interesting, this outcome has not been validated.

1.4.2 Treatment response and resistance monitoring

In addition to prognostic studies, EV have been profiled to monitor specific therapies and resistance, such as chemotherapy, radiation, and immunotherapies. In a cohort of 203 NSCLC patients, miR425-3p was identified using HiSeq to differentiate between platinum chemotherapy resistant and sensitive patients.[99] Similarly, profiling of EV cargoes has been shown to predict chemoresistance in CRC.[100] Profiling mRNA in EVs is especially useful to monitor immunotherapy targets, such as PD-L1 or KRAS. In a cohort of melanoma and NSCLC patients, a high presence of PD-L1 in EV RNA correlated to a complete response for patients on anti-PD-1 antibodies.[101] This group used the exosome RNA extraction kit exoRNeasy (Qiagen), which first binds exosomes to exoEasy spin columns and then extracts RNA from the bound vesicles using Qiazol.[101] This result is extremely promising, implying that using EVs from plasma as an early response marker is feasible. However, one immediate problem with this method is that digital PCR is incredibly low throughput, only allowing for the measurement of eight samples at a time.

Indeed, EV analysis is a potential tool for early cancer diagnosis, effective treatment decision making, and monitoring treatment responses, all of which will increase survival rates. The main challenge facing the clinical application of exosomes resides in understanding the

mechanisms that regulate their heterogeneity, as changes in TDEs contents can impact the reproducibility of diagnostic outcomes.

1. 5 CTC isolation technologies

1.5.1 Commercially available isolation methods

Currently, the only FDA approved CTC isolation technology is CellSearch™, a system that uses a ferrofluid tagged with antibodies against the epithelial cell adhesion molecule (EpCAM) to magnetically sort EpCAM positive cells. Briefly, CellSearch™, is a highly standardized technology that has been used to enumerate CTCs in large cohorts of breast[102,103], metastatic colorectal[103], prostate, and lung cancer patients. CellSearch™ enumerates CTCs based on several metrics, including size, morphology, and the expression of specific proteins. CTCs are classified as having a clear nucleus using DAPI staining, along with being cytokeratin (CK) positive and CD45 negative using immunofluorescence.

Although CellSearch™ paved the way to use CTC in clinical settings, there are several downfalls to this technology, especially for use in lung cancers. It has been shown in several studies that CellSearch™ enumerates low numbers of CTCs from lung cancer patients, with several studies finding CTCs in only ~30% of patients. [104,105] One reason for this finding is that EpCAM is not expressed in 21.3% of primary lung tumors, indicating that there is a substantial population of CTCs that would be missed if isolating using EpCAM alone.[106] Finally, the CellSearch™ equipment is expensive and requires immediate processing, creating a high barrier to entry for CTC studies.

1.5.2 Microfluidic isolation technologies

A second broad category of CTC isolation technologies are microfluidics, which take advantage of either physical properties of CTCs or protein expression on CTCs for isolation through immunoaffinity capture.[107] The first group, technologies that use physical properties of CTCs, are frequently label-free technologies, which offer the benefit of returning an untouched pool of CTCs. These technologies rely commonly on the different size of CTCs (15-20μm) compared to white blood cells (WBCs, 8-12μm) to isolate pure CTCs. Examples of this type of technology include the Labyrinth[108,109], the Vortex chip[110], and filtration based microdevices.[111] While these technologies allow for a wide array of downstream applications, including functional studies, they tend to have low purity and have a high chance of clogging, both of which are detrimental to the use of CTCs in clinical settings.

An alternative, and more commonly used, approach is immunoaffinity microfluidic devices that perform either positive or negative selection for antibodies found on cells of interest. The first immunoaffinity device, the CTC Chip, was developed in 2007 and used pillar structures etched in silicon and functionalized with anti-EpCAM to isolate CTCs from NSCLC patients.[112] This technology captured an average of 155 CTCs/mL compared to the average of 60 CTCs/mL isolated by CellSearch in a collective study of prostate, lung, breast, ovarian, and colorectal cancers.[113] Following the advent of the CTC Chip came modifications to the original design including adding chaotic micromixers in the form of a Herringbone device that increases the number of collisions between cells and the antibody-coated device surfaces.[114] These devices are ideal for CTC capture because the length scale afforded is similar to that of surface features on cells, allowing for highly specific probing of targeted cells. Other common immunoaffinity

microfluidic CTC isolation technologies include the Oncobean Chip[115], MagSweeper[116], and the CTC-iChip[117].

1.5.3 Graphene oxide (GO) chip

The addition of nanomaterials into immunoaffinity microfluidic devices has increased their yield and specificity. An excellent example of such a device is the graphene oxide (GO) chip that uses GO monolayers that have self-assembled onto a gold-patterned surface and are then functionalized to allow antibody presentation through Neutravidin-biotin interactions.[118] The capture efficiency of the device was originally reported to be 87% and the surface chemistry allows for the conjugation of any biotinylated antibody of interest, allowing the device to be used across many cancers. Additionally, due to the large number of active sites, cocktails of antibodies can be used on the same device, allowing for the capture of cell populations that would otherwise be missed by using only one capture antibodies. This was demonstrated with high efficacy in a cohort of stage I-III NSCLC patients, where CTCs were captured using anti-EPCAM, anti-CD133, and anti-EGFR (epidermal growth factor receptor).[119] In this study CTCs were detected in all 13 patients and at all 38 timepoints.

The GO has been applied to numerous studies, demonstrating the efficacy of this device to isolate CTCs[118–122]. An additional benefit of the GO chip is the ability to perform downstream RNA characterization. On-chip RNA extraction followed by off-chip RNA purification and analysis was performed in studies of CTCs from lung[119], prostate[122], and breast[123] cancer patients. In the first two GO Chip studies, the RNA analysis was performed using the highly multiplexed Biomark (Fluidigm), which performs RT-qPCR on 96 samples for 96 unique genes, while the third used an 18-gene PCR panel. Both Biomark studies were able to generate interesting RNA profiles, however this type of analysis would not be sufficient for exploratory

studies. Additionally, RNA from CTCs is found to be of a lower quality, making characterization even more challenging. There is a need to develop protocols and workflows for post-capture CTC-RNA characterization for discovery-based studies.

1. 6 CTCs as biomarkers in NSCLC

As previously stated, CTCs make an outstanding potential biomarker in NSCLC because they allow you to directly profile the tumor of origin. CTCs have been shown to be useful as both diagnostic and prognostic biomarkers in numerous cancers.

1.6.1 Diagnostics

Although CTCs are not currently used in clinical NSCLC diagnosis, many CTC metrics that have been measured in research settings have shown diagnostic potential. The most common of these are enumeration, mRNA, DNA mutations, miRNA, and protein expression. Several groups have reported that CTC counts were elevated in patients with NSCLC compared to healthy controls, and also that CTC counts decreased when the patients began radiation therapy.[45,124,125] In addition to CTC enumeration, gene expression profiling could be a potential for lung cancer diagnostics. Hayes et al. looked at 51 tumors and 13 healthy controls to determine genetic markers for each of the types of lung cancer. For example, genes ASH1 and HMGB3 indicated adenocarcinoma with L587S, CLCA2 and HMGB3 determining squamous carcinomas.[126] If these markers could be found in CTCs, that would represent the ability to diagnose specific subtypes of lung cancer.

1.6.2 Prognostics and treatment monitoring

In addition to disease diagnosis, CTC contents have been analyzed and several prognostic markers have been discovered. Chen et al. measured cytokeratin 19 (CK19) mRNA in CTCs

before and after radiation through reverse transcription PCR (RT-PCR). They found that patients with CK19 expression after radiation had overall poorer survival and progression-free survival compared to patients with negative CK19 mRNA expression.[127] Another group performed a large-scale analysis using the National Cancer Institute-Cancer Genome Anatomy Project database to identify a panel of four genes that could be used together to predict prognosis and treatment efficacy. These genes are KRT19, ubiquitin thiolesterase, a gene highly similar to HSFIB1 for fibronectin, and TRIM 28.[128]

CTCs have also been interrogated for their mutation status and compared to both cfDNA and original tumor. In 2008, CTCs isolated from NSCLC patients were tested using allele specific PCR for EGFR mutations. T790M mutations were found in 11 of 13 patients compared to only finding the mutation in 4 of 12 patients free plasma DNA, with a positive T790M mutation conferring drug resistance.[129] In 2012, ALK rearrangement was found in both isolated CTCs and primary tumor from 5 ALK-positive NSCLC patients, offering a potential screening tool for crizotinib treatment.[130]

In summary, CTCs offer the potential to be used in clinical settings, especially for determining or predicting prognosis or treatment outcomes. CTCs have not, however, crossed the necessary barriers to become used routinely in clinics. This is largely because of the isolation and characterization workflows used in these studies. As such, there is a need to thoroughly apply CTC assays to relevant clinical challenges and then validate these findings in larger cohorts.

1. 7 Mission statement and hypothesis

Liquid biopsies have the potential to dramatically alter the way in which we monitor cancer and inform treatment decisions. However, the adaptation of liquid biopsies routinely in the clinic is hindered by the isolation and characterization workflows for the biomarkers of

interest, along with thorough validation of clinical utility on both small and large scales. There is a clear need for the development of technologies to analyze EVs from patient plasma, along with studies to determine the clinical utility of both CTCs and EVs.

To this end, in my thesis I have developed workflows to isolate and analyze EVs, used these workflows to interrogate the clinical utility of EV cargoes in lung cancer, and investigated the clinical utility of CTCs using a microfluidic CTC isolation device in a population of lung cancer patients. These unique projects use techniques that are broadly applicable across the field of biomarkers, and the workflows developed are highly versatile and could be applied to a myriad of clinical questions in the future.

Chapter 2 Isolation and Characterization Workflows for Extracellular Vesicle (EV) Analysis

2. 1 Abstract

Extracellular vesicles (EVs), nanoscale vesicles 50-200nm in diameter, are lipid bound vesicles excreted from all cell types that are known to play important roles in the transfer of cellular information, drug resistance, and cancer metastasis. Additionally, EVs offer clinical uses including as biomarkers for cancer diagnostics or prognostics and drug delivery vehicles. While there are numerous reasons to study EVs from a biological and clinical perspective, their small size and low cargo concentrations makes them incredibly challenging to work with. As such, it is critical to develop highly sensitive isolation and characterization technologies to allow researchers and clinicians to harness the full potential of EVs for cancer diagnostics, prognostics, and therapeutics.

Microfluidics offer the potential to isolate EVs with high purity, using smaller sample volumes than conventional methods, while still allowing for a wide array of downstream applications. Here, several microfluidic technologies are presented that isolate EVs using (1) phosphatidyl serine – annexin V binding, the ^{new}ExoChip (2) On chip NK-EV biogenesis after NK cell capture and (3) direct EV biotinylation, DICE device. These methods are then validated using the necessary, and critical, characterization workflows, with an emphasis on protein characterization. These isolation technologies paired with sensitive characterization workflows are then applied to clinical cohorts.

2. 2 Resulting Publication Information

The work within this chapter contains excerpts from the following publications and manuscripts as noted:

1. Y.T. Kang, **E. Purcell,** C. Palacios-Rolston, T. Lo, N. Ramnath, S. Jolly, and S. Nagrath. "Isolation and Profiling of Circulating Tumor-Associated Exosomes Using Extracellular Vesicular Lipid–Protein Binding Affinity Based Microfluidic Device." *Small,* 2019. https://doi.org/10.1002/smll.201903600
2. Y.T. Kang*, Z. Niu*, T. Hadlock, **E. Purcell**, T. Lo, M. Zeinali, S. Owen, V. Keshamouni, R. Reddy, N. Ramnath, S. Nagrath. "On-Chip biogenesis of circulating NK cell-derived exosomes in non-small cell lung cancer exhibit anti-tumoral activity." *Advanced Science, 2020*
3. Y.T. Kang*; **E. Purcell***, T, Hadlock, T. Lo, A. Mutukuri, S. Jolly, and S. Nagrath. "Multiplex isolation and profiling of extracellular vesicles using a microfluidic DICE device." *Analyst,* 2019. https://doi.org/10.1039/C9AN01235D

Additional publications that have been generated because of the workflows developed in this section include:

1. Y.T. Kang, T. Hadlock, T. Lo, **E. Purcell**, A. Mutukuri, S. Fouladdel, M. De Silva, H. Fairbairn, V. Murlidhar, S.A. Mclean, and S. Nagrath, "Dual-isolation and profiling of circulating tumor cells and cancer exosomes from blood samples with melanoma using immunoaffinity-based microfluidic interfaces." *Advanced Science*, 2020 https://doi.org/10.1002/advs.202001581

2. T. Lo, Z. Zhu, **E. Purcell**, D. Watza, J. Wang, Y.T. Kang, S. Jolly, D. Nagrath, and S. Nagrath. "Microfluidic device for high-throughput affinity-based isolation of extracellular vesicles." *Lab on a Chip,* 2020 https://doi.org/10.1039/C9LC01190K
3. X. Tan, K. Day, X. Li, L. Broses, W. Xue, W. Wu, W. Wang, T.W. Lo, **E. Purcell**, S. Wang, Y.L. Sun, M. Oo, B. Baker, S. Nagrath, M. Day "Quantification and Immunoprofiling of Bladder Cancer Cell-Derived Extracellular Vesicles with Microfluidic Chemiluminescent ELISA." *In review*
4. Y.T. Kang, Y. J. Kim, B. Rupp, **E. Purcell,** T. Hadlock, N. Ramnath, S. Nagrath "Isolation of circulating markers for liquid biopsy using immunoaffinity-based stimuli-responsive hybrid hydrogel beads." *In submission*

2. 3 Introduction

Although EV biology is a growing field due to their potential as cancer biomarkers, current EV isolation methods inhibit our ability to further characterize their diagnostic potential. The main challenge is the quantity of exosomes found in the blood. EVs are extremely dilute compared to blood cells, making it necessary to concentrate them before performing any downstream assays. Similarly, many applications of EVs rely on isolating specific subpopulations of EV, such as tumour cell or immune cell derived EVs. There is a need for technologies that isolate specific subpopulations of EVs with high purity, allowing for the determination of the potential clinical applications of EVs.

Commercial exosome isolation kits are available and use a variety of techniques ranging from spin columns to immunoaffinity assays; however, their selectivity is poor, and these kits require many spinning and rinsing steps before running assays.[131] Examples of commercial products for exosome isolation include ExoQuick (Systems Biosciences) and Total Exosome

Isolation Reagent (Thermo). These kits, however, have low purity compared to the gold standard method: ultracentrifugation (UC).[131]

Ultracentrifugation is the most common EV isolation method; EVs are pelleted using a series of sequentially faster centrifugation steps. UC is very reliable and is compatible with a range of applications; it is, however, a long process, requires expensive equipment, and can damage EV membranes in the process. Despite these shortcomings, ultracentrifugation is considered the gold standard for exosome isolation and provides a consistent density-based isolation technique that is highly reproducible.[132] Although largely effective at separating exosomes from other sample components, ultra-centrifugation requires many steps, is time intensive, and is not feasible for clinical applications.

Microfluidics technologies offer many advantages and may become the optimal method for exosome isolation in the future. Owing to recent advances, numerous microfluidic devices for exosome isolation have been developed with better recovery and shorter processing times compared to UC.[60,133,134] Among them, immunoaffinity-based microfluidic isolation using antibodies against exosomal surface proteins is advantageous as it allows for high specificity exosome isolation from heterogeneous samples, such as plasma, serum, or urine. Although very selective, antibody binding is strong, making it challenging to remove captured exosomes without damaging their membranes. Maintaining membrane integrity is of interest for many downstream applications including studying cell-interaction mechanisms.

Microfluidics allow for on-chip profiling at significantly lower sample volumes than traditional assays while achieving higher sensitivity for applications including immunofluorescent staining, surface plasmon resonance (SPR), and surface enhanced Raman scattering (SERS).[135–137] For example, Im et al. used 150 μL pre-processed exosomal samples to

evaluate ovarian exosome's surface expression. While these on-chip profiling technologies are one potential path to clinical applicability of EVs, these methods largely require advanced knowledge of the target EVs to functionalize a device to capture the specific EVs within the sample.

As an example, antibodies against the tetraspanin CD63 have been widely applied to exosome isolation from the plasma of patients with ovarian cancer, breast cancer, and glioblastoma.[64,138–142] However, anti-CD63 is not a specific biomarker for any one cancer, and its expression is known to vary depending on the type of cancer.[143] Recent studies using clinical samples showed that only 69.56% of lung cancer patients have CD63 positive exosomes with comparably low absolute expression level compared to other exosomal markers.[94,144] To date, a few cancer specific exosomal proteins such as epidermal growth factor receptor (EGFR), prostate-specific antigen (PSA), and epidermal growth factor receptor 2 (HER2) have been incorporated into microfluidics for cancer-associated exosome isolation for lung, prostate, and breast cancers, respectively.[145–147] However, none of these methods isolate purely tumour derived EVs (TDEs), and even fewer technologies isolate immune cell derived EVs or exosomes.

Following the development of an isolation technology, it is critical to ensure that the isolated vesicles are pure and the vesicles of interest. Nomenclature and definitions around the types of EVs are currently being developed among researchers. A body of researchers, the International Society of Extracellular Vesicles, has set out a series of guidelines defining the characteristics and assays needed to definitely call a researcher's isolated samples extracellular vesicles or exosomes.[19] These include size (50-200nm), morphology, and the most challenging characteristic, protein expression. Proteins found in EVs differ based on the cell type of origin,

therefore protein assays need to be optimized and validated for each cell type and technology, and protein characterization technologies are in high demand.

In summary, there is a need for microfluidic technologies that isolate specific EV populations using immunoaffinity-based chemistries. However, it is also beneficial to be able to release the EVs or use viable EVs after isolation. As such, the chemistries need to allow for a release mechanism that does not use highly basic solutions or high temperatures. Following isolation, it is critical to have accurate workflows for EV characterization to ensure that the samples are isolated with high purity and sensitivity. Finally, there is a need to develop technologies that couple isolation and characterization to decrease the amount of precious sample used.

2. 4 Methods

2.4.1 Ultracentrifugation

Plasma or cell culture media was centrifuged at 12,000xg for 20 minutes to remove cellular debris. The supernatant was then ultracentrifuged at 100,000xg for 90 min to pellet the EVs using 36 mL Polyethylene terephthalate (PET) tubes (Thermo Fisher). Excess tube volume was filled with sterile PBS pH 7.4 (Gibco). The extracellular vesicle-pellet was washed with PBS and centrifuged at 100,000 x g for 90 min. Extracellular vesicles were suspended in 100 µL PBS pH 7.4 or RIPA with protease inhibitor cocktail (Fisher Scientific) and frozen at -20°C. EVs stored in PBS were then used for nanoparticle tracking analysis along with RNA extraction and characterization, while EVs in RIPA were used for western blot analysis.

2.4.2 Nanoparticle tracking analysis (NTA)

Nanoparticle tracking analysis (NTA) was performed using Malvern's Nanosight equipment. Two operation procedures were used depending on the volume of the sample. For larger volumes, quantification was performed using five 30-second runs at a flow rate of 20 using the brightness setting of 15. The camera detection was set to a level of 4 for all runs. Runs were then averaged with the average and standard deviation between the runs being reported. For smaller volumes, 30 µL of the prepared solution was applied to the jig of the system. The particle movement was monitored through a video sequence for 20 s in triplicate in stagnant mode. For either sample type, all data acquisition and processing were performed using NanoSight NS300 control software, and concentration of particles in exosome size range was used for calculating capture and release efficiencies of the present platform.

2.4.3 Protein extraction and Western Blot

EVs were isolated from ultracentrifugation into 150 µL RIPA buffer (Thermo Scientific, cat #89900), protein concentration was measured by microBCA™ Protein Assay Kit (Thermo Scientific cat #23235). Western blot loading was normalized by using 5mL blood volume for extracellular vesicle isolation, loading the maximum protein (37.5 µL) in each lane, and using Bio-Rad's Stain Free gels to allow normalization. Briefly, the protein was separated at 250V for 30 minutes. Semi-dry transfer was then performed using Trans-Blot Turbo Transfer System (Bio-Rad) to a high fluorescence PVFD membrane (Bio-Rad, cat #1620261). The membrane was imaged using Bio-Rad's ChemiDoc to quantify total protein per lane. The membrane was blocked and incubated overnight with primary antibody in 5mL of 5% bovine serum albumin (Sigma-Alrich) in Tris Buffered Saline (TBS) (Bio-Rad). with 1% Tween 20 (Sigma-Aldrich) (TBST). The membrane was then washed thoroughly before incubating with HRP-secondary

antibody in 3% nonfat milk in TBST for 90 minutes followed again by additional washes. Measurement was performed using SuperSignal™ West Pico PLUS Chemiluminescent Substrate (Bio-Rad, Cat#34579) and SuperSignal West Femto (Thermo, cat #34096) and imaged on the ChemiDoc.

2.4.4 Wes Protein Processing

The Wes system from Protein Simple was used according to manufacturer's protocol. EV samples were isolated into RIPA buffer, same as for western blots. 3µL of protein lysate was used per sample, per lane. All antibodies used were from a rabbit host, and so the anti-rabbit detection kit was used (Protein Simple). The CD9 antibody (CellSignaling) was used at 1:50 dilution, and the EGF Receptor antibody (CellSignaling) was used at 1:10 dilution.

2.4.5 newExoChip fabrication and processing

2.4.4.1 Device design and fabrication

The ^{new}ExoChip device has 30 ripple-shaped channels, and each channel is composed of 60 circular channels in a row. Each circle has a diameter of 500 µm and the distance between each circle is 900 µm. The ^{new}ExoChip is fabricated by standard soft lithography including mold fabrication and PDMS molding. For the surface modification on the device, standard avidin–biotin chemistry was used with optimization. In the final step, the devices were injected with Avidin (1 mL of filtered PBS + 100 µL of NeutrAvidin), placed in a Petri dish sealed with parafilm along with wet paper napkins, and incubated overnight in a standard refrigerator. After 1–10 days, the devices were defrosted and washed out with filtered PBS. Before the biotinylated annexin V conjugation, the coverage of avidin in our device was checked and confirmed using biotinylated staining dye (Supporting Information S3). The devices were then injected with 110

μL of the biotinylated annexin V (10 μL annexin V + 100 μL of 1× binding buffer): 55 μL into the inlet, a 30-min incubation period, 55 μL into the outlet, and another 30-min incubation period before use.

2.4.4.2 Sample Processing—Exosome Capture and Release

The prepared model samples or patient plasma samples were processed using a Harvard syringe pump at the flow rate of 0.3–1.2 mL h^{-1}. All samples were prepared in the 1× of binding buffer containing 2.5 mm of $CaCl_2$ to be actively conjugated with annexin V. 300 μL of sample was withdrawn into a 1 mL syringe and connected to the device. After exosome capture, 200 μL of 1× binding buffer was processed at the flow rate of 1 mL h^{-1} to remove the excess unbound vesicles/proteins. For the release of the captured exosomes, 300 μL of 20 mm EDTA solution was flowed at the flow rate of 1 mL h^{-1} in two steps: the 1st 150 μL injection and 30 min incubation without flow. Another 150 μL was flowed and 200 μL of PBS buffer injection was followed at the flow rate of 1 mL h^{-1} to make sample 500 μL in total.

2.4.4.3 On-chip Protein Extraction and Western Blot Analysis

Exosome lysis was performed using RIPA buffer with 1% protease inhibitor. The prepared buffer solution was flowed through the device at the flow rate of 50 μL min^{-1} right after exosome isolation. Initially, 40 μL of sample was injected to remove residual solution in the device and sample collection was started after 40 μL. This was immediately followed by an injection of 50 μL per device at the same rate. Devices were incubated for 5 min, and then injected with another 50 μL at 50 μL min^{-1}. Finally, devices were manually injected with air to push out as much sample as possible from each device. The collected samples were then gently dispersed by vortex mixer and kept at −20 °C. Western blot analysis was performed as previously described (**Chapter 2 Methods 2.4.3**). Specifically, primary antibodies were

incubated overnight on a rocker at 4 °C at a concentration of 1:500 (Flotillin-1, Santa Cruz), 1:1000 (CD9, Cell Signaling; Calnexin, Cell Signaling), or 1:1500 (Beta-Actin, Cell Signaling) in 3% non-fat milk in TBST. Thorough rinsing was performed, and then secondary antibody was incubated for 2 h at room temperature (anti-Mouse, Santa Cruz; anti-Rabbit HRP, Cell Signaling) at 1:1500 in 3% non-fat milk in TBST.

2.4.6 NK-cell derived EV workflow to protein extraction

2.4.5.1 Exosome biogenesis on graphene oxide (GO) chip

NK cell capture was performed by flowing the sample containing NK cells through the prepared GO chip devices using a syringe pump at a flow rate of 1 mL h^{-1}. PBS buffer was then applied to wash away nonbonded cells. 300 µL of MEM-alpha serum-free media with 20% exosome-depleted fetal bovine serum (FBS) (Gibco, USA) and 200U/ml recombinant human interleukin 2 (rhIL-2) (PeproTech, USA) was then pumped into the device with low flow rate (1 mL h−1). Incubation for 12 h with the whole device was then performed at 37 °C, 5% CO2 incubator Galaxy 14S (Brunswick, USA) to generate the EV-rich supernatant.

2.4.5.2 NK Cell-Derived Exosomes Isolation/Release Using Magnetic Beads for Protein Extraction

200 µL of supernatant from the device was directly applied to the prepared magnetic beads (ExoBead) conjugated with anti-CD63 for exosome capture. This mixture was incubated on a rotator for an hour, and magnetic beads were separated using a magnet, followed by PBS washing three times. The beads right after this step underwent SEM or western blot analysis. For the release of the captured exosomes on the beads, 1 mL of 0.5×10^{-3} M biotin solutions was added to the separated beads, consisting of 1 mL of filtered water and 10 µL of biotin solution

and incubated for 0.5–2 h. RIPA buffer with 1% protease inhibitor was prepared for lysis of captured exosomes. 30 μL of the prepared buffer solution was injected to postcapture ExoBeads and incubated for 20 min. After incubation, the protein lysate was aspirated and stored separately. Western blots were performed based on the protocols described above. Primary antibodies for this project were: Flotillin 1 (1:1000 dilution), HLA-C (1:2000 dilution), and CD56 (1:1000 dilution). Secondaries were anti-mouse HRP (1:1500 dilution, SantaCruz) and anti-rabbit HRP (1:1500 dilution, Cell Signaling).

2.4.7 DICE Device fabrication and processing

2.4.6.1 DICE Fabrication

The DICE device has four quadrants, with each quadrant having 13 × 13 circular chambers connected by junction channels. Each circular chamber has a diameter of 100 μm and the pitch is 500 μm. The circular chamber design facilitates efficient EV isolation and easy analysis based on our previous simulation and experimental results.[14] The height of the device is 50 μm and to achieve this high-aspect ratio design, we fabricate the mold using deep reactive-ion etching (DRIE). Briefly, SPR220 was spin coated onto a four-inch silicon wafer at a thickness of 3 μm before exposure and post-baking. DRIE was then performed to achieve a height of 56.1 ± 0.79 μm. After mold fabrication, the DICE device was fabricated by combining PDMS and PDMS curing agent mix (1:10) before baking overnight at 70 °C. The prepared PDMS layer was bonded to an untreated glass slide by O2 plasma treatment.

2.4.6.2 Device Functionalization

For the surface modification of the device, we used standard avidin–biotin chemistry with optimization. Following initial device fabrication, ethanol with silane solution was injected into

each device and incubated for an hour. Each device was then injected with GMBS solution (5 mL ethanol + 14 μL GMBS) and incubated for 30 minutes. Each device was once again washed out with ethanol before injection with a NeutrAvidin solution (1 mL filtered PBS + 100 μL NeutrAvidin). Each device was then stored in a parafilm sealed Petri dish containing wet paper and stored at 4 °C for future use. Devices used as no surface modification controls were not treated by the modification procedure. Control devices were injected with 3% BSA solution (0.03 g per 1 mL filtered PBS) to prevent nonspecific binding and incubated for at least 30 minutes. This 3% BSA solution was washed out with PBS buffer before storage and use.

2.4.6.3 Extracellular vesicle purification and sample preparation

The sample collection and experiments were approved by University of Michigan Institutional Review Board (IRB). Informed consents were obtained from all participants of this clinical study and blood samples were obtained after approval of the institutional review board at the University of Michigan. All experiments were performed in accordance with the approved guidelines and regulations by the ethics committee at the University of Michigan. EV purification from the blood sample was followed by recent consents for general EV research. Whole blood samples were collected in EDTA tubes and were subsequently centrifuged at 2000g for 15 minutes to isolate plasma. The isolated plasma samples from cancer and healthy donors were kept at −80 °C before use and used within 6 months. From the separated plasma layer, 100 μL aliquots were placed into ultracentrifugation tubes (Beckman Coulter, United State) along with 100 μL of 0.2 μm filtered PBS. The tubed samples then underwent Airfuge ultracentrifugation (Beckman Coulter, United States) using an A-100/30 angle rotor for 40 minutes at 100 000g. After the 1st ultracentrifugation, 150 μL of supernatant was removed from each tube and replaced with 150 μL of filtered PBS, followed by an additional round of

ultracentrifugation at 100 000g for 40 minutes. Following ultracentrifugation, 150 μL of supernatant from each tube was discarded and the remaining contents containing the purified EV pellet were ready for biotinylation. For the performance verification of the DICE device, purified EVs from A549 lung adenocarcinoma were purchased and used as a model sample. This EV sample was directly biotinylated without any purification steps.

2.4.6.4 Biotinylation of extracellular vesicles

Purified EVs were biotinylated for non-biased immobilization following the EZ-Link protocol with optimization. EZ link biotin powder, EZ-Link Sulfo-NHS-LC-Biotin (ThermoScientific, United States) was utilized for EV biotinylation during these experiments. A 10× concentration of 300 μM biotin solution was prepared by dissolving 1.6 mg of E–Z link biotin in 10 mL of filtered PBS. This 10× solution was then diluted to 1× by incorporating 100 μL of the 10× solution with an additional 900 μL of filtered PBS. 100 μL of 1× 300 μM biotin solution was then added to 50 μL of purified EVs, followed by a 1-hour incubation. Refrigerated desalt spin columns were prepared using repeated PBS washing and centrifugation steps following the manufacturer stated procedure. After the hour-long EV incubation, 150 μL of the biotinylated EV sample was injected into the desalt spin column and centrifuged at 1500g for 2 minutes. The sample was then passed through a 0.2 μm filter and stored in vials at −80 °C for future use. Biotinylation of purified A549 cell derived EVs for the EV immobilization on chip experiment followed the same procedure as that of clinical samples. To evaluate the effect of biotinylation on EV's surface marker binding sites, we prepared two different EV samples using a plasma sample from a healthy control: one before and one after biotinylation. EVs were isolated using an Airfuge ultracentrifugation using the previously described procedures. One 150 μL sample was then biotinylated using the previously outline biotinylation procedure, while

another 150 µL sample did not undergo biotinylation. Both biotinylated and non-biotinylated samples were injected with 5 µL of CD9 anti-rabbit antibody in ultracentrifugation tubes and allowed to incubate for 1 hour. Each sample underwent a second Airfuge ultracentrifugation for 20 minutes at 100 000g, followed by extraction of 100 µL of supernatant to remove excess antibody. 50 µL of filtered PBS was then added to the remaining sample in each UC tube, along with 3 µL of AlexaFluor 647 goat anti-rabbit (ThermoScientific, United States). This secondary antibody was incubated for 1 hour followed by 20-minute ultracentrifugation at 100 000g. After ultracentrifugation, 50 µl of sample was extracted from each UC vial and the pellet was discarded. The fluorescence intensities from these samples were compared by using a fluorescence microscope.

2.4.6.5 Device operation and performance verification

The prepared model samples or patient biotinylated EV samples were processed using a Harvard syringe pump. Filtered PBS was first injected through the inlet of each device to remove leftover NeutrAvidin. A total of 100 µL of pre-enriched EV sample was then pumped through the inlet of each device, followed by another PBS wash step to clear any non-bonded sample from the PDMS chamber. Multiplexed immunofluorescence staining was performed by using each of four different outlets to inject either specific antibodies or lipophilic dyes.

2.4.6.4 Field emission scanning electron microscopy (FE-SEM) analysis

EVs captured within the device were fixed in 2.5% glutaraldehyde for one hour to retain their morphology. After rinsing with PBS, the samples were dehydrated in a graded concentration of ethanol (50%, 70%, 90%, 95%, and 100%) for 10 min at each step (two times for 100%). The samples were dried using hexamethyldisilane, followed by overnight air drying in the hood. The dehydrated samples were then mounted on aluminum stubs and sputter coated

with gold to create a conductive layer. The samples were observed by FEI Nova 200 Nanolab Dualbeam FIB scanning electron microscope at The Michigan Center for Materials Characterization (MC2) at University of Michigan.

2.4.6.5 On-chip immunostaining analysis

For immunofluorescence staining, each device was first blocked with 5% BSA solution. Next, inlet tubing was removed from each device and 3″ tubing was attached to each of the four outlets. Through each of these outlets, 50 μL of either PD-L1, Vimentin, CD9, or EGFR (1 : 20 dilution in 1% BSA solution) were applied and incubated overnight at 4 °C. After overnight incubation, a PBS wash was run through each outlet to remove excess primaries. The outlet tubing was then removed, and a single tube was attached to the inlet. A secondary solution of 2.5 μL anti-mouse IgG2b 488 and 2.5 μL anti-rabbit IgG 647 in 100 μL of 1%BSA was pumped through the device inlet and incubated for 35 minutes. A final PBS wash was applied through the inlet to clear unbound secondaries. Each device was then imaged at 4×, 10×, 20×, and 40× magnification (Eclipse TI2, Nikon, Japan.) Devices were scanned in FITC for PD-L1 confirmation and CY5 for confirmation of Vimentin, CD9, and EGFR. Analysis was performed by measuring the fluorescent intensity of each circular chamber in each quadrant. The average intensity across all chambers per quadrant was taken by dividing total intensity by the area of the chambers summed. The standard deviation is then representative of the variations in fluorescence intensity across all the chambers in one quadrant.

2. 5 Results

2.5.1 Optimized workflows for EV quantification and characterization

The backbone for EV research is the isolation and validation workflows that come before the downstream clinical or biological application. First, several isolation methods are available, ultracentrifugation[131,148], commercial kits (commonly polymer precipitation) [47,51,52], and immunoaffinity (commonly microfluidics)[63,141,149–152], **Figure 2-1.** Following isolation, the International Society for Extracellular Vesicles has created a checklist for the necessary workflows to validate pure EV isolation.[19] The backbone for these workflows is shown in **Figure 2-1**. These guidelines require protein expression[69], size and concentration measurement[69], and then morphology validation using electron microscopy[67,68]. From there, the EVs can be used for clinical applications such as RNA profiling[40,65,68,92,153,154], protein expression[78–80], functional analysis[155–157], or drug delivery[26,29,30,33,34]. To perform NTA, electron microscopy, or applications

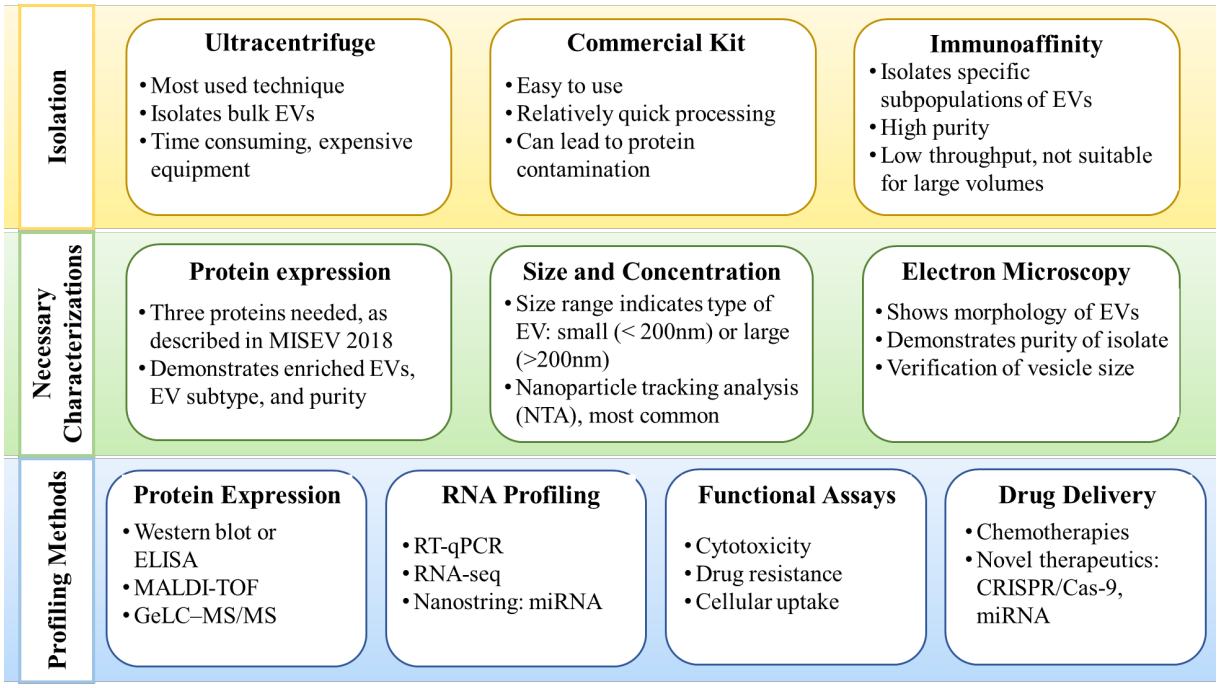

Figure 2-1 Outline of EV isolation, characterization, and profiling methods.

where intact EVs are needed, the EVs are isolated straight into PBS. If protein characterization is the goal, then the EVs are isolated into RIPA with PIC.

Each study involving EVs must go through the required assays as shown in "Necessary Characterizations" in **Figure 2-1.** before researchers can proceed with their application (i.e. biomarker, drug delivery, etc). An example of the data collected from these workflows are shown in **Figure 2-2**. For these experiments, EVs were isolated from either cell culture media or plasma using ultracentrifugation and isolated into two buffers, the first into PBS and the second into RIPA buffer. From the PBS samples, NTA and transmission electron microscope were performed to validate the size and shape of the EVs, along with quantifying the concentration of the EVs, **Figure 2-2A**. The NTA results indicate a clean sample with most vesicles within the expected size range, 50-200nm, **Figure 2-2A**. The TEM image indicates a nice round, spherical morphology, demonstrating an intact EV at the correct size, 85nm, **Figure 2-2B**. From the RIPA sample, western blots were performed to show the presence of the EV-specific proteins CD9 and CD81, **Figure 2-2C**.

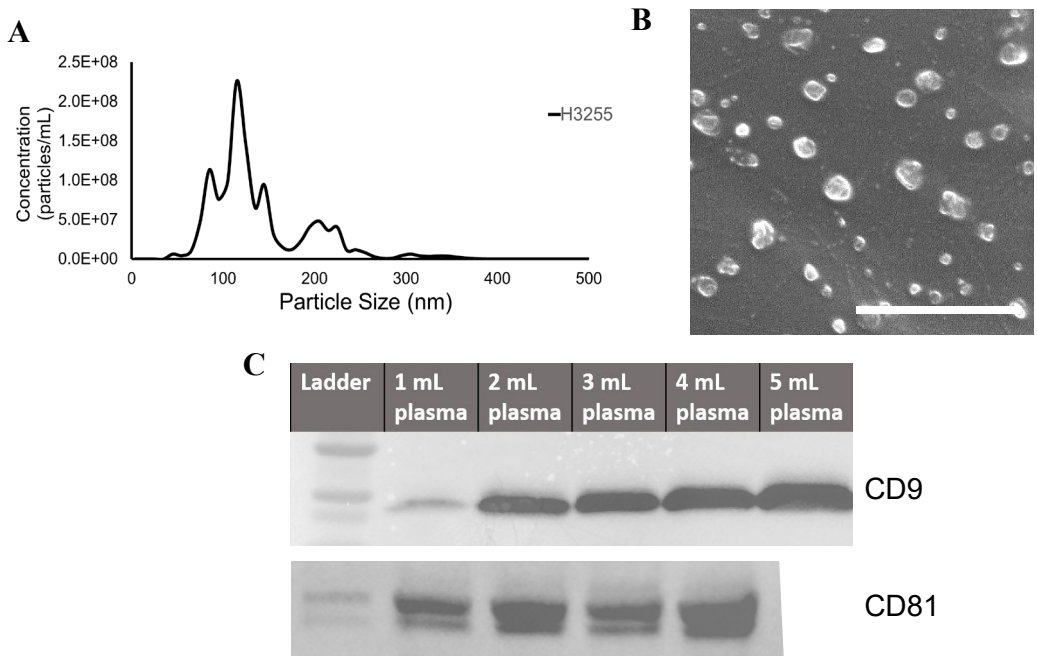

Figure 2-2 Examples of EV characterization assays

A. Nanoparticle tracking analysis (NTA) of a cell-line derived EV sample indicates the concentration and size of isolated EVs. **B.** Transmission electron microscopy (TEM) of a single EV isolated from a plasma sample. Scale bar is 1μm. **C.** Western blot analysis of EVs isolation from 1-5mL of plasma using UC. The EVs were analyzed for both CD9 and CD81, common EV markers.

NTA and EM workflows remain the same for all samples, however, different EV populations will express unique EV-specific proteins. For example, it is known that EVs from lung cancer plasma have elevated CD9 and CD81, but low CD63, while EVs from NK cells do not express CD9 or the other tetraspanins.[19,94] These restrictions mean that optimization needs to be performed for every unique EV application. In the next several sections, I describe unique EV isolation and characterization technologies along with the protein characterization that verified those workflows.

2.5.2 [new]ExoChip isolation technology using PS-Annexin V binding chemistry to isolate tumor-specific exosomes

As discussed above, the first step in the EV or exosome workflow is reliable isolation. However, one of the main challenges of using EVs for clinical and biological applications in cancer is isolating purely tumor derived EVs. Immunoaffinity-based microfluidic EV isolation using anti-CD63 is widely used; however, anti-CD63 is not specific to cancer-EVs, and some cancers secrete EVs with low expression of CD63.[143] For example, recent studies using clinical samples showed that only 69.56% of lung cancer patients have CD63 positive exosomes with comparably low absolute expression level compared to other exosomal markers.[144] To date, a few cancer specific exosomal proteins such as epidermal growth factor receptor (EGFR), prostate-specific antigen (PSA), and epidermal growth factor receptor 2 (HER2) have been

incorporated into microfluidics for cancer-associated exosome isolation for lung, prostate, and breast cancers, respectively.[145,146]

Alternatively, phosphatidylserine (PS), usually expressed in the inner leaflet of the lipid bilayer of the cells, is shown to be expressed on the outer surface of cancer associated EVs. A new exosome isolation microfluidic device ([new]ExoChip), conjugated with a PS-specific protein, to isolate cancer-associated exosomes from plasma, is presented, **Figure 2-3**. Briefly, the device achieves 90% capture efficiency for cancer cell exosomes compared to 38% for healthy exosomes and isolates 35% more A549-derived exosomes than an anti-CD63-conjugated device. Immobilized exosomes are then easily released using Ca^{2+} chelation. The recovered exosomes

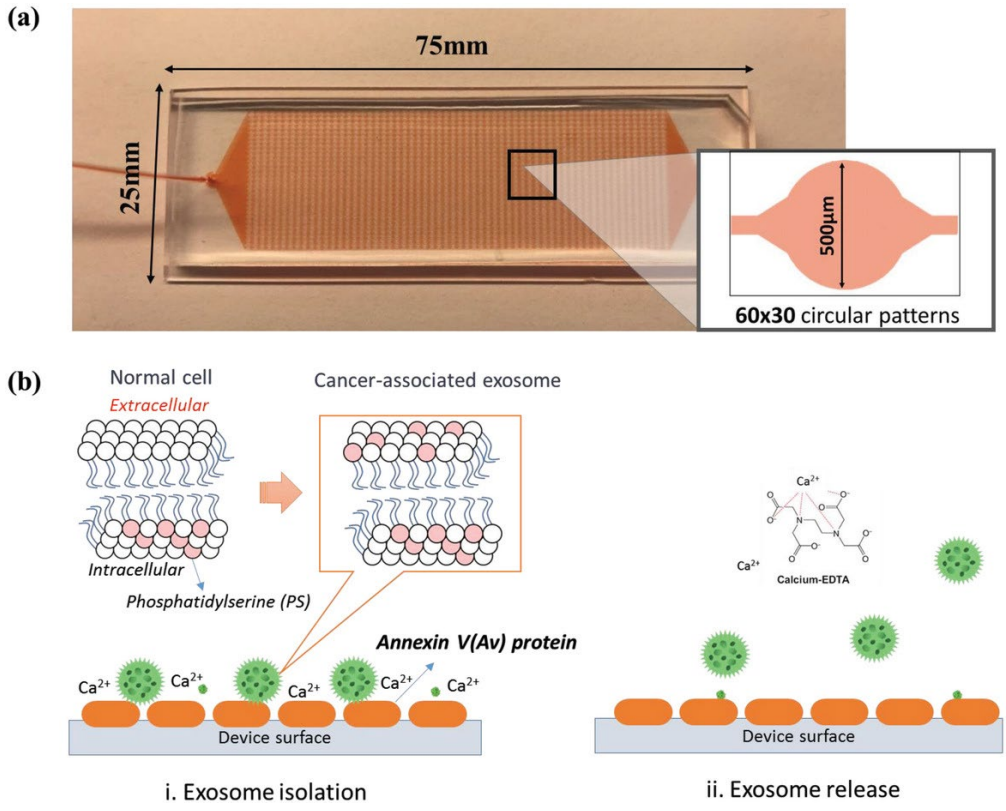

Figure 2-3 Design of the [new]ExoChip with schematic of capture mechanism.

A. Picture of the [new]ExoChip with dimensions, indicating the many chambers for exosome capture. **B.** Illustration of the capture and release schematic for the PS-Annexin V isolation and release chemistry**.**

from clinical samples are characterized by electron microscopy and western-blot analysis, revealing exosomal shapes and exosomal protein expressions. The ^{new}ExoChip facilitates the isolation of a specific subset of exosomes, allowing the exploration of the undiscovered roles of exosomes in cancer progression and metastasis.

The annexin V immobilized microfluidic device is designed with alternating narrow and wide ripple-like designs, inspired by the ExoChip, that enhances the binding interaction between specific exosomes and PS-targeting molecules, thus resulting in higher capture efficiency and purity at conditions of high flow rates (**Figure 2-3**). Compared to our previous ExoChip[60], the ^{new}ExoChip has 225 times more micro-sized circular chambers, enabling faster sample processing with higher selectivity (**Figure 2-3A**). COMSOL models indicate that there are lower velocities along the edges of the circular chambers than the rectangular chambers, **Figure 2-4**. This lower velocity allows the EVs to better bind to the device, slower velocities mean increased binding time and hence higher binding potential. This higher binding potential allows us to capture higher concentrations of EVs compared to previous device designs.

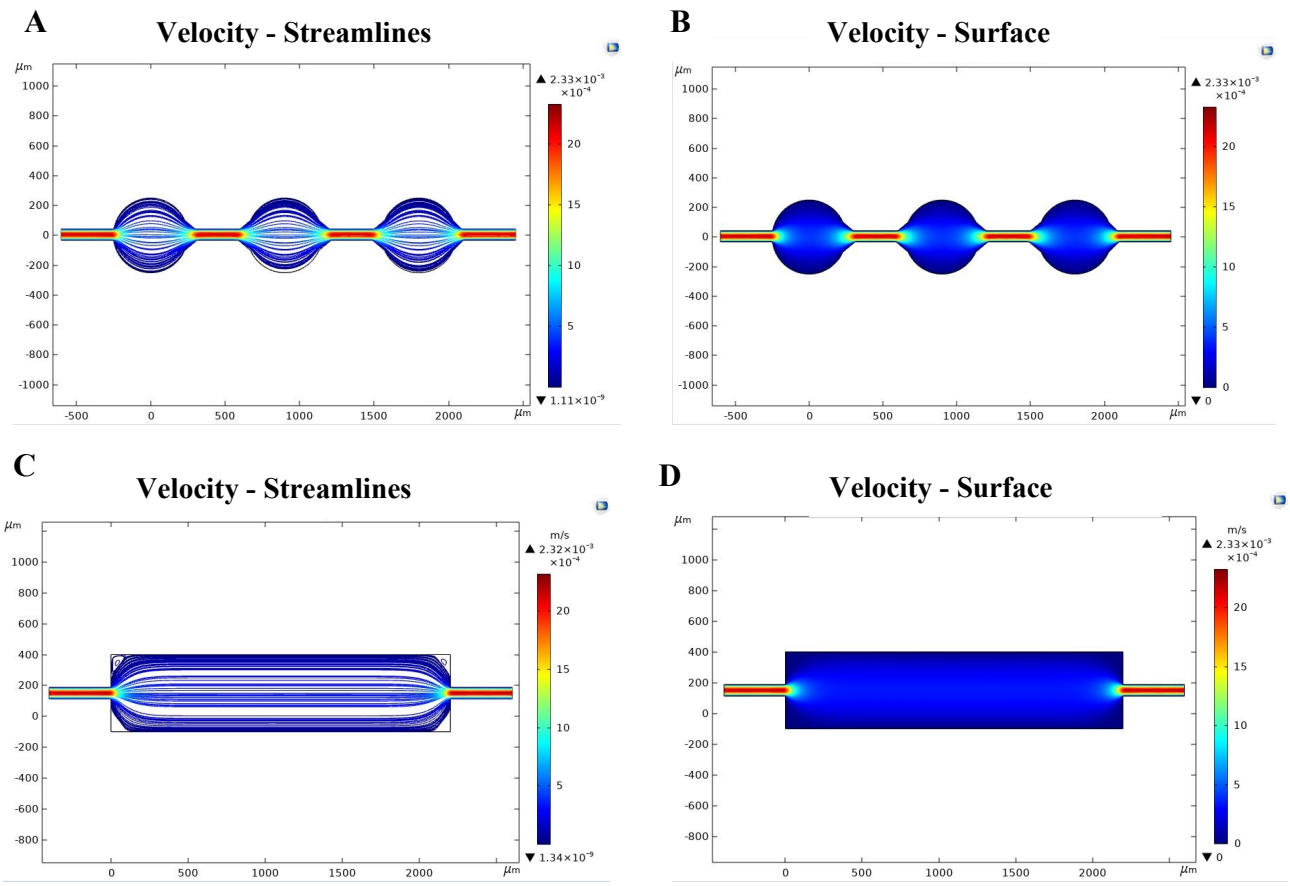

Figure 2-4. Comparative COMSOL models of the ^{new}ExoChip.

A-B. Velocity profiles for ^{new}ExoChip and **C-D.** a standard rectangular chamber demonstrates the decrease in velocity along the edge of the chambers. This decrease in velocity allows for increase binding in the ^{new}ExoChip**.**

Following validation experiments with control devices and cell line models, we then applied this technology to study clinical blood samples from patients with non-small cell lung cancer (NSCLC) and melanoma to verify the translational potential of our devices. This was the first device that we developed and there were concerns about whether the ^{new}ExoChip would isolate enough EV material to fully characterize, especially when using our protein workflows.

We extended our study to 12 clinical plasma samples from lung (n = 4), melanoma (n = 3) and healthy donors (n = 5). In all cases, we used 30–100 µL of plasma samples for exosome isolation using our ^{new}ExoChip. The concentration, size distribution, shapes, and proteins

expression levels of exosomes released from the device were evaluated using NTA, SEM, and western blot analysis. **Figure 2-5A** shows the various exosome concentrations for each patient and by cancer type. Although the five healthy donors show similar exosomal concentrations, the cancer patients showed a wide range of exosome concentrations. The *Ma* showed the highest (2.79×10^9 per mL) and *Ld* showed the lowest concentration (2.89×10^8). Statistical analysis of particle size confirmed specificity of most samples, both cancerous and healthy (**Figure 2-5B**). While there is a wide range of particulate sizes captured, the mean size of every sample falls below 150 nm in diameter, and the mode of each sample (excluding *Ld*) falls lower than the corresponding mean. Interestingly, the average size of exosomes from lung cancer was bigger than those of melanoma and healthy control. Similar size differences were shown in our cell line experiments. This could imply that lung cancer exosomes isolated by PS-annexin V affinity might be larger than usual or that another majority of extracellular vesicles in lung cancer might affect this size distribution. However, this information, along with the median values, showed that a considerable portion of samples collected from all sample types fall within the exosomal size range. The varying sizes of captured exosomes were also verified by SEM analysis (**Figure 2-5C**).

To confirm that the captured vesicles from our device are exosomes, we used western blot analysis to verify the expression of exosomal markers. Instead of using CD63, which is known to have lower expression on lung cancer exosomes, we used CD9 and Flotillin-1 as exosomal markers. From the western blot analysis using three lung plasma samples and two melanoma samples, we see positive bands for both exosomal markers (**Figure 2-5D**). Additionally, the samples were probed for Beta-Actin as a standard loading control and calnexin to verify that there was no cellular contamination within the samples.

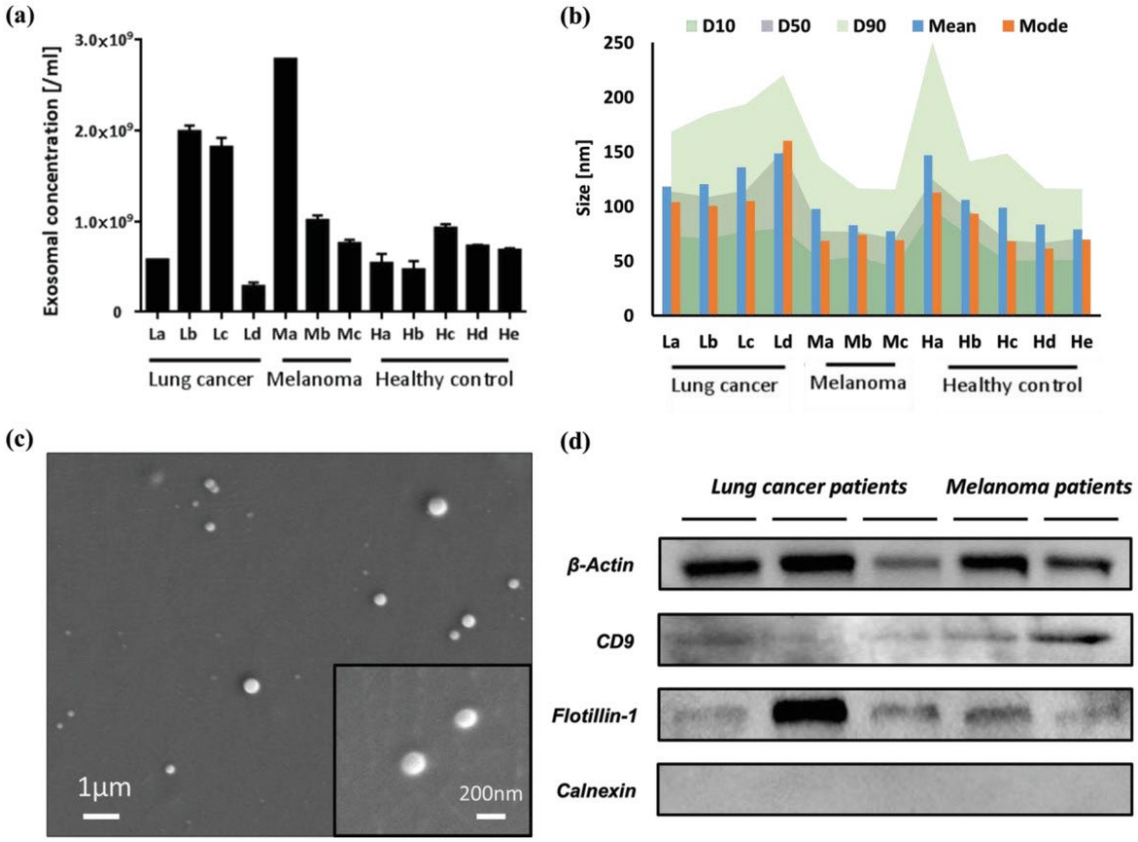

Figure 2-5. Isolation of exosomes from clinical samples from cancer patients and healthy donors.

A. Vesicle size distribution regarding mean, mode, and D-values (D10, D50, and D90) after release. **B.** Exosome concentration after newExoChip-based exosome recovery. **C.** SEM image of isolated exosome and the magnified view of the exosome from a melanoma patient. **D.** A representative western blot analysis of the protein isolated from ^{new}ExoChip and characterized for exosomal markers and intracellular protein marker in five different cancer patients' plasma samples.

In summary, the PS-Annexin V binding chemistry of the ^{new}ExoChip allows us to capture highly pure cancer-associated EVs from clinical plasma samples. This offers the potential for clinical applications of EVs for diagnostics and prognostics. However, this chemistry is only effective for tumor derived EVs. Other EVs of interest, including those from immune cells, would not be captured using this method. As such, other isolation chemistries are needed.

The results and excerpts in this section are found in the following publication:

Y.T. Kang, **E. Purcell,** C. Palacios-Rolston, T. Lo, N. Ramnath, S. Jolly, and S. Nagrath. "Isolation and Profiling of Circulating Tumor-Associated Exosomes Using Extracellular Vesicular Lipid–Protein Binding Affinity Based Microfluidic Device." *Small,* 2019. https://doi.org/10.1002/smll.201903600

2.5.3 On-Chip Biogenesis of Circulating NK Cell-Derived Exosomes in Non-Small Cell Lung Cancer Exhibits Antitumoral Activity

As the recognition between natural killer (NK) cells and cancer cells does not require antigen presentation, NK cells are being actively studied for use in adoptive cell therapies in the rapidly evolving armamentarium of cancer immunotherapy. In addition to utilizing NK cells, recent studies have shown that exosomes derived from NK cells also exhibit antitumor properties. Furthermore, these NK cell-derived exosomes exhibit higher stability, greater modification potentials and less immunogenicity compared to NK cells. Therefore, technologies that allow highly sensitive and specific isolation of NK cells and NK cell-derived exosomes can enable personalized NK-mediated cancer therapeutics in the future.

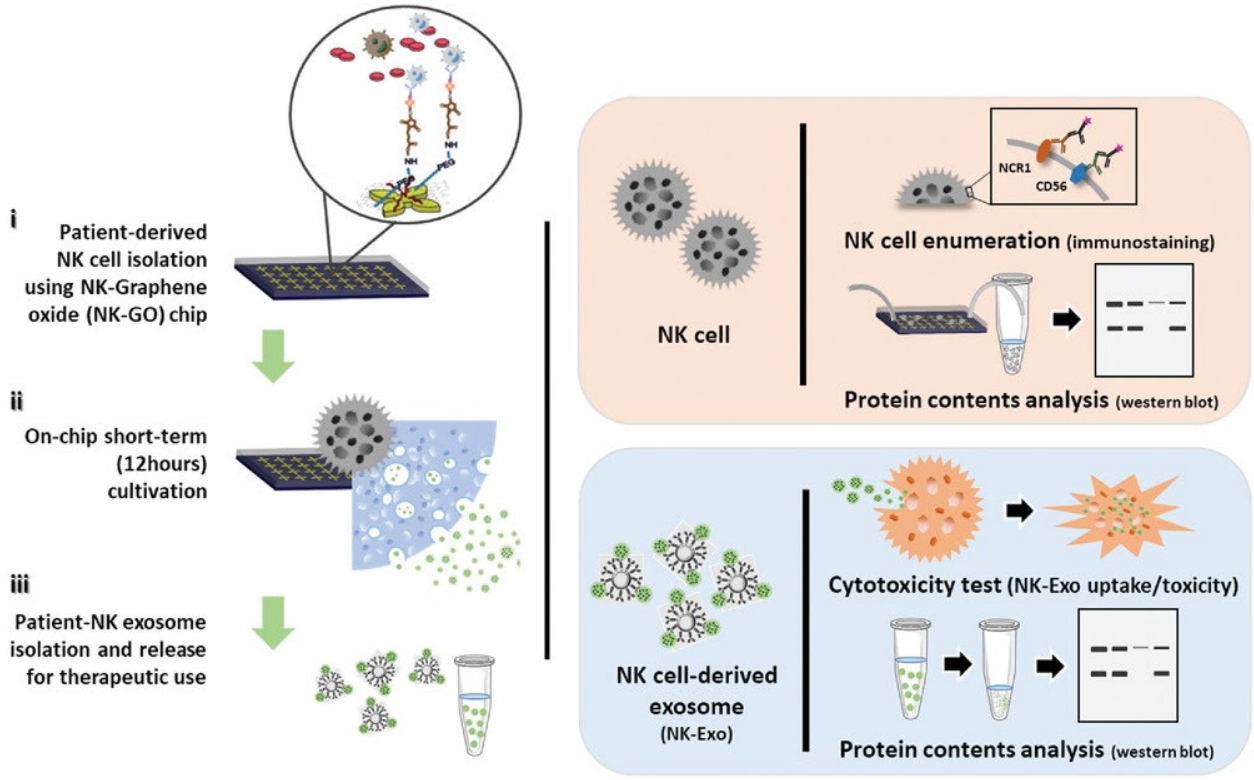

Figure 2-6. Schematic for the workflow to isolate NK-exosomes after on-chip biogenesis from captured NK cells.

Here, a novel microfluidic system to collect patient-specific NK cells and on-chip biogenesis of NK-exosomes is proposed, the schematic of the workflow is show in **Figure 2-6**. In a small cohort of non-small cell lung cancer (NSCLC) patients, both NK cells and circulating tumor cells (CTCs) were isolated, and it is found NSCLC patients have high numbers of NK and NK-exosomes compared with healthy donors, and these concentrations show a trend of positive and negative correlations with bloodborne CTC numbers, respectively. It is further demonstrated that the NK-exosomes harvested from NK-graphene oxide chip exhibit cytotoxic effect on CTCs. This versatile system is expected to be used for patient-specific NK-based immunotherapies along with CTCs for potential prognostic/diagnostic applications.

However, for this application to become clinical feasible, thorough characterization of the isolated exosomes is critical. The isolation of exosomes after isolation of the parent cells on the GO chip is a novel technique, and we again needed to establish whether there would be enough product for characterization. Because the cells, and not the EVs, were captured, we needed to validate whether the quantity of EV-protein was sufficient for western blot analysis. A further challenge of this technology is that we isolated NK cell derived EVs, which are notorious for not expressing CD9, our best EV-marker.[19] As such, we tested and optimized new markers, flotillin 1 (FLOT1) and HLA-C, both of which fall within MISEV's guidelines for EV purity.

In our clinical cohort of 5 lung cancer patients and 2 healthy controls, we first demonstrated the isolation of NK cells on the NK-GO chip **Figure 2-7A.** The highly pure NK cell isolation allows us to ensure that the collected EVs are definitively NK-EVs. The purity of those EVs was qualified using FLOT-1 and HLA-C, **Figure 2-7B**. Although both healthy donors

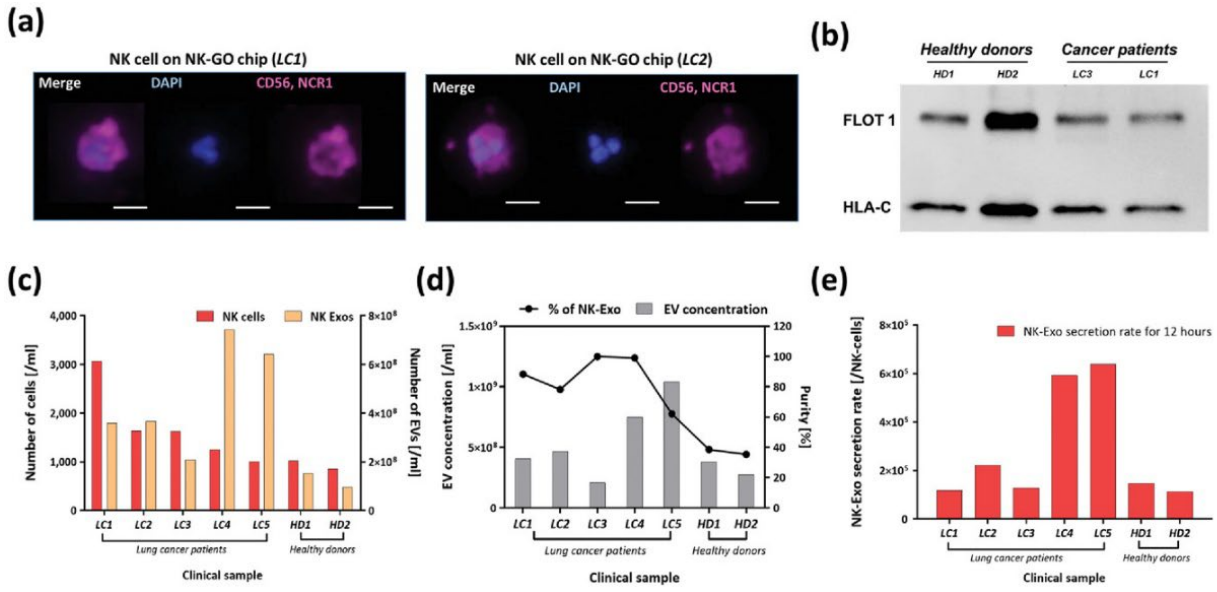

Figure 2-7 Analysis of clinical samples from NSCLC patients using NK-GO microfluidic platform.

A. Immunofluorescence image examples of CD56/NCR1 + NK cells captured on NK-GO chip (Scale bar = 20 μm); **B.** western blot analysis for showing the positive expression of FLOT1 and HLA-C in exosomes from clinical samples; **C.** profiling in quantity of NK cells and NK cell-derived exosomes among different patients and healthy individuals observed after 12 h on-chip incubation; **D.** total extracellular vesicle concentration and percentage of exosomes among patient samples and healthy control samples; **E.** biogenesis of exosomes quantified as secretion rate of exosomes per captured NK cells for 12 h.

and lung cancer patients had varying levels of both, the strong presence of both markers indicates the definite isolation of EVs. This result also demonstrates that despite only using a very low number of EVs, we were able to get reliable western blot results. This is emphasized by the finding that patients' samples from which we captured only 1,000 NK cells excreted only $2x10^8$ EVs, which is notably lower than other devices we have developed, **Figure 2-7C**. The western blot purity finding is further complemented by the finding that our EV isolation from NK-cells on GO chip led to EV purities that were above 60% by size, and above 80% for 4 out of 5 lung cancer patients. Finally, we were able to calculate the excretion rate of NK cell-derived EVs on chip per NK-cell, which has been rarely studied, **Figure 2-7D**. The excretion rate finding is the driving force for the final chapter of this thesis, **Chapter 5**.

The results and excerpts in this section are found in the following publication:

Y.T. Kang*, Z. Niu*, T. Hadlock, **E. Purcell**, T. Lo, M. Zeinali, S. Owen, V. Keshamouni, R. Reddy, N. Ramnath, S. Nagrath. "On-Chip biogenesis of circulating NK cell-derived exosomes in non-small cell lung cancer exhibit anti-tumoral activity." *Advanced Science, 2020*

2.5.4 Multiplex isolation and profiling of extracellular vesicles using a microfluidic DICE device.

In addition to their use as isolation technologies, microfluidics offer the opportunity to perform on-chip characterization of isolated molecules, including EVs. In this work, we present a simple strategy to immobilize and analyze EVs for multiple markers on a single microfluidic device and perform differentiated immunostaining-based characterization of extracellular vesicles (DICE). This device, composed of four quadrants with a single inlet, captures biotinylated EVs efficiently and facilitates multiplexed immuno- staining to profile their extracellular proteins, allowing for a multiplexed approach for non-invasive cancer diagnostics in the future, **Figure 2-8**. From controlled sample experiments using cancer cell line derived EVs and specific fluorescence staining with lipophilic dyes, we identified that the DICE device is capable of isolating biotinylated EVs with 84.4% immobilization efficiency. We extended our study to profile EVs of 9 clinical samples from non-small cell lung cancer (NSCLC) patients and healthy donors and found that the DICE device successfully facilitates immunofluorescent staining for both the NSCLC patients and the healthy control. This versatile and simple method to profile EVs could be extended to EVs of any biological origin, promoting discoveries of the role of EVs in disease diagnostics and monitoring.

2.5.4.1 Device optimization and on-chip EV immobilization

To isolate and analyze EVs in a non-biased way, we designed an EV isolation device that was antigen independent. For that, we pre-conjugated biotin onto the surface of EVs for immobilization on our microfluidic device, **Figure 2-8A**. This streamlined procedure uses only 20 µL of sample and is sufficient to analyze using immunostaining. After the biotinylation of EVs, we evaluated their size profiles by using NTA, the average vesicle size within tested samples falls within the standard 50–200 nm size distinction of EVs, which agrees with previously reported values.[147,158] The ability of the DICE device to utilize avidin/biotin affinity for EV capture was examined by NTA, fluorescence imaging and scanning electron microscope analysis. First, we prepared two different DICE devices with and without NeutrAvidin conjugation and processed an identical amount of biotin conjugated A549 EVs to evaluate the EV immobilization efficiency of our device. The concentration of initial and resulting (after EV

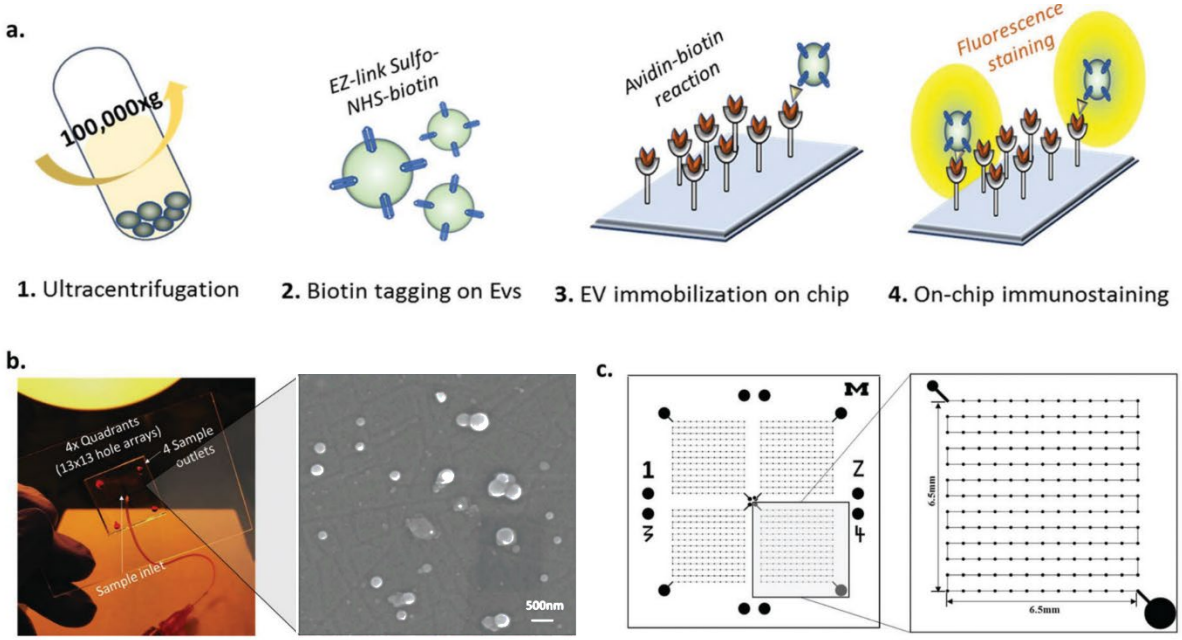

Figure 2-8. Differentiated immunostaining characterization of extracellular vesicle (DICE) chip for extracellular vesicle profiling

A. Procedure of the DICE; **B.** Fabricated DICE device (left) and immobilized extracellular vesicles in DICE device (right), scale bar is 500nm; **C.** Design of the DICE device.

capture) samples were compared using the NanoSight NS300 (Marven Instruments, UK) EV concentration within biotinylated samples measured both pre- and post-capture using NTA.

As seen in **Figure 2-9A**, NeutrAvidin conjugated DICE devices are nearly four times more effective than control devices at immobilizing biotinylated EVs. To confirm this immobilization qualitatively, we used immunofluorescent staining and SEM analysis. Non-conjugated and NeutrAvidin conjugated devices were injected with biotinylated EVs, followed by an incubation periods and PBS wash. Green PKH dye was then applied to each device, staining the lipid bilayer of EVs still present within the device. **Figure 2-9B** shows the significant presence of EVs within NeutrAvidin conjugated devices, demonstrating the effectiveness of the avidin/biotin-based EV capture within the small chambers of the DICE device. To further confirm the presence of EVs in the device, SEM images were taken showing the capture of EVs both in the chambers and along the channels of the device, **Figure 2-9C**. The 25,000× image confirms the previously reported spherical morphology of EVs, further confirming the pure isolation of EVs from our samples.

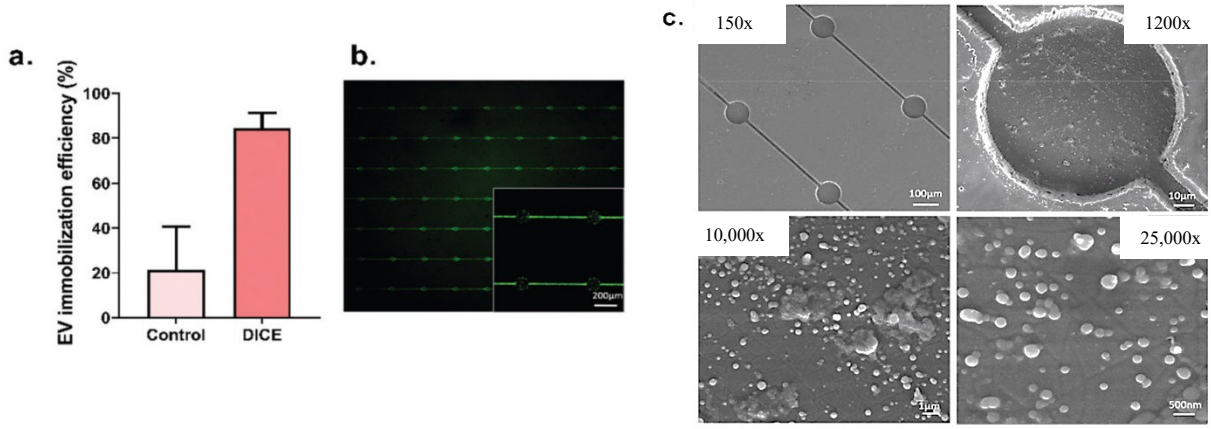

Figure 2-9 Biotinylation and isolation of extracellular vesicles

A. Immobilization efficiency of A549 derived exosomes compared to a control device without streptavidin conjugation; **B.** The immobilized extracellular vesicles stained with lipophilic dye, PKH-green; **C.** Scanning electron micro- scope (SEM) analysis of the on-chip immobilized extracellular vesicles from the lung cancer cell line, A549. Scale bars are 100 µm, 10 µm, 1 µm, and 500nm from top left, top right, bottom left to bottom right.

2.5.4.2 Multiplexed profiling of the EVs from clinical samples

We analyzed our small clinical cohort (n = 5 NSCLC patients, n = 4 healthy control) in terms of nanoparticle tracking analysis and immunostaining results. Multiplexed profiling of EVs from patient samples was carried out using the DICE device. Lung cancer patient and healthy donor blood samples were processed to isolate and then biotinylate EVs for experimental use. EV sample concentrations were measured using NTA analysis before being applied to the DICE device. EV concentration and size results, given in **Figure 2-10A**, demonstrate a 186% greater EV concentration within samples derived from lung cancer patients than in healthy patient samples. While the greater number of EVs in cancer has been previously reported[159,160], this result also indicates the utility of this EV isolation method for lung cancer samples. Recent studies with larger sample size reported no significant difference in total EV concentration in plasma between cancer patients and healthy donors.[161,162] Mean value of particles within both lung cancer patients and healthy donors were reasonably equivalent (116.92 vs. 117.25). Healthy donor and lung cancer patient samples were applied to NeutrAvidin conjugated DICE devices for EV immobilization.

Multiplex profiling was then performed utilizing simultaneous application of PD-L1, Vimentin, CD9, and EGFR antibodies followed by secondary fluorescent antibodies. Fluorescent imaging showed considerable presence of all four antibodies on the surface of the captured EV. As demonstrated in **Figure 2-10B**, which depicts the significant capture of EGFR-expressing EVs, three of the four quadrants of each device were positive in their specified secondary fluorescent channel (FITC anti- mouse IgG2b 488 for PD-L1 and CY5 anti-rabbit IgG 647 for

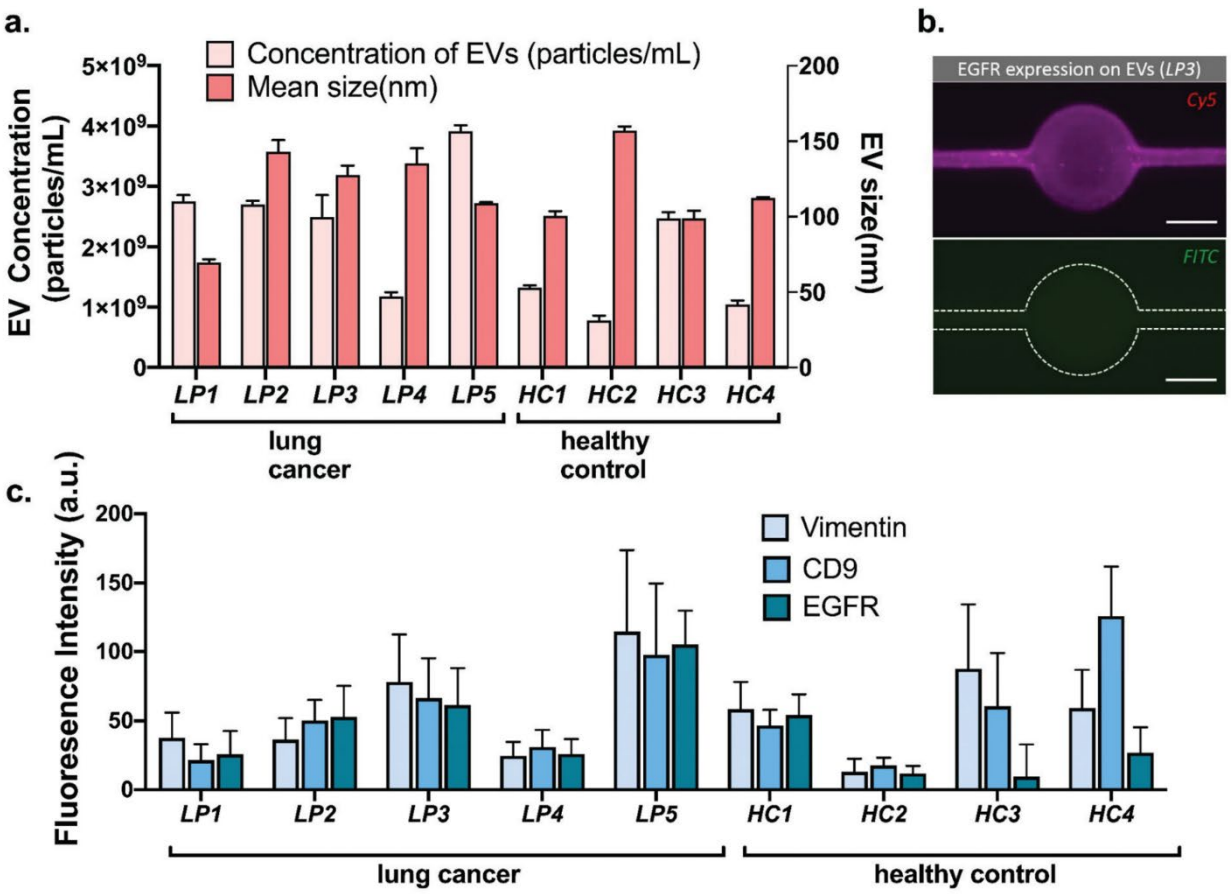

Figure 2-10. DICE-based multiplexing results of 5 different clinical samples

A. EV concentration and size distribution analysis; **B.** Evaluation of EGFR expression on EVs from a lung cancer patient. (Scale bar = 50 μm); **C.** Immunofluorescence intensity analysis of clinical samples using three different protein markers including Vimentin, CD9 and EGFR. Expression in arbitrary units.

Vimentin, CD9, and EGFR). Fluorescent intensity was determined by measuring the intensity of the entire area of each quadrant of the device and subtracting away the background intensity. This normalized the intensity normalizes for fluctuations in background light and small device defects. Additionally, the same volume of plasma was run through each device, to normalize for volume.

The three quadrants that were positive (Vimentin, CD9 and EGFR) were all stained with the same secondary antibody (anti-rabbit IgG 647) while the secondary antibody for PD-L1 was different because of the differing host of the PD-L1 antibody (rabbit vs. mouse), **Figure 2-10C**.

It is possible that the reason there was no positive signal for PD-L1 was because of the differing imaging wavelength as well as the different secondary antibodies. Further testing would be needed to verify that this was a true negative PD-L1 staining. Other than HC1, EGFR intensities of lung cancer patients were found to be higher than that of healthy controls. Vimentin, which was found to be expressed on lung cancer EVs, is also notably expressed in EVs from healthy donors. Because vimentin is one of the most dominant cytoskeletal elements in leukocytes[163], one might want to interpret a high expression of vimentin on healthy EVs with care.

We have found similar results of person-dependent differential protein expression using the quantitative western blot system, the Wes (Protein Simple). The Wes uses capillary action to quantify protein expression from only 3μL of protein lysate. The Wes creates an output of a protein peak, in a.u., with marked molecular weights as quantified based on loaded standards. Using healthy plasma in a titration from 1mL to 4mL, EVs were isolated using ultracentrifugation. The protein was then processed using the Wes for the EV protein CD9, allowing for quantified protein expression. This method is beneficial because of the ability to directly compare protein expression between samples. In **Table 2-1** we see that as plasma volume increases, so does CD9 expression, which makes logical sense. This is corroborated by the result from **Figure 2-2**, where protein concentration appears to increase with increased volume. However, the Wes allows us to see that the CD9 concentration does not increase linearly, which likely is a comment on the efficiency of ultracentrifuge isolation.

Table 2-1 CD9 protein quantification using Wes System

Patient ID:	Plasma volume	Total CD9 quantity (a.u.)	CD9 per mL (a.u./mL)
HC5	1 mL	0	0
HC5	2 mL	4,514	2,257
HC5	3 mL	12,023	4,007
HC5	4 mL	63,256	15,814
HC6	1 mL	12,132	12,132
HC6	2 mL	32,147	16,073
HC6	3 mL	55,478	18,492

We then moved to use the Wes system to profile patient samples for CD9 and found that there is a wide array of concentrations between patients, even when normalized for starting volume of plasma. Interestingly, like from the DICE device, we find that the amount of CD9 on the isolated EVs varies most dramatically by person, and is cancer independent. It is interesting to note that Lung Cancer 1-4 all have metastatic lung cancer, and have dramatically higher CD9, while Liver Cancer 1 has stage II hepatocellular carcinoma and DCIS 1 has ductal carcinoma in situ, or the earliest stage of breast cancer, and they have lower CD9 expression. This could be because the samples have more EVs or higher CD9 expression, further analysis would be needed. Finally, we used two samples to demonstrate the presence of EGFR, a protein of interest in many cancers, in EVs from cell lines (H3255) and Lung Cancer Patient 5.

Table 2-2 CD9 expression in cancer patient derived EVs

Patient ID:	CD9 per mL (a.u./mL)
Lung Cancer 1	38,071
Lung Cancer 2	85,095
Lung Cancer 3	6,308
Lung Cancer 4	10,681
Liver Cancer 1	1,095
DCIS 1	683

Table 2-3 CD9 and EGFR expression using Wes

Sample Type:	Protein:	Protein expression (a.u.)
H3255	CD9	959,580
H3255	EGFR	36,789
Lung Cancer 5	CD9	681,603
Lung Cancer 5	EGFR	704,345

The results and excerpts in this section are found in the following publication:

Y. T. Kang*, **E. Purcell***, T. Hadlock* et al. Multiplex isolation and profiling of extracellular vesicles using a microfluidic DICE device. Analyst 144, 5785–5793 (2019).

2. 6 Discussion

The study of EVs will allow researchers to develop diagnostic and prognostic tests, understand cancer biology, and develop cancer therapeutics. Microfluidic technologies are highlighted when used to isolate EVs from the plasma of cancer patients, allowing researchers to study these nanosized particles more effectively. First, it is critical to validate all novel technologies for their ability to isolate pure EVs or exosomes. This is done to the MISEV standards to ensure consistency within the field, allowing EVs to become clinically relevant biomarkers. The most challenging aspect of validating the purity of isolated vesicles is protein characterization. Western blots are the standard method for probing a sample for proteins of interest. However, this method traditionally uses large volumes or high concentrations of protein to ensure success. It was necessary to first develop western blot workflows and then validate them using microfluidic technologies developed in our lab. Here I presented several novel microfluidic EV, or exosome, isolation and profiling technologies along with the western blot analyses that ensured the purity of the isolated samples.

Using the first device presented, the ^{new}ExoChip, we showed that our PS targeting microfluidic device is capable of capturing tumor-associated exosomes more efficiently than the previous ultracentrifugation method and well-known exosomal protein marker method. Although most previous studies have focused on exosomal proteins, monitoring the exosomal lipids for alteration depending on the disease status might be more suited for clinical use. Exosomes from tumor cells have been shown to have the potential to induce antitumor activity, so their PS expression might help its activation. Thus, the exosomes isolated using this PS-based method might be more effective to induce immune response, suggesting that this subset might be useful for further clinical use. Several prospective studies have shown that PS is expressed on cancer derived exosomes in ovarian cancer and prostate cancer. In addition to these, our studies making use of PS expression on exosomes from lung cancer and melanoma is consistent with previous results. These results empower the theory that cancer exosomes express PS abundantly and may induce some immune response. The present ^{new}ExoChip facilitates the isolation of cancer-associated exosomes, thus allowing us to explore the undiscovered roles of exosomes in cancer progression and metastasis.

The second workflow presented uses the graphene oxide (GO) microfluidic chip to isolate NK cells. As a proof of concept, here we have demonstrated the possibility of a streamlined microfluidic approach to on-chip biogenesis and harvest of natural killer cell-derived exosomes through comprehensive studies using NK cell lines and clinical samples from lung cancer patients. In the future, NK cell-derived exosomes may find a complementary use as both diagnosis and therapeutic tools for patients with cancer. Given the burgeoning interest in this field, it is important to fill the technical gaps pertaining to exosome isolation, harvest, and expansion. We hereby present a highly sensitive method to isolate NK exosomes derived from

viable NK cells using our NK-GO chip. Using the NK-GO chip, we showed that patients with non-small cell lung cancer presented with high numbers of NK and NK cell-derived exosomes compared with healthy donors.

Finally, the potential of the microfluidic DICE device was presented as a multiplexed isolation and protein profiling tool through simultaneous studies using cancer cell derived EVs and plasma samples from cancer and healthy donors. These results demonstrate the ability of the DICE device to successfully capture and multiplex concentrated EV samples. As biotinylation of concentrated EV samples allows for the capture of EVs of unknown origin, the ability to derive the protein profile of EVs on the DICE device enables a rapid and thorough investigation into the vesicles source. The ability to separate and differentiate multiple primary and secondary antibodies within the four channels of the device demonstrates the DICE device's potential as a platform for multiplex profiling involving antibodies other than the four tested here. Although we found that the expression of EV proteins is largely patient dependent, we were able to corroborate this finding using the Wes system, where we found that CD9 expression is highly person dependent.

In conclusion, microfluidic technologies offer the potential to isolate EVs with high purity and at enough for the necessary characterization assays. EV isolation technologies come in many forms depending on the objective of the device, and it is critical that characterization assays are developed and validated for all those technologies. Here I have presented three unique methods for EV isolation and the western blot characterizations that validated their isolation purity, a critical step towards the use of EVs in clinical settings.

Chapter 3 Mutation Monitoring of EV-RNA and EV-Protein in Metastatic NSCLC Patients to Predict Patient Outcomes.

3. 1 Abstract

Extracellular vesicles (EVs) are a stable, abundant biomarker in the blood commonly used to serially profile molecular characteristics of patient tumors through a non-invasive liquid biopsy. In non-small cell lung cancer (NSCLC), identifying the presence of sensitizing and resistance epidermal growth factor receptor (EGFR) mutations dictates treatment plans. Here, EVs isolated from stage IV NSCLC patients were longitudinally monitored for the presence of sensitizing and resistant mutations. EGFR mutations were detected in both EV-derived RNA (EV-RNA) and EV-derived protein (EV-protein), demonstrating the benefits of using EVs for multiplexed cargo analysis that is not possible with other common biomarkers. Using EV-RNA, tumor biopsy matched sensitizing mutations (exon 19 del and L858R) were detected in 90% of patients and resistance (T790M) mutations in 100% of patients. For exon 19 deletion positive patients with 2+ serial timepoints, mutant EV-RNA burden mirrored disease trajectory in 100% of patients.

3. 2 Resulting Publication Information

E. Purcell*; S. Owen*, E. Prantzalos, A. Radomski, N. Carman, T. Lo, C. Subramanian, N. Ramnath, and S. Nagrath. "Detection of EGFR mutations in exosomal RNA and protein mirrors disease status in metastatic non-small cell lung cancer patients." *In submission*

3. 3 Introduction

The widespread adoption of targeted therapies using small molecule tyrosine kinase inhibitors (TKIs) has greatly benefited the 10-30% of advanced non-small cell lung cancer (NSCLC) patients who have sensitizing epidermal growth factor receptor (EGFR) mutations in an otherwise challenging to treat cancer.[164,165] This subset of NSCLC patients harboring sensitizing (L858R and exon 19 deletion (exon 19 del)) EGFR mutations have seen significantly improved survival due to TKIs; yet resistance often occurs in as few as nine months, commonly through the secondary EGFR T790M mutation.[7–9] While it has been documented that additional mutations arise during treatment, traditional tumor monitoring technologies are not commonly used to monitor for these changes. To improve patient care, it is critical to have real-time knowledge of a patient's mutation status, thereby allowing clinicians to alter treatment strategies accordingly. As such, the development of a method for non-invasive longitudinal monitoring offers the potential to drastically improve real-time treatment personalization.

Due the invasiveness and localized sampling of the tumor biopsy, the gold standard in patient care is not frequently used for repeated monitoring, may not result in enough material for testing[2], and may miss mutations carried in other tumor regions. To address these challenges, advancements in liquid biopsies have led to the clinical use of blood-based biomarkers, mostly commonly circulating tumor DNA (ctDNA), to monitor changes in the tumor non-invasively and longitudinally.[166] Yet, ctDNA assays are limited by several notable technical challenges; ctDNA is shed only during cell death[167] and suffers from low abundance[17] and rapid clearance from circulation.[168,169] Hence, ctDNA has the potential to miss the most current molecular changes in a tumor cells that are the most evasive leading to treatment resistant.

Extracellular vesicles (EVs), lipid bilayer bound nanovesicles approximately 30-150 nm in diameter, are a promising alternative blood-based biomarker offering increased abundance and stability compared to ctDNA.[82,83] They are functional vesicles secreted from live cells as a mechanism of cell-cell communication and contain cargo from their originating cells, including DNA, RNA, and protein, which is protected by the lipid bilayer from exogenous degradation while in circulation.[18] The stability of these vesicles in circulation is the key distinguishing factor compared to ctDNA.

Given the tiny amount of cargo carried by these nano-sized vesicles, the development of techniques that can analyze these important carriers is an active area of research in recent times. To date, groups have largely been limited to microRNA or protein to glean information about a patient's disease, and to develop diagnostic and prognostic signatures.[40,170] A final key benefit of using EVs for a liquid biopsy compared to ctDNA is the ability to performed multiplexed analysis of EV-derived RNA (EV-RNA) and EV-derived protein (EV-protein). However, thus far, the detection of mutations carried in EVs in either analyte has been reported by few groups and has been biased towards nucleic acid analysis, with few groups reporting the detection of mutant proteins in extracellular vesicles.

Significantly, mutation profiling in extracellular vesicles is an emerging field, with the first studies focusing on the detection of cancer-specific mutations.[171–174] Mutations carried in EVs have been shown in glioblastoma, pancreatic cancer, and NSCLC. The clinical application has centered on improving detection rates compared to ctDNA alone, commonly by combining ctDNA with DNA and RNA derived from exosomes (a subset of small EVs).[174,175] Most recently, Castellanos-Rizaldos et al. co-isolated exosomal RNA and cell-free RNA for mutation detection from a panel of 30 EGFR mutations. Similar to other studies, this work was limited

based on the use of pre-amplification steps prior to qPCR, which can introduce signal strength bias, for mutation detection and was constrained to a single time point for evaluation. While increasing the detection rate of these rare mutations was achieved, these studies have not demonstrated their utility in a clinical setting and remain single-analyte analyses.

Although there have been no studies using mutations carried in EVs to monitor a cohort of patients, initial evidence suggests this tracking may enable enhanced patient monitoring.[176] Therefore, to provide clinical benefit, the use of mutational profiling in EVs needs to advance beyond single timepoint detection for longitudinal mutation burden monitoring. This approach necessitates a more robust and unbiased analytical techniques to provide molecular information not attainable through radiographic imaging, the current gold standard.

This study followed a cohort of metastatic NSCLC patients to quantify the EGFR mutation burden carried in EV cargo. Sensitive approaches were optimized to profile the mutations carried in EVs at the RNA and protein levels. Specifically, digital droplet-based PCR (ddPCR) was used to analyze the EV-RNA without pre-amplification while mutated protein content of EVs was profiled using western blot. Patients carried at least one sensitizing EGFR mutation (exon 19 del, L858R) based on tumor biopsy and were receiving TKI therapy at the time of enrollment. Moreover, a subset of patients in this study already carried the resistance T790M mutation at the beginning of longitudinal monitoring. Resistance mutations would potentially decrease the efficacy of TKIs, although novel TKIs are being developed to target these mutations as well. Despite the predicted TKI sensitivity, patients had differing therapeutic responses, which is a well-known challenge of TKI therapies. As such, there is a need to develop an enhanced approach to predict who will have favorable outcomes, or who should receive an alternative therapy.

To this end, in this study the cohort was longitudinally monitored for EGFR mutation burden carried by EV-RNA and EV-protein. To date, to the best of our knowledge, there have be no previous studies tracking exclusively EV mutations in a cohort of cancer patients using EV-RNA or EV-protein cargo. This study highlights the potential benefits of dual-monitoring both EV-RNA and EV-protein; distinct roles for EV-RNA and EV-protein were revealed.

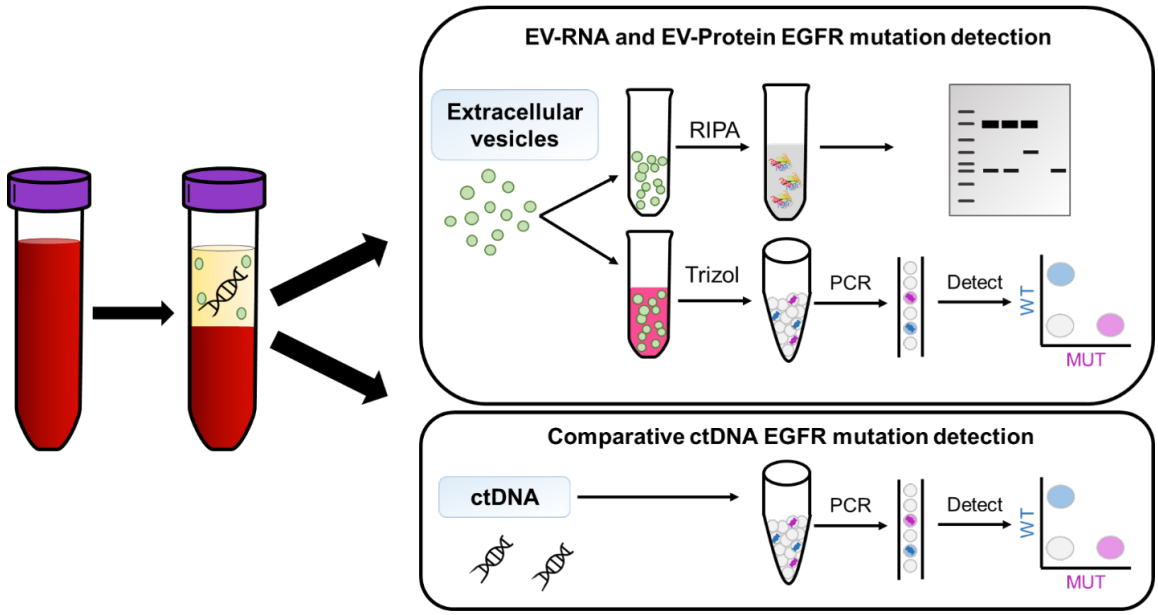

Figure 3-1 Workflow for the isolation and characterization of EV-RNA and EV-protein

3. 4 Methods

3.4.1 Patient Enrollment

All blood was collected following IRB (HUM00119934) approval, and all patients gave their informed consent to participate in the study. All patients had metastatic lung adenocarcinoma. The cohort of patients in this study had known EGFR mutations.

3.4.2 EV Isolation from cell culture and patient plasma

EVs were first isolated and characterized from cells in culture to validate our assays. H1975, H3255 and H1650 cells were grown in RPMI-1640 (Gibco) supplemented with 10% fetal bovine serum (FBS) (Sigma-Alrich) and 1% Antibiotic-antimycotic (Gibco). Cells were grown to 80% confluence before subculturing using 0.05% Trypsin-EDTA (Gibco). To prepare extracellular vesicles, cells were seeded at 3,000,000 cells/100 mm dish (Sarstedt) in complete media. 24 hours after seeding, cells were washed three times with phosphate-buffered saline (PBS) pH 7.4 (Gibco) and incubated for 72 hours in serum-free RPMI-1640 media (Gibco). Cell culture media (CCM) was centrifuged at 2,000 x g for 15 min and frozen at -20°C. This media was processed according to the

Plasma was prepared for EV isolation using one of the following three methods and was stored in the -80C freezer until use.

Plasma prep 1 (Ficoll): Whole blood was collected in EDTA tubes. Samples were prepared using Ficoll-Paque^{TM} PLUS (GE Healthcare) following the manufacturer's protocol. The plasma and leukocyte layers were collected for CTC isolation and effluents were centrifuged following the plasma prep 3 protocol.

Plasma prep 2 (Dextran): Whole blood was collected in EDTA tubes. 1 mL of 6% dextran solution (w/v) was mixed into 5 mL whole blood. The sample sat 1-1.5 hours at room temperature to allow the red blood cells sedimentation. The supernatant was collected for CTC isolation and the effluent was centrifuged following the plasma prep 3 protocol.

Plasma prep 3: Whole blood was collected in EDTA tubes was centrifuged at 2,000xg for 15 minutes at room temperature. The plasma supernatant was collected and frozen at -20°C for up to 30 days.

EVs were isolated from either plasma, plasma preps, or cell culture media using ultracentrifugation, **see Chapter 2 Methods 2.4.1 Ultracentrifugation.**

3.4.3 EV quantification and RNA extraction

After isolation using UC, the EVs that had been suspended in PBS were split for quantification and RNA extraction. EVs were first quantified for size and concentration using NTA using Malvern's Nanosight. Quantification was performed using five 30-second runs at a flow rate of 20 using the brightness setting of 15. The camera detection was set to a level of 4 for all runs. Runs were then averaged with the average and standard deviation between the runs being reported.

The remaining EVs in PBS were lysed using Trizol™ Reagent (Trizol) (Invitrogen) at a 1:10 ratio of extracellular vesicle suspension to Trizol and incubated at room temperature for 5 minutes. A 1:5 ratio of chloroform (Sigma-Aldrich) to Trizol was added and briefly vortexed to mix, then incubated for 2-3 minutes at room temperature. The sample was centrifuged at 12,000xg for 15 minutes. The aqueous phase was collected and mixed in a 1:1 ratio with 70% ethanol (Sigma-Aldrich). Total RNA was purified using the Norgen Single Cell RNA isolation kit (Norgen Biotek Corp.). cDNA was prepared using SuperScript IV VILO Master Mix with ezDNase Enzyme (Invitrogen) following the manufacturer's protocol. All purified RNA and cDNA products were handled in a PCR workstation to prevent contamination.

3.4.4 EV-RNA processing validation using RT-qPCR

Reverse transcription quantitative PCR (RT-qPCR) was used to validate the EV processing conditions to ensure the EVs were not degraded. 20µL TaqMan™ gene expression PCR reactions were prepared using TaqMan™ Fast Advanced Master Mix (Applied Biosystems) in 96-well MicroAmp Fast Optical Plates (Applied Biosystems) and processed on a QuantStudio 3 (Applied Biosystems) using fast cycling conditions. Each mRNA:sample pair was analyzed in technical triplicates.

Table 3-1 TaqManTM gene expression assay IDs

TaqMan™ gene expression assay IDs	
Gene	Assay ID
ACTB	Hs01060665_g1
GAPDH	Hs03929097_g1

3.4.5 Cell-free DNA extraction and mutation profiling

Cell-free DNA (cfDNA) was isolated from the plasma using the QIAamp Circulating Nucleic Acid Kit (Qiagen) following the manufacturer's processing protocol. cfDNA was eluted into 15 µL for ddPCR mutation detection, see below section.

3.4.6 Mutation detection by droplet digital PCR

EGFR mutations were identified by using RainDrop™ ddPCR (RainDance Technologies). In brief 25 µL reactions were prepared using TaqMan™ SNP Assay (Life Technologies), 2x TaqMan Genotyping Master Mix (Applied Biosystems), and droplet stabilizer (RainDance Technologies). Maximum cDNA was loaded into each dPCR reaction. The PCR reaction was

loaded onto the Source Chip (RainDance Technologies) to for droplet generation and collected into an 8-tube PCR strip (Axygen). The PCR tubes were transferred to the thermocycler for 45 rounds of PCR amplification (Bio-Rad). The PCR tubes, containing the samples, were then transferred onto the Sense Machine (RainDance Technologies) where the fluorescence intensity of each droplet was measured.

For the point mutations, L858R and T790M, mutations were considered present based on the detection of one or more positive droplets within the pre-established gates based on positive EV-RNA controls. For exon 19 del, deletions were considered present based on the detection of one or more positive droplets above the threshold. A threshold for detection was determined based on the number of false positive droplets detected using EV-RNA negative controls. The maximum number of false positive droplets detected in any negative control (16 droplets) was used as the threshold for detection. All presented data is represented as the threshold subtracted from the total number of mutant positive droplets counted and any further normalization specified in the respective figure.

Table 3-2 TaqManTM EGFR mutation detection assay IDs

Gene	Assay ID
L858R	AHRSRSV
T790M	AHRSROS
Exon 19 deletion	Hs00000228_mu

3.4.7 EV-protein extraction, quantification, normalization

EV-protein was extracted and western blots were performed according to the methods outlined in **Chapter 2 Method 2.4.3 Protein Extraction and Western Blot.** The primary antibodies used in this work are listed in **Table 3-3.**

Table 3-3 Antibodies for EV-protein analysis using western blot

Target protein	**Dilution**	**Catalog number (Cell Signaling)**
CD9	1:1000	#13174
ACTB	1:1000	#4970
GAPDH	1:1000	#5174S
Calnexin	1:1000	#2679
EGF Receptor L858R Mutant Specific	1:1000	#3197
EGF Receptor exon 19 E746-A750del specific	1:1000	#2085
Anti-rabbit IgG, HRP-linked Antibody	1:1500	#7074S

Western blots normalization was performed following Bio-Rad's Stain Free Gel analysis protocols. Briefly, following protein separation and transfer, the blot is imaged using Bio-Rad's Stain Free Blot imaging setting to capture the total protein per lane. Using Bio-Rad's Image Lab 6.0.1 software, the total protein in each lane is compared and a normalization coefficient determined. After blotting for specific proteins, each band is compared to the total protein of the

lane, adjusted using the normalization coefficient, and quantified as a Normalized Protein Intensity.

3. 5 Results

3.5.1 EV Cargo Carries Mutations from Cells of Origin

To first establish experimental protocols and demonstrate the presence of EGFR mutations in EVs, EVs secreted from lung cancer cell lines with known EGFR mutations were tested for EGFR mutations. EV-RNA and EV-protein were tested using ddPCR and western blot, respectively. ddPCR offers a highly sensitive platform to directly quantify the number of mutant transcripts from bulk RNA without risk of pre-amplification bias[177], allowing for direct comparison between samples and patients. Briefly, the EVs were lysed using Trizol™ Reagent. The Norgen Single Cell RNA kit (Norgen Biotek) was used to purify and isolate the EV-RNA, due to the miniscule amount of RNA contained in these samples. RNA was reverse transcribed and directly loaded onto the RainDrop™ (RainDance Technologies) ddPCR system for analysis.

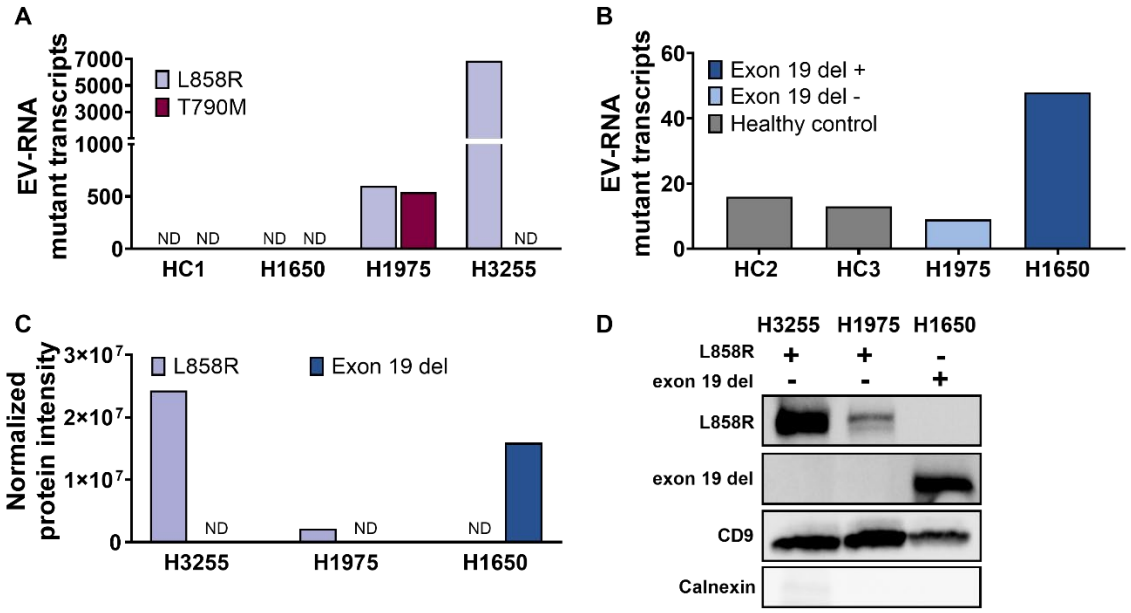

Figure 3-2 EGFR mutations carried in RNA and protein from cell line derived EVs H1975 (L858R/T790M), H3255 (L858R), H1650 (exon 19 del).

A-B. EV-RNA ddPCR droplet counts of lung cancer cell line-derived and healthy plasma prep 1 for **A.** L858R and T790M point mutations and **B.** exon 19 del **C.** Normalized protein intensity for L858R and exon 19 del EGFR mutations from cell line derived extracellular vesicles using western blots.

Matching the cells of origin, EV-RNA derived from H3255 carried a heterozygous L858R mutation **(Figure 3-2A, Figure 3-3)**, EVs from H1975 carried heterozygous L858R and T790M mutations **(Figure 3-2A)**, and EVs from H1650 carried exon 19 del **(Figure 3-2B).** As expected, the assay showed that the EVs were negative for EGFR mutations that were not present originally in their cell line of origin**.** Additionally, in healthy donor EV-RNA (HC1-3), no mutant droplets were detected in these samples using either the L858R or T790M ddPCR assays (**Figure 3-2A, B and Figure 3-3)**. However, the exon 19 del ddPCR assay showed an average background of 14.5 ± 2.12 (n=2) droplets in healthy donor EV-RNA, like the background signal from negative control cell line EV-RNA, **Figure 3-4**. This assay

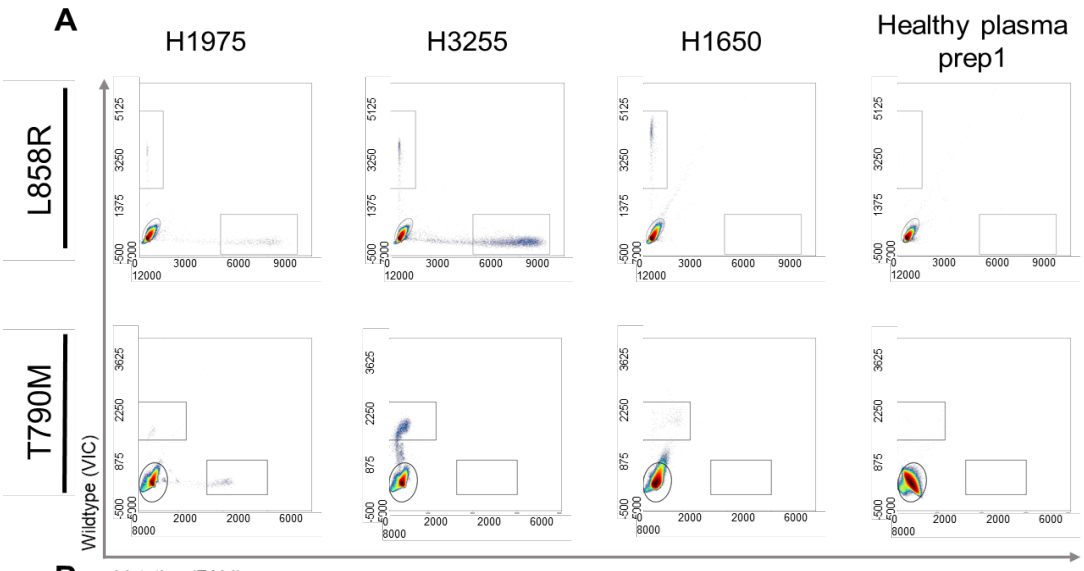

	H1975	H3255	H1650	Healthy plasma prep 1
L858R	+	+	-	-
T790M	+	-	-	-

Figure 3-3 EGFR point mutations, L858R and T790M, detected in lung cancer cell line derived EV-RNA.

A. Representative ddPCR plots for EGFR L858R (top) and T790M (bottom) from EV-RNA generated using control lung cancer cell line derived EVs and healthy control EVs from plasma prep 1. The mutation signal is detected in the FAM channel (x-axis), wildtype signal is detected in the VIC channel (y-axis) and empty droplets are shown in the bottom left of each plot. **B.** Table of EGFR L858R and T790M point mutation status in lung cancer cell lines and healthy donors.

simultaneously screens for 19 different deletion variants using pooled primers, resulting in increased background signal. A threshold for positive detection was determined based on the highest background signal observed among all negative control samples. This threshold for detection was used for all subsequent analysis for NSCLC patient EV-RNA and can be seen on in the images of **Figure 3-4.**

Cell line derived EVs also carried mutant EGFR protein, as demonstrated using western blot. Specific identification of the two activating mutant proteins was achieved. L858R was

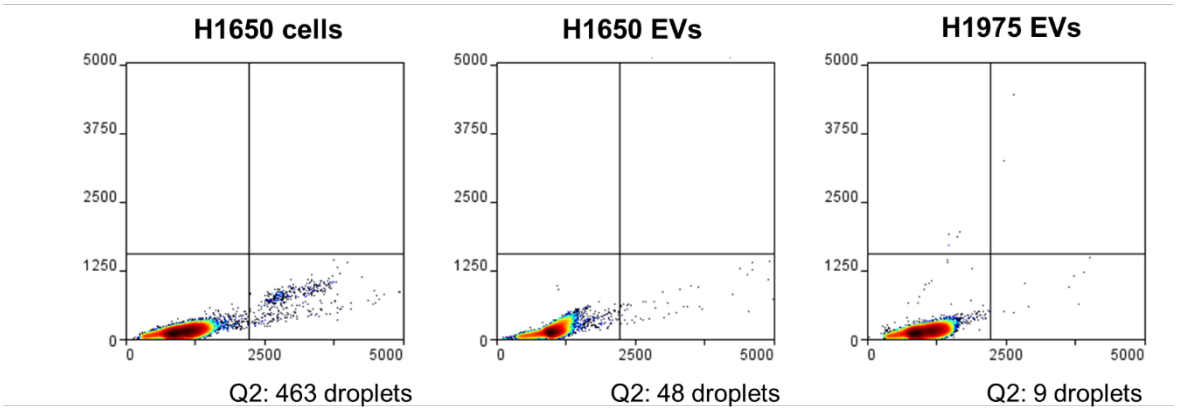

Figure 3-4 Exon 19 deletion mutation quantification and gating for positive detection.

H1650 cells, H1650 EVs, and H1975 EVs were analyzed for the presence of the 19 exon19del variants in the assay.

detected exclusively in H3255 and H1975 derived EVs **(Figure 3-2C, D)**, and exon 19 del only in H1650 derived EVs **(Figure 3-2D)**. A validated T790M antibody is not yet commercially available, and therefore the samples were not tested for this mutation. Each EV-protein sample was additionally profiled for the EV marker CD9, and was shown to be free of cellular contamination based on calnexin, **Figure 3-2C, D**.

Protein intensity for each marker was normalized to the total protein loaded into each lane using BioRad's StainFree Gel technology. Each band was normalized to the total protein per lane, eliminating the need for housekeeping genes which are not equally present in all EVs due to their loading mechanisms and cells of origin.[178] StainFree Gels have been found to be more consistent than housekeeping proteins or Ponceau staining as a loading control and provide the added benefit of controlling for differential loading.[179,180]

3.5.2 Metastatic NSCLC Patient Cohort and Study Design for EGFR Mutational Profiling in EVs

The above established dual EV-RNA and EV-protein mutational profiling was applied to analyze EVs from blood plasma in a cohort of ten metastatic NSCLC patients with at least one kno wn sensitizing EGFR mutation based on primary tumor biopsy. Patients were enrolled after consent and blood was collected under IRB approval. The cohort's median age was 64 years

(range, 45-82 years) and was well distributed between male and female. Full patient demographics can be found in **Table 3-5**.

Table 3-4 Patient EGFR mutation ddPCR and extracellular vesicle characterization

							EV Characteristics	
Patient	Visit	Mutation	Blood volume (mL)	Raw droplet count	Raw droplets without noise	Normalized droplet counts (5mL blood)	Concentration (per mL blood)	Size (nm)
L1	1	exon 19 del	8.6	9	-7	0.00	2.64E+09	141.7 ± 2.2
	2	exon 19 del	18.2	16	0	0.00	1.42E+09	157.3 ± 5.5
	3	exon 19 del	15.2	26	10	3.29	4.66E+09	140.4 ± 10.2
	4	exon 19 del	8	33	17	10.63	1.05E+10	130.4 ± 2.4
	5	exon 19 del	15.2	54	38	12.50	2.43E+09	164.2 ± 2.1
L2	1	exon 19 del	13.6	4	-12	0.00	—	—
	2	exon 19 del	20	35	19	4.75	1.80E+09	149.4 ± 2.6
	3	exon 19 del	12.8	33	17	6.64	2.40E+09	150.0 ± 6.0
L3	1	exon 19 del	6.6	53	37	28.03	—	—
	2	exon 19 del	11.2	39	23	10.27	—	—
	3	exon 19 del	12.8	36	20	7.81	1.58E+09	140.9 ± 4.4
	4	exon 19 del	7.2	21	5	3.47	—	—
L4	1	exon 19 del	6.2	26	10	8.06	—	—
	2	exon 19 del	15.2	33	17	5.59	1.99E+09	139.3 ± 3.3
	3	exon 19 del	10.8	31	15	6.94	2.78E+10	139.0 ± 6.5
	4	exon 19 del	17.2	24	8	2.33	1.22E+10	107.2 ± 4.3
L5	1	exon 19 del	12.6	53	37	14.68	4.06E+09	137.2 ± 11.7
	2	exon 19 del	10.1	28	12	5.94	2.26E+09	158.2 ± 7.5
	4	exon 19 del	19.5	26	10	2.56	2.23E+09	120.3 ± 1.7
L6	3	exon 19 del	6	12	-4	0.00	1.27E+09	157.7 ± 15.0
	4	exon 19 del	11.2	33	17	7.59	1.17E+09	134.1 ± 6.2
L7	1	exon 19 del	4	59	43	53.75	3.98E+09	138.5 ± 4.8
L8	1	exon 19 del	13.4	16	0	0.00	2.01E+09	138.8 ± 1.9

				Raw droplet counts		Normalized droplet counts (5mL blood)		EV Characteristics	
Patient	Visit	Mutation	Blood volume (mL)	Mutant	Wildtype	Mutant	Wildtype	Concentration (per mL blood)	Size (nm)
L9	1	L858R	14	0	4	0.00	1.43	3.26E+09	130.8 ± 2.5
		T790M	14	0	19	0.00	6.79		
	2	L858R	15.2	3	24	0.99	7.89	8.55E+08	167.9 ± 5.5
		T790M	15.2	0	8	0.00	2.63		
	3	L858R	7.6	3	24	1.97	15.79	—	—
		T790M	7.6	4	41	2.63	26.97		
	4	L858R	15.2	5	1	1.64	0.33	—	—
		T790M	15.2	197	326	64.80	107.24		
L10	1	L858R	10.9	0	1	0.00	0.46	3.17E+09	145.9 ± 3.5
		T790M	10.9	0	50	0.00	22.94		
	2	L858R	14.4	0	76	0.00	26.39	6.11E+08	142.5 ± 6.0
		T790M	14.4	0	65	0.00	22.57		
	3	L858R	19.2	0	0	0.00	0.00	—	—
		T790M	19.2	1	29	0.26	7.55		
	4	L858R	10.9	1	3	0.46	1.38	—	—
		T790M	10.9	0	6	0.00	2.75		
	5	L858R	17.4	1	6	0.29	1.72	—	—
		T790M	17.4	0	7	0.00	2.01		
	6	L858R	13.4	6	3	2.24	1.12	1.98E+09	141.3 ± 3.5
		T790M	13.4	0	110	0.00	41.04		
L2	2	T790M	13.6	0	6	0.00	2.21	1.80E+09	149.4 ± 2.6
	3	T790M	20	0	9	0.00	2.25	2.40E+09	150.0 ± 6.0

Seven of the ten patients had samples collected at multiple time points, termed visits. The time between each visit varied depending on patient care, however, the time ranged from 26 to 231 days (mean = 89 ± 40 days) across all patients. The visit notation is used throughout this study to highlight general trends on the utility of patient monitoring using EVs to be compared across patients, however patient specific details and timelines are shown in **Figure 3-9** and **Table 3-4**.

While a plethora of EV isolation methods have been widely developed, including ultracentrifugation[148], microfluidic devices for EV capture[60,181,182], and commercially available kits such as ExoQuick (System Biosciences), EVs in this study were isolated using ultracentrifugation, which offers the widest array of downstream applications and high purity

Table 3-5 Patient demographics for metastatic EGFR NSCLC cohort

Patient	Gender	Age	Race	Stage	Node status	Tumor	EGFR Mutation	Treatments Used	Current patient status
L1	Female	45	White	IV	N3	T4	Exon 19 deletion, w/ PDL1 10%	Osimertinib, carboplatin + pemetrexeb + pembrolizumab, gencitabine	Deceased
L2	Male	72	White	IV	NA	NA	Exon 19 deletion, T790M	Osimertinib, carboplatin + pemetrexeb	Deceased
L3	Male	62	White	IV	N2	T3	Exon 19 deletion	Osimertinib	Stable
L4	Male	70	White	IV	N0	T2a	Exon 19 deletion	Osimertinib	Stable
L5	Male	66	White	IV	N0	T1a	Exon 19 deletion	Osimertinib	Stable
L6	Female	61	White	IV	N0	T2	Exon 19 deletion	Erlotinib	Stable
L7	Female	70	White	IV	N3	T1a	Exon 19 deletion	Osimertinib	Stable
L8	Female	82	White	IV	NA	NA	Exon 19 deletion	Osimertinib	Stable
L9	Female	61	White	IV	N3	T2	L858R, T790M	Osimertinib	Progressing
L10	Female	58	White	IV	N0	T2	L858R, T790M	Osimertinib and pemetrexed	Stable

compared to the above methods[131,183] and is compatible with a range of sample input volumes. After isolation, EV concentration and size was determined using nanoparticle tracking analysis (NTA), **Table 3-4**. Each EV sample was tested for EGFR mutations matching the tumor biopsy result. Additionally, matching ctDNA samples, nine samples across five patients, were tested for the corresponding EGFR mutations to compare detection rates.

3.5.3 EV Isolation Validation

The blood samples were preprocessed to isolate plasma using red blood cell depletion methods, validation experiments demonstrating this material can be utilized for EV analysis are shown in **Figure 3-5**. EVs were isolated from the effluent material generated in a tangential circulating tumor cell (CTC) characterization study.[109] To ensure that the EV cargo was not damaged by RBC depletion prior plasma extraction, standard EV characterization assays for the three plasma isolation methods were performed and compared. 15mL of blood from a healthy donor was divided and processed using 5mL of blood using each of the three plasma generation methods: Ficoll RBC removal followed by centrifugation (prep 1), dextran RBC removal followed by centrifugation (prep 2) or centrifugation alone (prep 3). For all reported values, error bars are indicative of the average and standard deviation of 3 technical replicates.

EV size and concentration of the three plasma prep methods was measured using NTA and the size of the EVs did not vary with isolation method; yielded vesicles were within the standard range for EVs (50-160 nm), **Figure 3-5A.** The concentration has been normalized to starting blood volume, reported values are per mL of original blood volume. The measured concentration of the EVs isolated using plasma prep 2 was dramatically higher than the concentration from plasma prep methods 1 or 3. The higher concentration could be a result of

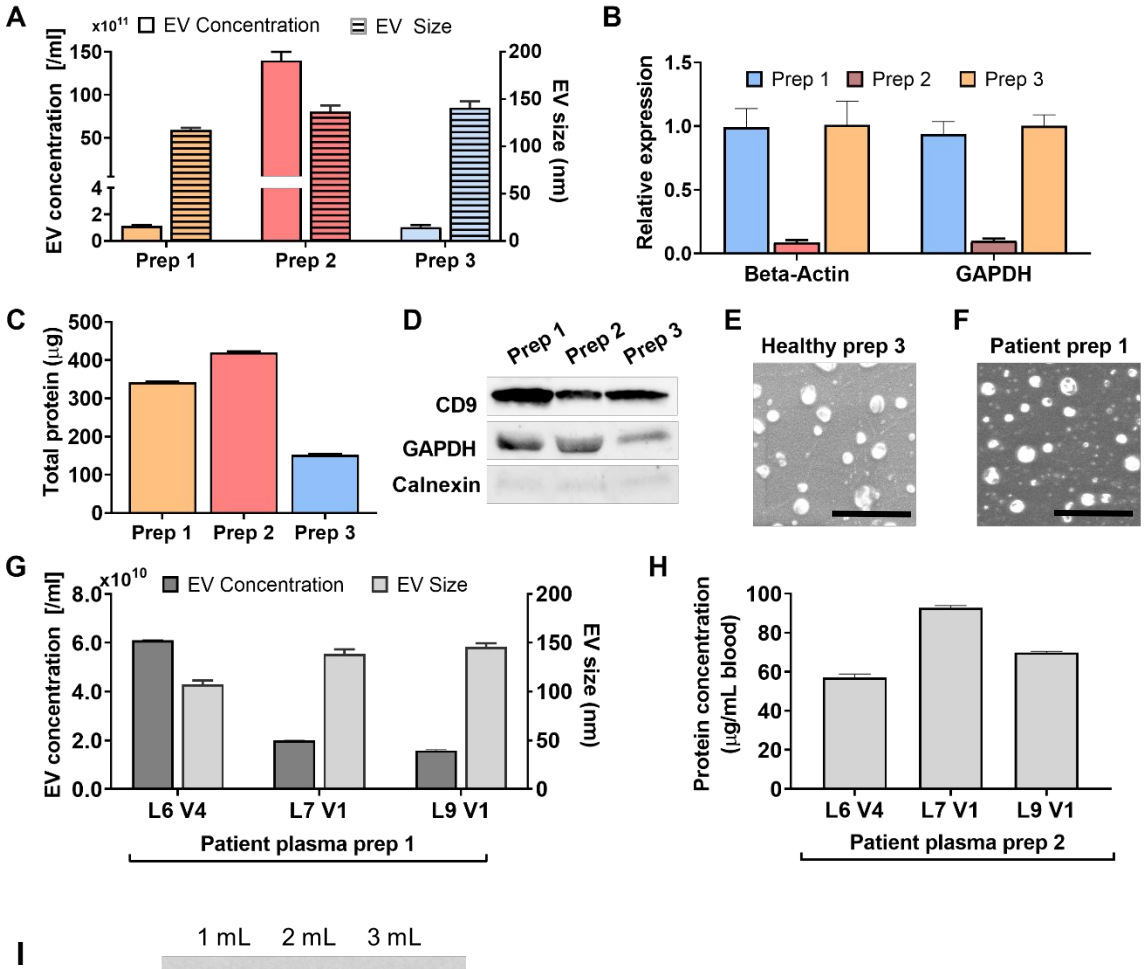

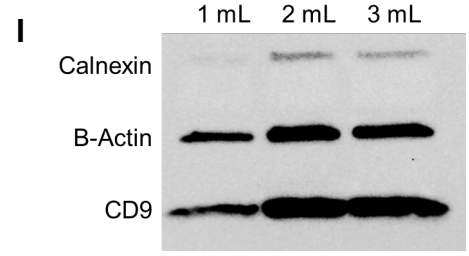

Figure 3-5 Validation of EV isolation techniques for different plasma preparations

residual dextran macromolecules being measured.[184] Another possibility is that dextran allows for more efficient recovery of EVs during ultracentrifugation. Further experiments would be needed to verify the cause of this increase.

The relative abundance of house-keeping genes, ACTB and GAPDH, was measured using RT-qPCR. Using plasma prep 3 EVs as the baseline for comparison, plasma prep 1 EVs had similar levels of the two genes, whereas plasma prep 2 EVs had less than 10% comparatively, **Figure 3-5B**. One explanation for the result is that the differences in EV-RNA

yield is from inefficiencies in EV lysis in the presence of remaining dextran molecules. Another is that the EV-RNA was damaged during the dextran processing, leading to lower abundance. Further testing would be needed to verify the reason. Because the detected levels of housekeeping genes were similar for plasma preps 1 and 3, plasma prep 1 samples were used for EV-RNA characterization.

EV-protein characterization was performed using microBCA and western blot. There was slightly higher protein yield from plasma prep 2 than plasma prep 1, and both were higher than plasma prep 3, **Figure 3-5C.** Western blot analysis of the three plasma prep methods showed similar expression of the following proteins: exosomal marker CD9, housekeeping gene GAPDH, and contamination marker calnexin, **Figure 3-5D.** The cellular contamination marker, calnexin, was validated to be negative using a titration of plasma-derived EVs ranging from 1-3mL of plasma used. To do so, the samples were processed without performing the 12,000xg spin in the ultracentrifugation protocol. The presence of the calnexin band indicates the success of this antibody along with the necessity of the semi-final centrifuge step to remove cellular contamination.

Scanning electron microscopy images of EVs isolated from a healthy control prep 3 and a patient prep 1 to demonstrate successful EV isolation, **Figure 3-5E, F.** Scale bar indicates 1 μm.

For additional verification, NSCLC patient plasma preps were processed either (1) directly into PBS for NTA quantification or (2) into RIPA lysis buffer for protein analysis. Three plasma prep 1 samples were measured using NTA and were found to have similar size, 130 ± 17nm, and concentration, $3x10^{10} \pm 2x10^{10}$, **Figure 3-5E**. From the same patients and time points, the plasma prep 2 samples were measured for EV-protein quantity using microBCA with an average of, 73 ± 18 μg/mL blood in 150 μL of protein lysate from 5mL of blood**, Figure 3-5F**.

In summary, it was found that the plasma prep 1 would be best used for RNA studies, while plasma prep 2 was best used for protein studies.

3.5.4 Longitudinal Detection of EGFR Mutations in EV-protein

EV-protein was isolated from the plasma of four patients over 3-4 visits. EV-protein was tested for sensitizing mutations exon 19 del or L858R based on initial biopsy. EGFR mutations

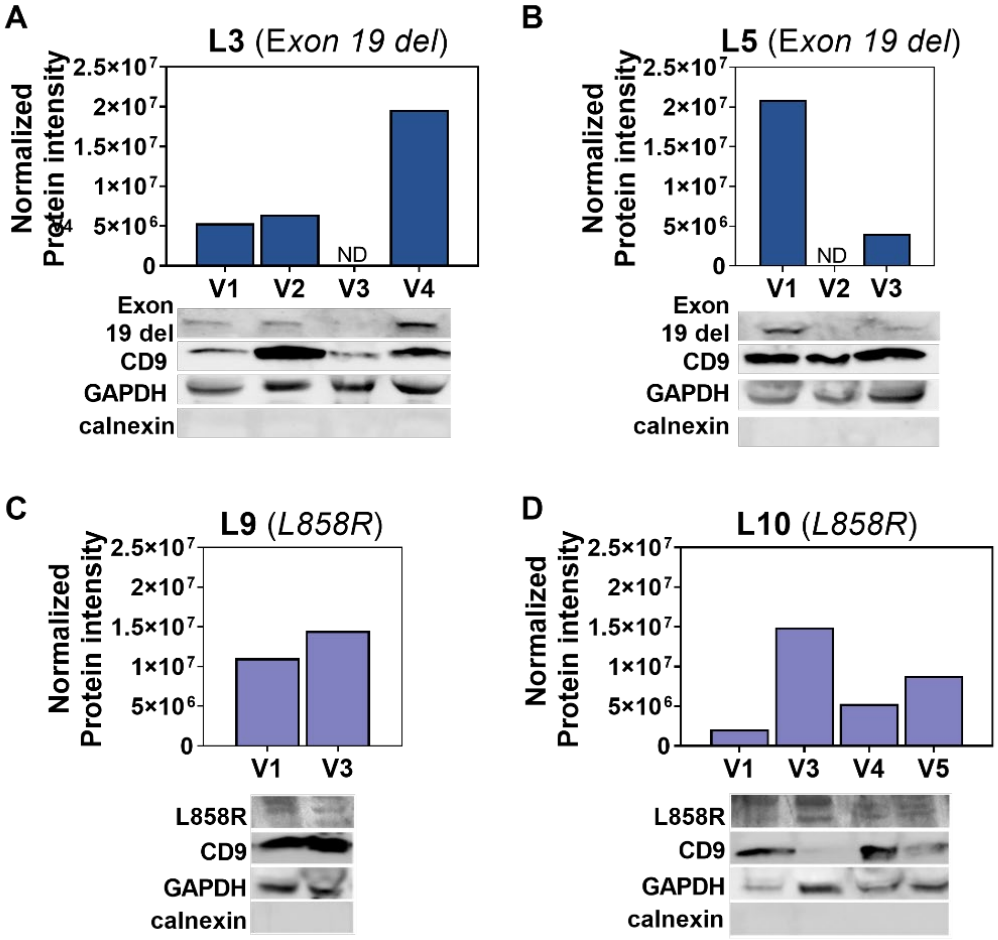

Figure 3-6 Detection of EGFR mutations in EV-protein.

A-D. EV-protein with detected mutant EGFR from patients across multiple visits from **A.** L3 with exon 19 **del B.** L5 with exon 19 del **C.** L9 with L858R, and **D.** L10 with L858R. Samples were additionally screened for CD9, GAPDH, and calnexin. Normalized mutant EV-protein is quantified above each western blot using BioRad's StainFree Gel technology to normalize to the total protein as quantified by imaging the Stain Free Gel after transfer to a PVDF membrane. ND = not detected.

in the EV-protein were detected using western blot in samples from 4/4 (100%) patients, two patients with exon 19 del mutations and two with L858R mutations. Patients L3 and L5 have moderately identifiable bands for exon 19 del, while having various levels of CD9 and similar GAPDH bands, **Figure 3-6A, B**. The two patients demonstrated similar detection rates, with one patient having exon 19 del EV-protein detected in 3/4 of samples (L3) and the second in 2/3 of samples (L5). Interestingly, one patient has a trending increase in their mutated EGFR EV-protein, while the other has a steady decrease, despite both being clinically stable through all timepoints.

Conversely, the L858R band is present in samples from patients L9 and L10, but less distinct compared to exon 19 del in L3 and L5, **Figure 3-6C, D.** While the bands are less distinct, there is L858R EV-protein at all the timepoints tested. The second patient, L10, shows a net increase in L858R EV-protein over time compared to visit one, although the amount does not increase at all visits. The less optimal bands could be the result of EV packaging, the protein itself, or several other challenges. However, the CD9 and GAPDH proteins are highly variable between samples for the patients with L858R and are less clean than would be expected from either cells or healthy EVs.

EGFR mutations found in EV-protein demonstrate the potential to use EVs as multiple cargo biomarkers. This finding marks the first demonstration of EGFR mutations detected in patient-derived EV-protein. Full western blots can be found in **Figure 3-7.**

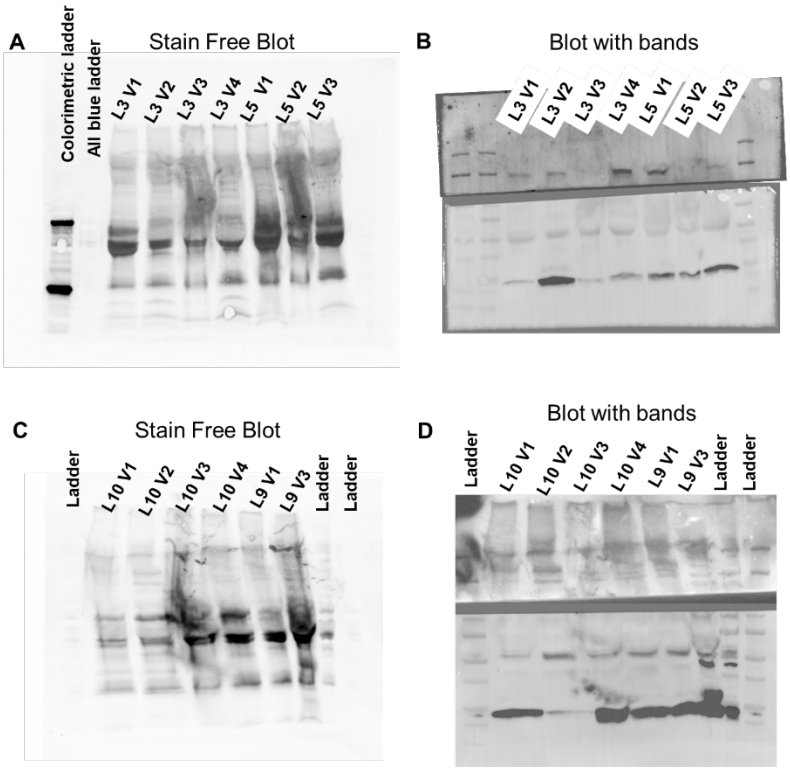

Figure 3-7 Full western blot images for patient EV protein samples

A, C. Stain Free Blot images showing the total protein per sample, used to perform quantification of specific bands.
B, D. Bands for 4 proteins of interest. The top image in each part demonstrates an EGFR mutation, either exon 19 del (**Figure 3-7B)** or L858R (**Figure 3-7D).** All samples were additionally tested for calnexin (MW ~90-100kDA), GAPDH (~50-70kDA), and CD9 (~25-35kDA). Calnexin, a cellular contamination marker, is negative or under expressed in all samples. GAPDH has varying expression levels, indicating the need for total protein quantification. CD9 is expressed in all samples, at varying levels.

3.5.5 EGFR Mutations in EV-RNA Detected in Metastatic NSCLC Patients

In compliment, EV-RNA was isolated from 10 patients with multiple samples (n=33 total samples) collected from each of these patients at different time points (up to six visits) through their course of treatment. The mutation burden was evaluated in each sample, defined as the number of mutant EGFR droplets detected using ddPCR normalized to 5 mL of starting blood

volume. Exon 19 del was detected in 7/8 patients, **Figure 3-8A**. Patients varied as to the number of timepoints with exon 19 del positive EV-RNA, with some patients having mutant EV-RNA at 100% of timepoints (L3, L4, L7), and one having no detected exon 19 del, L8, **Figure 3-8B**. It is important to note that the patients had varying number of visits, ranging from 1-5 (average =

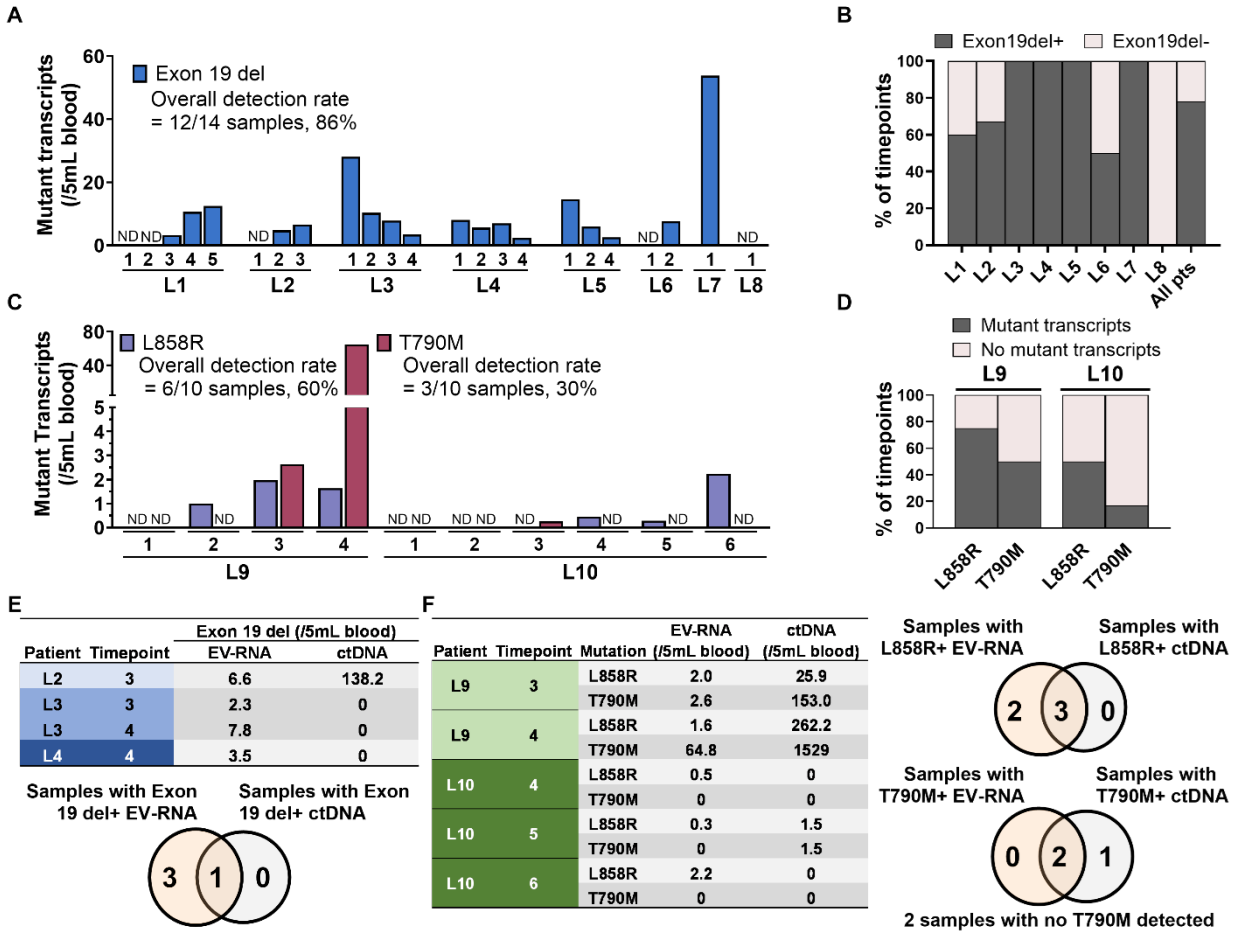

Figure 3-8 Detection of EGFR mutations in EV-RNA samples from metastatic NSCLC patients.

A. EGFR exon 19 deletion transcript concentration per timepoint for the eight patients pre-identified as being exon 19 del positive. **B.** Percent of time points that tested positive for EGFR exon 19 del mutations per patient. **C.** Mutant EV-RNA concentration for both L858R and T790M mutations across time points for two patients. **D.** Percent of time points that tested positive for L858R and T790M mutations by patient. **E-F.** Comparative concentration of EGFR mutations found in ctDNA and EV-RNA along with Venn diagrams displaying the overlap in samples with detected mutations in EV-RNA and ctDNA for **E.** four samples with known exon 19 del mutations and **F.** five samples with known L858R and T790M mutations.

2.88, n=8). Taken together, the positivity rate across all samples for exon 19 del was 78% (n=18/23).

The remaining two patients L9 & L10 co-harbored L858R and T790M mutations. Although the data is collected from only two patients, there was a larger range in the number of mutant transcripts detected for the two point mutations than were observed for exon 19 del. Patient L9 had a range of 0-80 T790M transcripts detected, compared to L10 with a range from 0-0.5 transcripts per 5mL blood, **Figure 3-8C**. Additionally, the point mutations were detected less frequently per patient compared to the patients with exon 19 del. L858R was detected in 75% of timepoints in L9 and in 50% of time points in L10. Even more modest was the detection of T790M, found in 50% of visits in L9 and only 17% of visits in L10, **Figure 3-8D.**

For nine samples, matched ctDNA was tested alongside EV-RNA for the EGFR mutations using the same ddPCR technique. For patients with exon 19 del, ctDNA was found in only 1/4 samples tested, compared to 4/4 EV-RNA samples, **Figure 3-8E.** Similarly, five L858R/T790M samples had dual testing and results show that 3/5 samples tested positive for L858R in both ctDNA and EV-RNA, while the remaining 2/5 were positive for L858R in only EV-RNA. The T790M was detected less frequently in both ctDNA and EV-RNA, with only 2/5 samples having mutations in both ctDNA and EV-RNA, one having only ctDNA mutations, and two having no detected T790M mutations, **Figure 3-8F**.

3.5.6 Longitudinal Monitoring of EGFR Mutations in EV-RNA Mirrors with Disease Trajectory

To explore the utility of EV-RNA in patient care, transient mutant EGFR burden was compared to the clinical outcomes of seven patients across up to six visits, **Figure 3-9**. At each

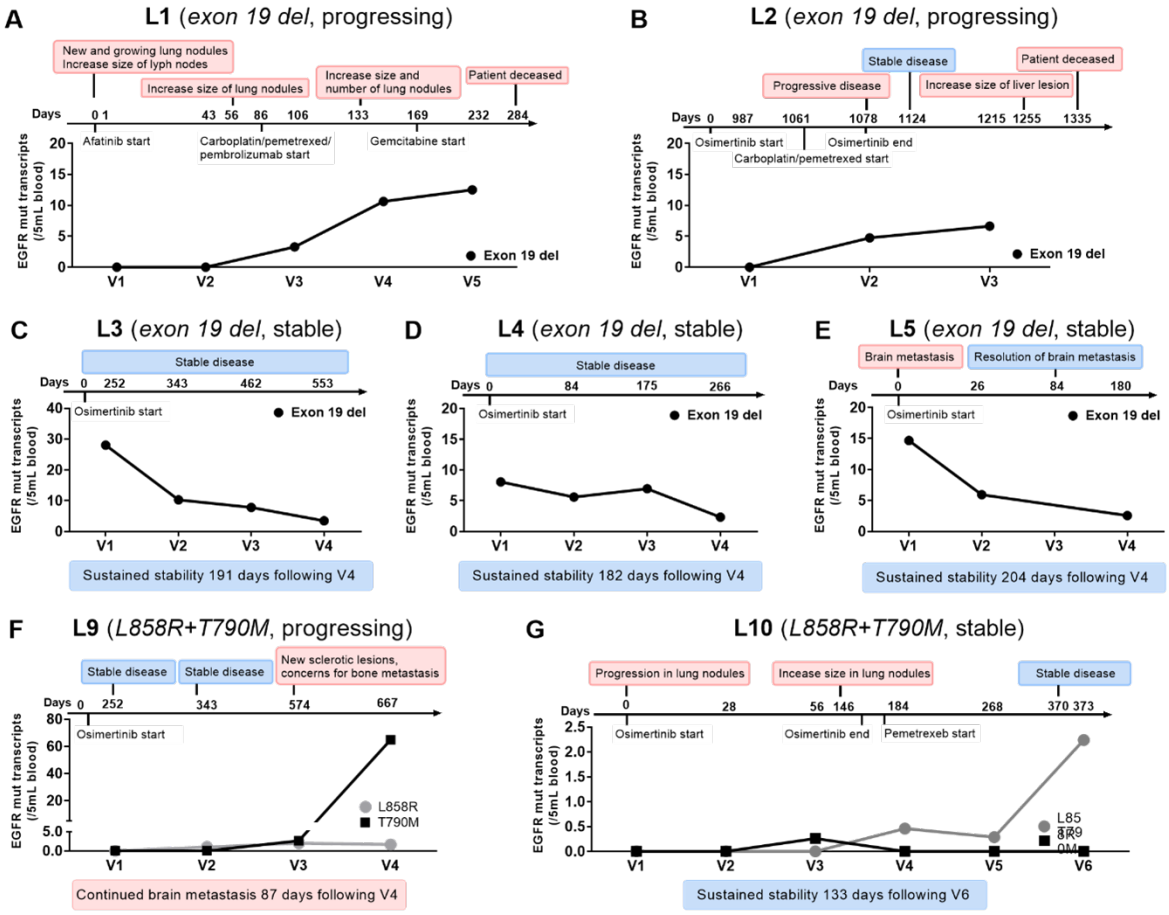

Figure 3-9 Clinical data timeline mapped to the mutant EV-RNA at each visit.

A-G. Normalized droplet counts for EGFR mutations in EV-RNA using ddPCR. A timeline with each patient's clinical data is displayed in days from start of treatment. Clinical data showing disease progression is shown in red text boxes, while stable disease is shown blue text boxes.

timepoint, response to therapy is classified as either a stable (n=17 samples) or progressing (n=22 samples) based on available clinical data corresponding to each blood draw visit following the guidelines established in RECIST (Response Evaluation Criteria in Solid Tumors) [34]. EV-RNA was determined to mirror disease status when an increase in mutation burden occurred at the same timepoint as progression, or conversely if a decrease or no change in mutation burden occurred at a timepoint when a patient was determined to have stable disease, **Figure 3-10A.**

Each patient's progression was classified based on overall disease trajectory into one of three categories based on trend in EV-RNA burden over time: consistently progressing (n=2 patients) **Figure 3-10B**, consistently stable (n=3 patients), **Figure 3-10B**, and divergent (n=2 patients), **Figure 3-10C**. The two patients with consistent progression, L1 and L2, both carried

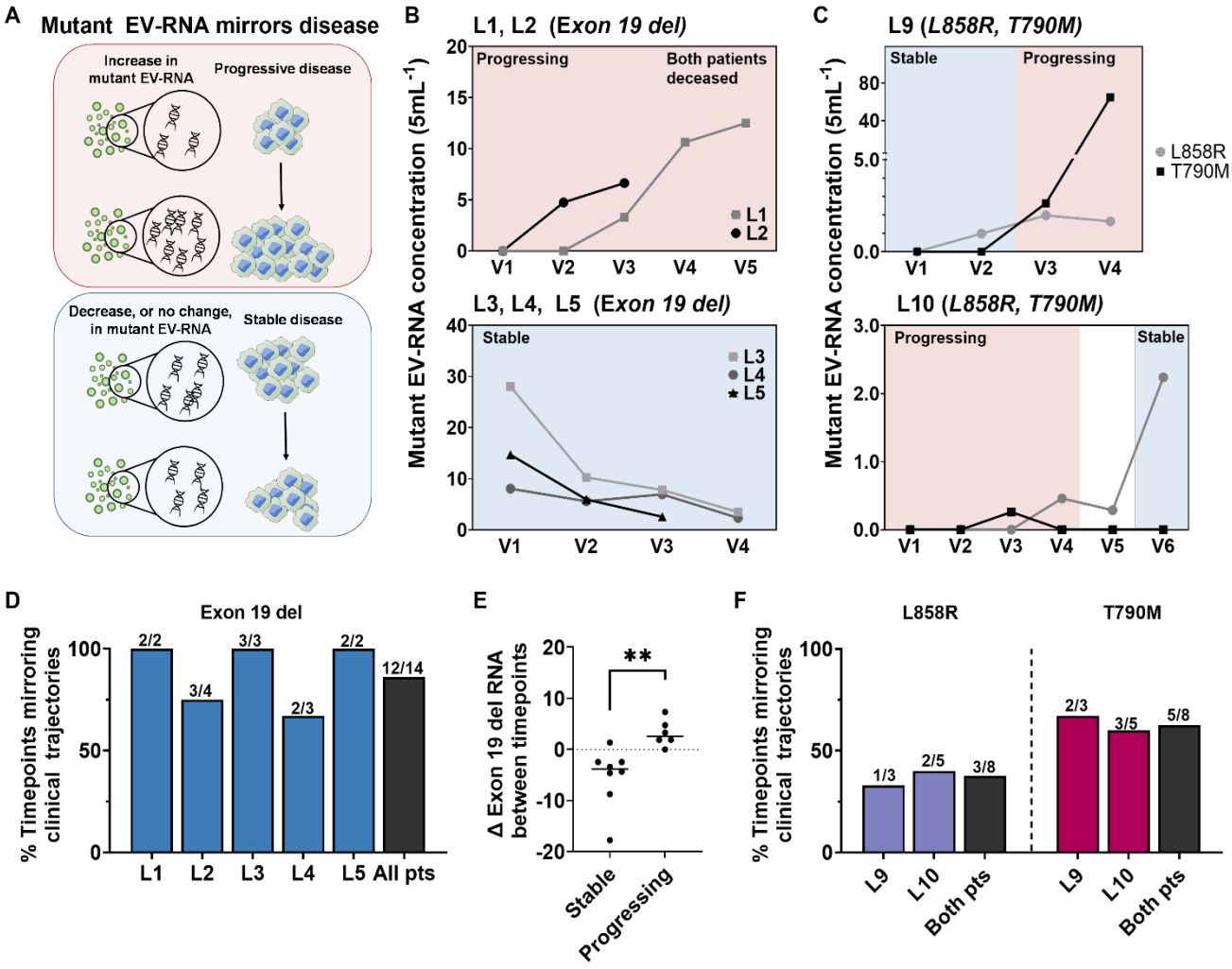

Figure 3-10 Changes in EGFR mutation burden in EV-RNA mirror disease status.

A. Schematic demonstrating EV-RNA mirroring disease status. An increase in mutant EV-RNA mirrors progressive disease, while a decrease or no change in EV-RNA would mirror stable disease. **B.** Mutant EV-RNA concentration for exon 19 del patients across multiple visits for patients with consistently progressive (top) or consistently stable (bottom) disease **C.** Mutant EV-RNA concentration for L858R/T790M in divergent patients, L9 (top) and L10 (bottom) across multiple visits. **D.** Percent of EV-RNA samples drawn at a timepoint when EV-RNA mutation burden mirrors disease status for patients with exon 19 del. **E.** Change (Δ) exon 19 deletion mutation burden in EV-RNA between timepoints for patients who are clinically stable compared to progressing, p-val = 0.0059 using an unpaired t-test. **F.** Percent of EV-RNA samples drawn at a timepoint when EV-RNA mutation burden mirrors disease status for patients with L858R and T790M mutations.

exon 19 del and had increasing EV-RNA mutation burden that mirrored disease progression, **Figure 3-10B**. Both patients had no detectable EV-RNA mutations in their first visits, however as their disease progressed, the mutation burden increased with each visit. L1 had increased size of lung nodules between visits 2 and 3, which correlated with the onset of detectable exon 19 del in their EV-RNA. Between visits 3 and 4, the size and number of lung nodules both increased, corresponding with a mutation burden increase of 223%. Similarly, patient L2 had progressing disease between visit 1 and 2, which was reflected by the onset of EV-RNA mutation detection. While the patient was clinically stable between visit 2 and 3, only a modest 40% increase in mutation burden was observed. L2's disease further progressed after visit 3. Ultimately, both patients were placed in hospice shortly before their final time point in this study and are now both deceased.

The second category, comprised of patients L3-L5 who were consistently stable, all carried exon 19 del. They had sustained, clinically stable disease and showed a downward trend in their EV-RNA burden at nearly every time point, **Figure 3-10B**. L5 initially had brain metastases and high levels of EV-RNA, however each subsequent time point demonstrated radiologically monitored resolution of brain metastases. This observation of sustained decreased EV-RNA burden is notably different than what was observed in L2, which showed a sustained increase in mutant EGFR burden, despite temporarily being classified as having clinically stable disease. All three patients with sustained clinical stability, L3-5, have been stable for 191, 182, and 204 days, respectively, since the final EV-RNA time point **(Figure 3-9)**.

In the last category, patients L9 and L10 each carried L858R and T790M and showed divergent clinical trajectories. L9 had undetectable levels of L858R and T790M EV-RNA at the initial visit and was clinically stable. However, as the patient progressed, EV-RNA burden of

L858R and T790M increased between visits 3 and 4, 83% and 2460% respectively (**Figure 3-10C).** At 87 days after the final blood draw, L9 has continued to show progression, and has brain metastasis. Conversely, L10 was progressing while on TKI therapy but did not have any detectable L858R or T790M EGFR burden. However, when the patient's therapy was switched to chemotherapy (pemetrexed) and the disease stabilized, the L858R mutation became detectable and increased by 672% between visits 5 and 6 in EV-RNA, **Figure 3-10C.** This patient has continued to be clinically stable for 133 days since the final blood draw **(Figure 3-9)**.

EV-RNA exon 19 del burden mirrored clinical trajectories at 12/14 timepoints across all five patients with 2+ timepoints, with the definition of mirroring being shown in **Figure 3-10A**. Patients ranged from having 67% to 100% of timepoints where EV-RNA mutation burden mirrored disease trajectory, **Figure 3-10D**. When quantitatively compared, the change in exon 19 del EV-RNA transcripts (ΔEV-RNA) between timepoints is significantly lower, quantified using an unpaired t-test with a p-val <0.05, for patients who are stable compared to progressing (p-val = 0.0059, two-tailed t-test), **Figure 3-10E.** Conversely, the two patients with L858R/T790M mutations saw 33% and 40% mirrored timepoints for L858R EV-RNA and 67% and 60% mirroring for T790M EV-RNA, **Figure 3-10F**. It is important to note that for both point mutations, especially for T790M, the detection rate was low, therefore conclusions cannot be accurately drawn about the relationship between ΔEV-RNA burden and disease progression.

3. 6 Discussion

Using ddPCR and western blots, EVs isolated from lung cancer patient plasma were analyzed for EGFR mutations. In this pilot study, the utility of EV-RNA and EV-protein is demonstrated to not only screen for the presence of mutations, but to dynamically monitor

patient disease status. Mutant EV-RNA was detected in 9/10 patients, and for 6/7 patients who were longitudinally monitored, mutant EV-RNA burden mirrored clinical trajectory. Within patients who had exon 19 del, ΔEV-RNA mutation burden strongly indicated disease trajectory, demonstrating that a single time point may be insufficient to assess patient status. The power of liquid biopsies enabled multiple time points from each patient to be collected.

While evidence from this pilot study suggests the rate of increase in EV-RNA mutation burden may be linked with progression severity, larger studies are needed to investigate this. For the patients with exon 19 deletion, both patients who had consistent progressive disease succumbed to their disease and are now deceased. These patients had similarly consistent increase in EV-RNA mutation burden. Conversely, the three patients with decreasing EV-RNA exon 19 del burden have remained clinically stable for an average of 192 ± 9 days after the final blood draw. These patients saw consistently decreasing EV-RNA mutation burden that mirrored their stable disease status. This was further highlighted by the finding that there is a significant difference in the exon 19 del ΔEV-RNA burden between timepoints between stable and progressing patients. These results indicate that changes in EV-RNA mutant burden may be an early indicator of clinical stability and perhaps even indicate disease progression before clinical monitoring methods.

Of the two patients with L858R/T790M mutations, one patient's EV-RNA burden mirrored disease trajectory, while the other did not. L9 has had sustained progressive disease 87 days after the final blood draw. Conversely, L10, after switching from a TKI to chemotherapy between visits 4 and 5, has remained clinically stable for 133 days after the final blood draw, despite an increase in L858R EV-RNA. The change from TKI therapy to chemotherapy during this study could impact the utility of targetable mutations carried in EV-RNA for patient

monitoring. Without the use of TKIs specifically targeting mutant EGFR, an increase mutant burden may not indicate treatment resistance in the tumor. Therefore, while EV-RNA may mirror disease trajectory for patients receiving targeted therapy, this may not extend to patients receiving other treatment types, such as chemotherapy and further studies are needed to investigate this.

Additional studies with larger cohorts are needed to validate these findings, however, this study presents initial evidence that increase in EV-RNA indicates progression for patients receiving targeted therapy. Future studies are needed to determine if EV-RNA can be used to detect progression prior to current techniques. Of interest, L6, only had two time points collected but saw an upward trend in their burden despite being clinically stable thus far. The preliminary findings presented here warrant a recommendation that the clinical trajectory of this patient should closely be monitored for indicators of disease progression.

While EV-protein was detected in samples from four patients, there was not an observed correlation between EV-protein burden and EV-RNA burden and there were too few patients to make assessments of correlation to disease. Previous studies in cell lines have shown that when exposed to TKIs, EGFR mutations result in differential protein stability compared to wildtype [35]; Treatment with the TKI erlotinib led to protein degradation in a mutant dependent manner, without significantly changing the transcriptomic expression. Additionally, osimertinib, the primary TKI the patients in this study were receiving, has been suggested to reduce protein stability in both wildtype and T790M mutant EGFR. The decreased stability of EGFR protein due to TKI treatment can lead to increased cellular protein turnover thereby either (1) reducing the amount of protein packaged into EVs or (2) leading to increased degradation of either cellular protein or EV-protein, both of which would reduce the quality of the proteins found in

EVs, as seen in this study.[185] Further studies will need to be performed to elucidate information about the mutated protein found in EVs.

Liquid biopsies hold the potential to address spatial heterogeneity and longitudinal monitoring limitations. However, the only FDA-approved liquid biopsy test, the Cobas v2, for mutation detection, relies on ctDNA. While capable at detecting the presence of new mutations, this test is still currently considered a "rule in" test, with the recommendation of a tissue biopsy to confirm a mutant negative result.[186] Compared to ctDNA, EVs demonstrated a more robust detection of exon 19 del, and similar detection rates for point mutations L858R and T790M, **Figure 3-8E, F**. To avoid splitting the sample or using pre-amplification steps, this study screened solely for EGFR mutations detected by tumor biopsy, therefore future studies are needed to expand further to screening for mutations in EV-RNA not originally detected by tumor biopsy. By instead using EVs, liquid biopsy mutation screening has the potential to advance beyond the current "rule in" test.

This work lays the groundwork for future studies to establish the utility of mutations found in EV cargo for patient care. In this novel proof of concept study, EVs were screened for previously identified EGFR mutations carried by each patient. Changes in EV-RNA correlated with disease trajectory; however, the clinical implications of EV-protein remain unclear. The utility of EV mutation monitoring warrants further investigations across additional mutations and cancer types. Further, the dual analysis of EV-derived cargo has the potential to go beyond monitoring and be used in lieu of a tumor biopsy for non-invasive screening for both sensitizing and resistance mutations in EGFR across a patient's treatment course. This minimally invasive approach could be integrated into the standard of care enable more rapid identification of treatment resistance and allow for timely treatment changes, overall improving patient care.

Chapter 4 Circulating Tumor Cells Isolated from Stage III NSCLC Patients Using Microfluidic Graphene Oxide (GO) Chip Predicts Progression Free Survival

4. 1 Abstract

Stage III non-small cell lung cancer (NSCLC) patients commonly undergo radiation treatment (RT), with imaging scans being the standard of care for determining disease progression both during and after RT. However, imaging technologies only detect progression after it has occurred, which may be well after tumor growth or disease progression has begun. In this work, we determined whether CTC metrics, including the number of CTCs, change in the number of CTCs during treatment, and PD-L1 expression on CTCs, can be used as a blood-based biomarker to predict patient outcomes in stage III NSCLC. At six timepoints through treatment, blood from 26 stage III NSLC patients was processed for CTC isolation and analysis using the immunoaffinity graphene oxide (GO) microfluidic chip. The primary endpoint was disease progression, either locoregional, distant, or death. CTCs were present in 100% of patients (n=26/26), and at 93% of timepoints (n=102/110). The number of CTCs decreased significantly from pre-treatment (Pre-TX) to mid-radiation ($p=0.02$, paired two-tailed t-test), after radiation ($p=0.04$, paired two-tailed t-test), and mid-immunotherapy ($p=0.02$, paired two-tailed t-test) timepoints. By calculating the percent decrease in CTCs from Pre-TX to mid-radiation therapy, it was found that patients who had a large decrease in CTCs had sustained stability. Conversely, patients who had an increase in CTCs during radiation therapy were likely to have progression. Patients were split in two even groups, defined by a 75% change in CTCs between Pre-TX and mid-radiation. A decrease in CTCs of less than 75% precluded a significantly shorter PFS time, 7

months vs 21 months average monitoring time with no progression ($p = 0.005$, log-rank test). Secondarily, it was found that the three patients who had progression while receiving anti-PD-L1 immunotherapy had a quantity of PD-L1+ CTCs greater than the median at all time points. Survival analysis shows that having >50% PD-L1+ CTCs at Pre-TX potentially predicts a shorter PFS. In conclusion, CTCs isolated using the GO chip are a potential blood-based biomarker to predict patient outcomes in stage III NSCLC patients undergoing RT.

4. 2 Resulting Publication Information

E. Purcell, Z. Niu, S. Owen, M. Grzesik, A. Radomski, H. Fairbairn, S. Jolly*, S. Nagrath*. "Circulating tumor cells (CTCs) isolated from stage III NSCLC patients using microfluidic graphene oxide (GO) Chip predicts progression free survival." *In preparation*.

4. 3 Introduction

Approximately 190,000 people were diagnosed with non-small cell lung cancer (NSCLC) in 2020. While localized, NSCLC has a survival rate of 63% and while regional, the survival rate is 35%, however when the cancer becomes metastatic the survival rate drops to 7%.[1] The current treatment for stage III, NSCLC, the final stage before metastatic cancer, is combination chemotherapy and radiation (RT) followed by anti-PD-L1 (programmed death ligand 1) immunotherapy for one year.[2,5] Being able to predict which patients will metastasize as early as the first few weeks of the RT would allow those patients to receive highly personalized, precise clinical intervention. To achieve this level of precision medicine, it is critical to repeatedly profile a patient's tumor to have accurate, up-to-date information about the patient's ever-changing tumor. However, current clinical practices rely on imaging scans and needle biopsies, which are expensive, time consuming, invasive, and minimally repeatable. As such,

there is a need for inexpensive, quick, minimally invasive, and easily repeatable technologies to characterize a patient's tumor, allowing for maximally personalized, precise treatment decisions.

Researchers have proposed the liquid biopsy to fill this need. The liquid biopsy is an assay that characterizes a biomarker found in a simple blood draw with the goal of informing treatment decisions or predicting patient outcomes. Liquid biopsies can be done many times throughout a patient's treatment, allowing for longitudinal monitoring of that patient. Common biomarkers include circulating tumor DNA or RNA (ctDNA/RNA), extracellular vesicles (EVs), and circulating tumor cells (CTCs).[107,187] ctDNA is the most common clinically used biomarker and is used mainly in cancer diagnostics or when looking for minimal residual disease[188,189]. However, ctDNA suffers from fast clearance and degradation in the blood stream as a result of the other circulating blood components.[168,169] A second promising marker, EVs, are nanovesicles excreted from all cell types that contain molecular information from their cells of origin, including tumor cells.[19,21,65,190] EVs contain DNA, RNA, proteins, and other analytes allowing for multi-analyte tumor profiling, however tumor-derived EVs are found in a backdrop of non-specific EVs in the blood.[39,40,173,187,191,192] Since there are no technologies to reliably isolate specifically tumor derived EVs, their clinical use is still largely undetermined. Although these two biomarkers are promising, the challenges associated with their isolation and characterization make them less suitable for serial tumor profiling compared to CTCs.

CTCs, conversely, are tumor cells shed from a solid tumor that circulate in the blood and give researchers direct information about the tumor. In many cancers, including NSCLC, the quantity as well as contents of CTCs, such as protein expression, RNA and DNA profiles, can be correlated to progression-free survival, overall survival, and disease stage.[42–45,127] Although CTCs are powerful biomarkers, their low concentration in the blood, 10-100 CTCs/mL,

compared to a backdrop of 10^6 white blood cells are challenging. For CTCs to become clinically useful biomarkers, highly accurate isolation and characterization techniques are critical, with many technologies being developed each year.

CTCs express unique surface proteins compared to white blood cells, making immunoaffinity-based technologies promising for isolating CTCs. The most common of which is the FDA-approved CellSearch®, which uses antibodies against epithelial cell adhesion molecule (EPCAM) to capture CTCs with magnetic beads.[113,193] Lung cancer CTCs, however, have been shown to lack EPCAM expression[109,194], making CellSearch® an ineffective technology for isolating CTCs from NSCLC. To overcome this challenge, novel immunoaffinity-based methods have been developed to isolate CTCs using multi-antibody cocktails, allowing CTCs to be isolated based on several surface proteins instead of solely EPCAM.[122] One example is the graphene oxide microfluidic chip (GO Chip) that we developed to isolate CTCs with high purity and specificity.[195] The GO Chip is a microfluidic technology that uses antibodies against CTC surface proteins to immobilize them on functionalized gold nanoposts. The GO chip was optimized to isolate CTCs specifically from NSCLC patients using anti-EPCAM, anti-epidermal growth factor receptor (EGFR), and anti-CD133 to increase the capture of lung cancer CTCs.[118–120,122,196]

Previous studies have correlated CTCs and CTC metrics to timepoints during treatment, or loosely to clinical outcomes, however none have demonstrated the clinical utility of monitoring CTCs in stage III NSCLC patients.[177,193,197,198] In a cohort of stage I-III NSCLC patients, we used the GO chip to demonstrate that the percent of PD-L1+ CTCs increased after RT, raising from 0.7% of CTCs to 24% of CTCs in 1mL of blood.[199] Additionally, we used RT-qPCR to further profile the isolated CTCs and found that PD-L1 and LGALS3BP were

significantly upregulated in the CTCs of patients with worse progression. Dorsey et al. developed an adenoviral probe that monitors telomerase activity to detect CTCs from the blood both before and after RT. They tracked 10 stage III NSCLC patients and found that patients had a substantial decrease in CTCs from before RT to after RT, with an average dropping from 62.7 to 0.6 CTCs/mL.[200] This group followed up their initial study with a larger cohort including 48 patients and found that 75% of the 20 patients who had recurrence saw an increase in the CTC counts post-RT. While these studies demonstrate the potential utility of using CTCs to monitor NSCLC patients through treatment, they did not correlate CTC metrics to clinical outcomes such as progression free survival (PFS) time.

In the current study, we use the GO chip to profile CTCs from locally advanced (stage III) NSCLC patients across both RT and immunotherapy. We isolated the CTCs and performed molecular characterization to develop CTC signatures that predict which patients will have shorter PFS time. By identifying which patients will have poor response to radiation therapy, clinicians can adapt treatment regimens using alternative lines of therapy for these patients. The cohort for this study all received combination chemotherapy and RT for six weeks, with most of the patients then receiving durvalumab for 1 year following their RT. Blood was drawn at six timepoints across both treatments and profiled for CTCs, making this the first study that monitored patients across both RT and durvalumab.

For each blood sample, two GO chips were processed in parallel to isolate and characterize CTCs to develop these CTC signatures. Using the first GO chip, we determined the quantity of CTCs using immunofluorescent staining. The second GO chip was used for on-chip RNA extraction followed by transcriptome profiling using Affymetrix microarrays for gene expression analysis. The CTC metrics were then analyzed and correlated to clinical data such as

gross tumor volume (GTV) and PFS. We then determined CTC signatures that are predictive of shorter PFS time for stage III NSCLC patients. Here we identified a CTC signature that is present early in a patient's RT that is predictive of shorter PFS, thereby allowing enough time for clinical intervention.

4. 4 Methods

4.4.1 Patient Enrollment

Patients provided written consent and all blood was collected under IRB approval from the University of Michigan. All patients had either stage IIIA or stage IIIB non-small cell lung cancer and had no previous therapies.

4.4.2 Sample Collection

Blood was collected from patients into 5 mL EDTA tubes. Blood was stored on a rocker until use to ensure the blood did not separate. 2mL of the blood was processed on the GO chips, 1 mL per chip.

4.4.3 Graphene Oxide Chip Fabrication

The GO chip was fabricated following procedures described previously[118]. Briefly, the PDMS chamber and silicon substrate were prepared separately and bonded using corona discharge. The gold patterned silicon substrate was prepared in the University of Michigan's Lurie Nanofabrication Facility using standard photolithography to pattern the silicon wafer with 50,000 gold flowers. Specifically, the silicon wafers are first deposited with one layer of chrome and one layer of gold.

GO chip functionalization is then performed in a wet lab. GO suspension is premade with graphene oxide, N, N-dimethylformamide (DMF), Tetrabutylammonium (TBA) hydroxide, and

phospholipid-polyethylene–glycol-amine (PL-PEG-NH2). Silicon substrates are immersed in the GO suspension for 10 minutes, followed by the addition of cross-linker compound N-(gamma-maleimidobutyryloxy) succinimide (GMBS) and Neutravidin. The GO chip was stored at 4°C until use.

4.4.4 CTC isolation using GO Chips

Two GO chips per sample were removed from the 4C fridge, and a 1mL PBS wash was flowed at 100 µL/min to rinse off the Neutravidin. Antibody cocktails were prepared during the PBS wash: 1% bovine serum albumin (BSA) in PBS filtered through a 0.5 µm filter, anti-EPCAM, anti-CD133 (Miltneyi), and anti-EGFR (RayBiotech). Following PBS wash, antibody cocktail was flowed through the inlet of each device at 20 µL/min, the devices were then incubated for 30 minutes. The devices were turned, and antibody cocktail was flowed through the outlet of each device at 20 µL/min and incubated for another 30 minutes. Following the incubation, another PBS wash was performed, 1 mL PBS at 100 µL/min. 3% BSA in PBS filtered through 0.5 µm filter was then flowed, 1mL at 100 µL/min, to decrease non-specific binding. Before applying blood to the devices, the blood was pipetted several times to ensure complete mixing. 1mL of blood was flowed at 1mL/hr through the inlet of the device to isolate CTCs and the effluent from each device was collected. To remove red blood cells (RBC) and other blood components, 6mL of PBS was flowed at 100 µL/min.

4.4.5 On-chip CTC fixation

After CTC isolation, one of the devices had PFA flowed, 1mL at 100 µL/min with a 40 min incubation, to fix the CTCs for future enumeration. Following PFA, 1mL PBS was flowed at 100 µL/min to wash extra PFA. The inlet and outlet of the chip was then parafilmed and the device was stored in a parafilmed dish with a wet kimwipe in a 4C fridge to avoid drying.

4.4.6 Immunofluorescent Staining of GO Chips

Immunofluorescent staining was performed on the GO chips that were fixed with PFA and stored at 4℃. The GO chips were removed from the fridge and allowed to heat to room temperature on the bench. To permeabilize the cells, we flowed 1mL of 0.02% TritonX at 100µL/min and incubated for 30 minutes. PBS was then washed through the device, 1 mL at 100µL/min. The devices were blocked at 100µL/min and incubated for 40 minutes using a cocktail of blocking solutions: 200µL goat serum, 300µL 6% BSA in PBS, and 500µL PBS per device. Primary antibody cocktail was applied immediately after blocking and flowed at 50µL/min. The devices were incubated overnight at 4℃. The following day, primary antibodies were washed off using 2mL of PBS flowed at 100µL/min. Secondary antibody cocktail was then applied at 50µL/min and incubated for 1 hr at room temperature. The unbound secondary antibody cocktail was then washed off with 2mL PBS at 100µL/min. DAPI was then applied to the devices at a concentration of 1µL in 1 mL. A final PBS wash was performed to remove excess DAPI, 2 mL PBS at 100µL/min. The inlets and outlets of the device were covered with parafilm and stored before imaging.

Table 4-1 Antibodies used for Immunofluorescent Staining

	Primary Antibodies		Secondary Antibodies	
Channel	Name	Company	Name	Company
FITC	CD45	Bio-Rad Cat# MCA87GA	AlexaFluor 488, goat anti-mouse IgG2A	Thermo Fisher Cat# A21131
CY3	Pan-CK	Bio-Rad Cat# MCA1907	AlexaFluor 546 goat anti-mouse IgG1	Thermo Fisher Cat# A21123
CY5	PD-L1	Biolegend Cat# NC0043617	AlexaFluor 647 goat anti-mouse IgG2b	Thermo Fisher Cat# A21242

4.4.7 GO Chip Imaging and CTC enumeration using Fluorescent Microscopy

The GO chips were scanned on an inverted Ti2 Eclipse fluorescent microscope with an LED light source. Each chip was scanned at 30x, using a 20x objective and an added 1.5x on the microscope. The chips were scanned in 4 channels with the following exposures and intensity percentages: DAPI (100ms, 15%), FITC (200ms, 30%), CY3 (200ms, 30%), and CY5 (200ms, 30%). After scanning, the images are opened in the Nikon NIS Analysis software to count for CTCs. CTCs are counted as being DAPI+/PanCK+/CD45- cells. A subset of PD-L1+CTCs is counted as being DAPI+/PanCK+/CD45-/PD-L1+ cells.

4.4.8 On-chip RNA extraction

The second GO chip was used for RNA extraction. Following CTC isolation, 100 µL of PicoPure RNA Extraction Buffer was flowed into the chip. The chip was then incubated at 42C for 30 minutes. Following incubation, 100 µL of UltraPure DEPC-treated water was flowed through the device and was collected in a sterile Eppendorf. This second RNA sample contains the RNA extracted from the CTCs. Each sample was frozen at -80C until purification.

4.4.9 CTC RNA Purification off-chip

After on-chip RNA extraction, the RNA was frozen at -80℃. To purify, the samples were thawed on ice before purification using the Arcturus® PicoPure® RNA Isolation Kit (Thermo Fisher, Cat# KIT0204). Purified RNA was stored in the -80℃ freezer until processing.

4.4.10 Affymetrix Clariom S PICO microarray processing

After thawing gently on ice, 11µL of the RNA samples were plated into a sterile barcoded PCR plate supplied by Thermo Fisher. The samples were then shipped to Fisher

scientific for microarray services by their lab. Briefly, RNA was quantified using PCR before running on Clariom S PICO human microarrays. Data was then returned to our lab for analysis.

4.4.11 Analysis of RNA microarray data

Standard microarray data processing procedures were followed in R programming environment (4.0.2). Briefly, raw intensities were imported as CEL files using the oligo package. The intensities were then normalized and summarized into gene-wise expression values using a robust multichip average (RMA) method.[201] Quality control plots, including normalized unscaled standard error (NUSE), relative log expression (RLE) as well as principle component analysis (PCA) were generated to discover outliers in the dataset. The probesets were then annotated using clariomshumanhttranscriptcluster.db package. If multiple probes were mapped to the same gene, the one with highest average expression across all samples was selected. Differentially expressed genes were then calculated between different conditions using the limma package. A paired-sample design was used for the comparisons between different time points and treatment outcomes.

4.4.12 Statistical Analyses of Clinical Data

Comparisons between two groups, such as “Stable” and “Future Progression” were performed using unpaired Student’s t-tests, two-tailed. Comparisons between timepoints were performed using a paired Student’s t-test, two-tailed. Correlation was performed by making a Pearson’s correlation matrix, and reported values are Pearson’s r. Survival analysis was performed using Kaplan-Meier survival curves using the Logrank method (Mantel-Cox test). Receiver operator characteristic (ROC) curves were generated using a 95% confidence interval using the Wilson/Brown method. All analysis was conducted in GraphPad Prism V9.

4. 5 Results

4.5.1 CTC isolation using graphene oxide (GO) Chip in stage III NSCLC patients

From whole blood, we isolated CTCs using the previously developed graphene oxide based microfluidic GO chip for CTC enumeration and mRNA characterization, **Figure 4-1.** In brief, the GO chip consists of a silicon wafer patterned with 50,000 gold flowers, graphene oxide nanosheets are adsorbed onto the surface, and a PDMS chamber is covalently bonded form a single chamber.[121] The device is then functionalized to tether the following capture antibodies on the surface: anti-EpCAM, anti-EGFR, and anti-CD133.[119] EpCAM is an epithelial marker commonly expressed on CTCs, EGFR is a protein expressed in lung cancer, and CD133 is a stem-cell like marker that has been shown to cause high propensity for tumorigenic phenotypes in lung cancer.[202] Two GO chips were run in parallel for each patient blood sample, one for CTC enumeration and one for RNA extraction of captured CTCs, **Figure 4-1**. These data were then

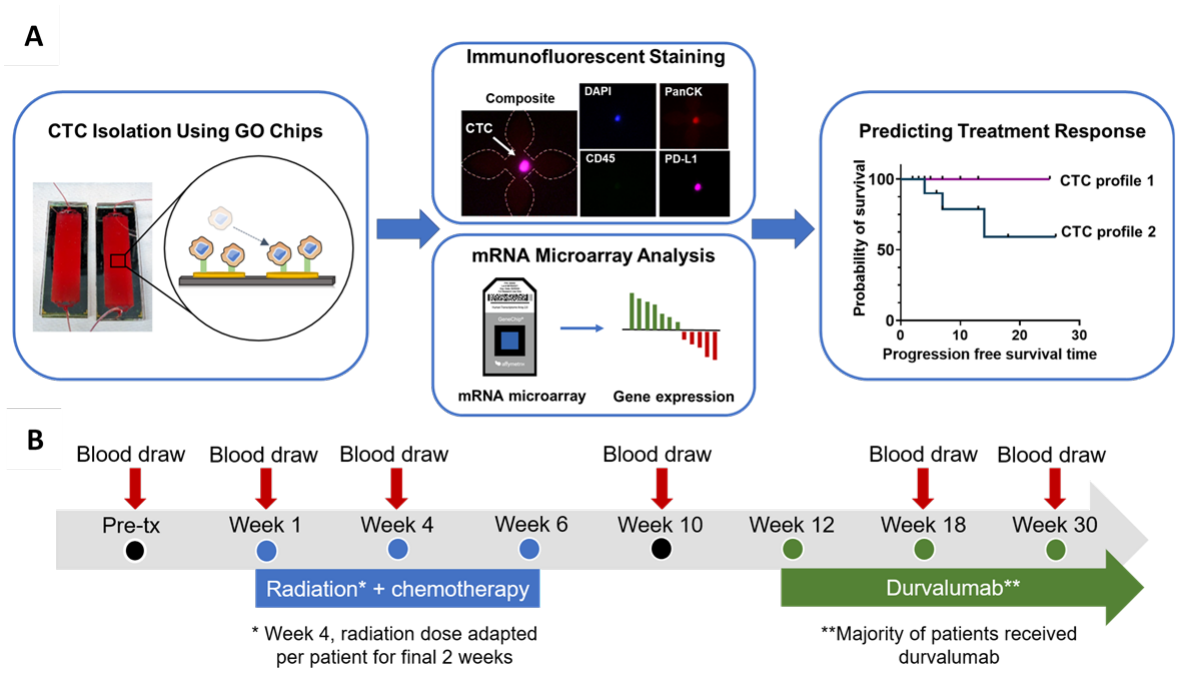

Figure 4-1 Overview of CTC isolation and characterization summary.

A. Schematic of CTC isolation using microfluidic GO Chip. Each sample is processed on two devices, one for enumeration via immunofluorescent staining and the second for mRNA microarray analysis. The CTC characteristics are then used generate profiles that are predictive of progression free survival. **B.** The timeline of patient sample draws shown, the black timepoints indicate no treatment, the blue time points are during radiation therapy, and green time points are during durvalumab for the majority of patients. Some patients received no future therapy after radiation, and some received a different immunotherapy.

compared to clinical metrics to generate CTC profiles that were assessed for their ability to predict poor patient outcomes.

CTCs were enumerated on the first GO chip using on-chip immunofluorescent staining. Staining was performed using a previously published protocol.[119] We stained the devices for four markers of interest: DAPI, a nuclear dye; pan-cytokeratin (panCK), a CTC marker; CD45, a leucocyte marker; and programmed death ligand-1 (PD-L1). Following immunofluorescent staining, the GO chips were imaged using an inverted fluorescent microscope, and CTCs were counted based on the presence of these stained proteins. A CTC was counted as a CK+/CD45-

/DAPI+ cell, with a subpopulation of CTCs being PD-L1+ CTC counted as panCK+/CD45-/DAPI+/PD-L1+ cells, **Fig 4-1A.**

In this cohort, patients were profiled through both radiation therapy (RT) and immunotherapy at a total of six timepoints, **Figure 4-1B**. Patients undergo six weeks of concurrent chemotherapy and RT; for the first four weeks, patients receive the same radiation dose, however, the dose for the final two weeks is determined based on the patient's imaging scans at week 4 of RT. Following radiation, most patients (16/26) had 1 month of no treatment before starting an anti-PD-L1 immunotherapy, durvalumab. Some patients, however, were enrolled before durvalumab became standard of care. Of these, 2 patients received a different immunotherapy, 8 patients received no immunotherapy, and 1 died during radiation. Full clinical information and demographics is found in **Table 4-2**.

CTCs were monitored at six strategic timepoints through both RT and immunotherapy. The first timepoint, Pre-TX, occurred before patients received any treatment and serves as a baseline. The Week 1 (W1) time point is during the first week of RT, and potentially a timepoint that could offer a very early indication of patients' disease. Week 4 (W4) is the fourth week of RT and the timepoint when the clinical team altered patients' radiation dosing. This timepoint offers an optimal time to adjust patient treatment. The Week 10 (W10) timepoint is one month after patients finish chemotherapy and RT but before they receive durvalumab. This timepoint is used as the end point for radiation efficacy. The Week 18 (W18) timepoint is approximately 1 month into the patients' immunotherapy, while the Week 30 (W30) timepoint is approximately 4 months into immunotherapy. The timeline of blood draws with a treatment timeline is in **Figure 4-1B.**

Table 4-2 Patient demographic data

Clinical Characteristic		n (%)
Total Patients	26	—
Age	mean = 67	range = 50-83
Sex	F	7 (24%)
	M	21 (76%)
Stage	IIIA	11 (38%)
	IIIB	18 (62%)
Histology	Adenocarcinmoa	12 (46%)
	Squamous cell	12 (46%)
	Poorly differenciated NSCLC	2 (8%)
Immunotherapy following chemoradiation	None	8 (30%)
	Durvalumab	16 (62%)
	Pembrolizumab	1 (3%)
	Atezolizum	1 (3%)
Progression	None	17 (65%)
	Locoregional	5 (19%)
	Distant	4 (15%)
Current Status	Stable	19 (73%)
	Progressing	3 (12%)
	Deceased	4 (15%)

4.5.2 Absolute CTC number decreases through treatment but does not correlate to patient outcome

The number of CTCs in 1 mL of blood was enumerated for each patient, revealing unique trends in CTC counts. As seen in **Figure 2A**, the patients have different trajectories, however,

several overall trends became apparent. For reference, each horizontal line indicates the trajectory of one patient, with each mountain peak height representing the CTC concentration per mL of blood. Any blank spaces or discontinuous lines indicates that the patient missed the blood draw at that timepoint. As the patients were plotted based on their CTC counts at Pre-TX, the mountain plot indicates that most patients have a substantial decrease in CTCs from Pre-TX to Week 1 of radiation. While many patients sustain the low number of CTCs through the end of RT, several patients had comparatively high numbers of CTCs at W10 after RT, **Figure 4-2A.** Instead looking at the CTC counts averaged by timepoint, we see that there was a significant decrease in CTCs from Pre-TX to Week 1 ($p = 0.02$, paired t-test), and from Pre-TX to both Week 10 and Week 30 ($p = 0.04$ and 0.02 respectively, paired t-test), **Figure 4-2B**. This result further solidifies that CTCs decrease at the start of RT; however, this additionally elucidates that CTCs are lower after RT and several months into immunotherapy at Week 30.

After demonstrating a significant change in CTCs based on timepoint, we investigated whether CTC concentration at the timepoints around RT correlated to gross tumor volumes (GTVs) measured before and during RT. The number of CTCs were correlated to GTV using Pearson's correlation matrix, and values reported are Pearson's r, with significant correlations having $p<0.05$ **Figure 4-2C**. This analysis reveals whether two values are correlated by comparing the values' rank within all the values, i.e. if variable 1 is consistently high when variable 2 is high amongst their populations, the two variables are correlated. As expected, the Pre-TX and W4 GTVs were strongly correlated ($p = 0.0076$, Pearson's correlation t-test). Interestingly, the number of CTCs does not correlate to GTV at any of the time points, with some timepoints being even slightly negatively correlated with GTV, such as W4 and W10.

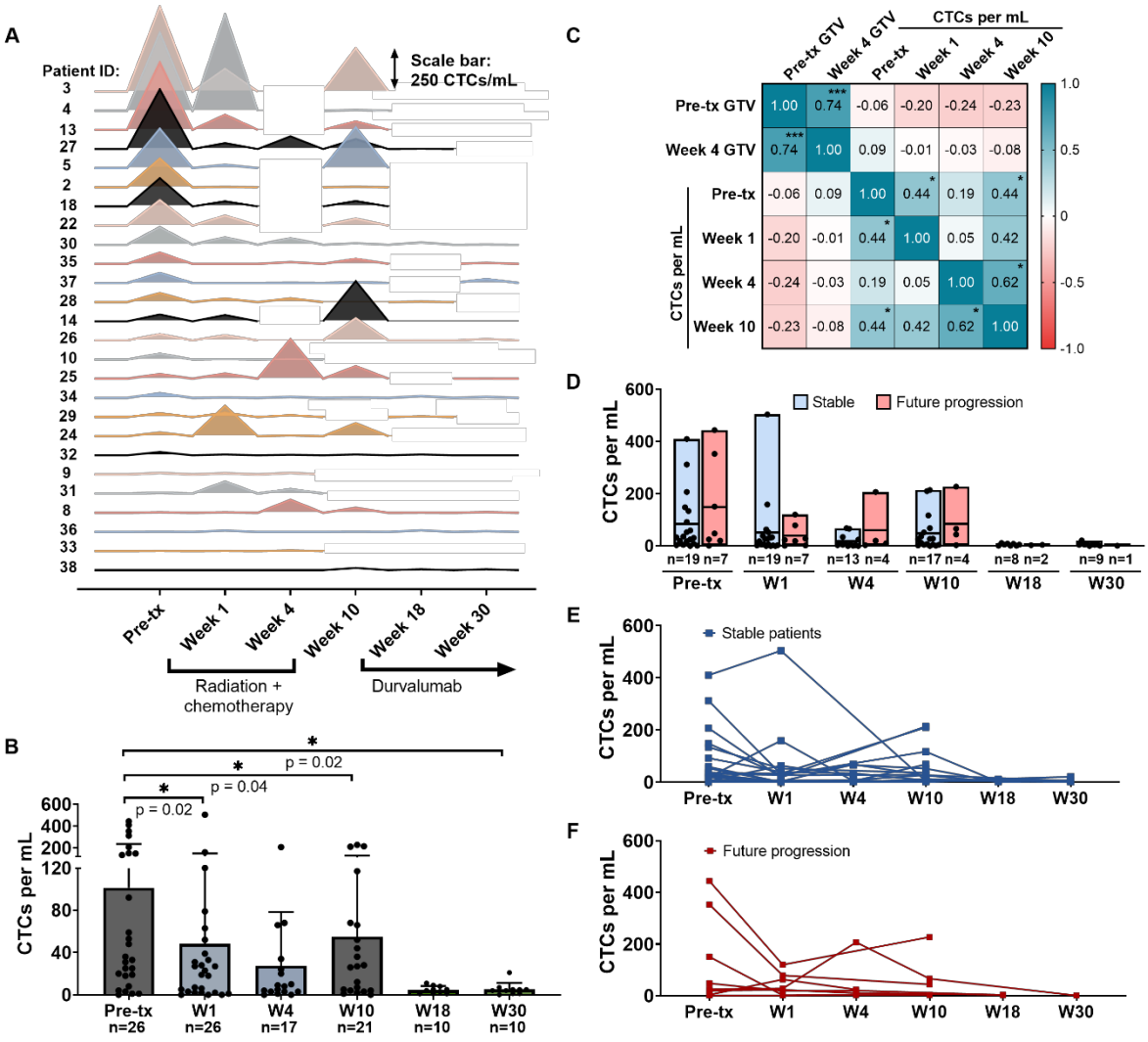

Figure 4-2 CTC isolation and enumeration using graphene oxide (GO) chip

A. Ridge plot demonstrating the CTCs per mL of blood at each time point for each patient. Horizontal lines denote one patient, with each mountain peak representing the number of CTCs at that timepoint per mL. Patients are arranged from highest Pre-tx CTCs to lowest. Scale bar reads the height of a 500 CTC/mL peak. **B.** Bar plot of CTCs per mL at each time point for all patients grouped. Statistics performed using two-tailed, paired t-test (* denotes p-val < 0.05). **C.** Correlation matrix with Pearson's r shown in each square demonstrating the correlation between the GTV (gross tumor volume) at two time points, Pre-tx (pre-treatment) and at week 4 of radiation, along with the CTC numbers at four timepoints (* denotes p-val < 0.05, ** p-val < 0.005, *** p-val < 0.0005). **D.** CTCs per mL of blood plotted based on whether the patient has stable disease or ultimately progressed. **E-F.** Trajectories of the number of CTCs/mL through all six timepoints as split into **E.** stable and **F.** patients with future progression.

This analysis also revealed that the number of CTCs is loosely correlated between some of the

time points, but not all, **Figure 4-2C**. For instance, the number of CTCs at Pre-TX is correlated to the number at W1 and W10 but not W4. However, the number of CTCs at W4 does correlate to the number at W10. Numerous studies have found that CTC number and GTV do not correlate in various cancers, including squamous cell carcinoma of the head and neck region, hepatocellular carcinoma, and small cell lung cancer.[203–205] This could be for multiple reasons, including the variation in vasculature around and within a tumor which could change the rate of dissemination of CTCs found into the blood.[206]

The absolute number of CTCs at each timepoint was then compared to disease progression; patients were grouped into either "Stable" and "Future progression" based off their clinical outcomes. The number of CTCs at each timepoint where then plotted for the two groups, **Figure 4-2D,** and was found to not differ significantly between the stable and progressing patients. The individual CTC trajectories of the stable, **Figure 4-2E,** and progressing, **Figure 4-2F**, patients were plotted and further demonstrate that there is no difference in the number of CTCs between the stable and progressing patients.

4.5.3 Large decrease in CTCs during RT predicts longer progression free survival time

When doing an interpatient comparison, the heterogeneity between patients and tumors is likely the most important factor in CTC dissemination.[206] Instead, a comparison within each patient is a more reasonable strategy, comparing the number of CTCs longitudinally within one patient to determine how their individual disease in changing, **Figure 4-3A**. We quantified this

as the percent change in CTCs, giving us a standardized change in CTCs that can then be compared between patients.

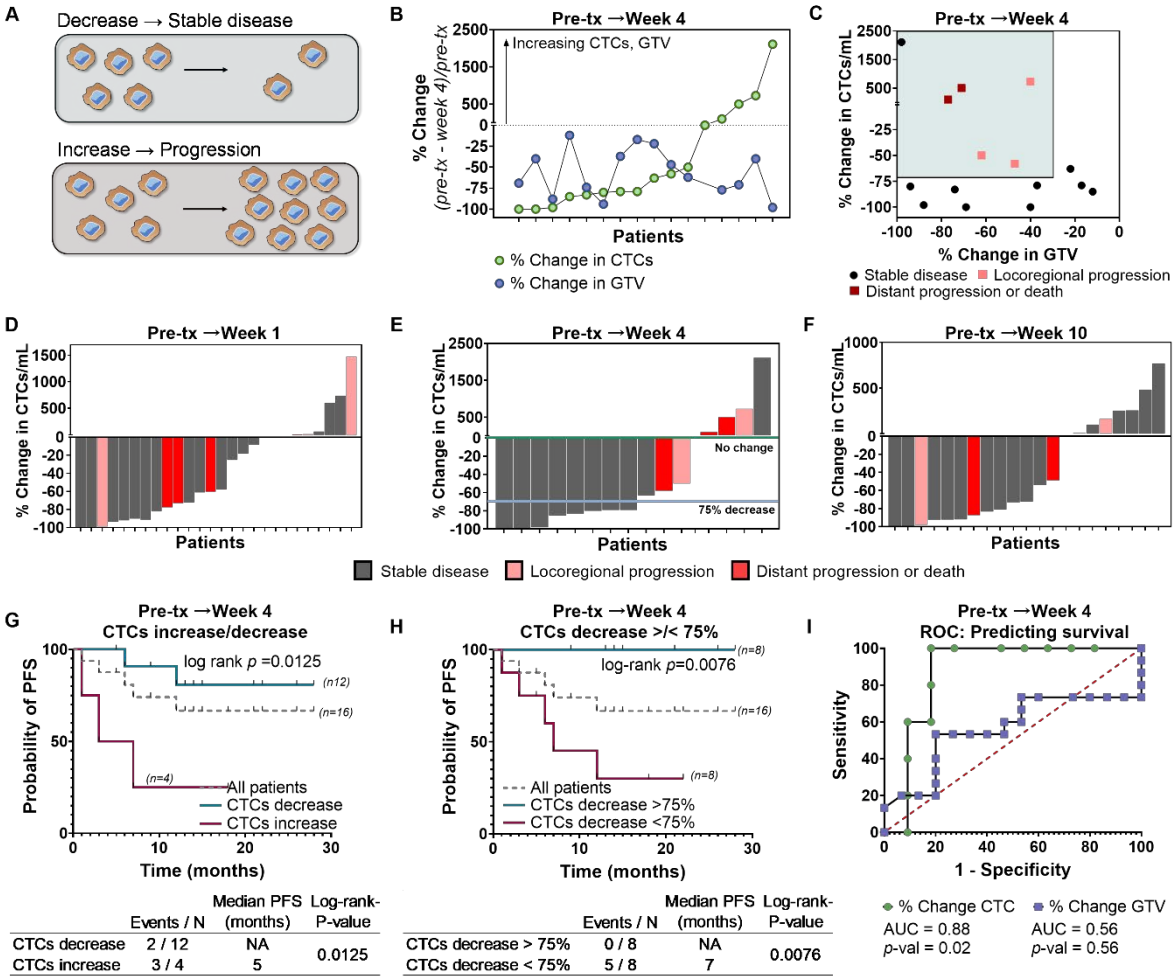

	Events / N	Median PFS (months)	Log-rank-P-value
CTCs decrease	2 / 12	NA	0.0125
CTCs increase	3 / 4	5	

	Events / N	Median PFS (months)	Log-rank-P-value
CTCs decrease > 75%	0 / 8	NA	0.0076
CTCs decrease < 75%	5 / 8	7	

Figure 4-3 Change in CTCs during radiation treatment predicts progression free survival.

A. Schematic demonstrating the hypothesis of change in CTCs within one patient. **B.** Percent change in GTV and CTCs between Pre-TX and Week 4 for 16 patients plotted by patient. **C.** Percent change in CTCs plotted against percent change in GTV. Color and symbol shape denote whether the patient has stable disease, locoregional progression, or distant progression or death. Lines indicate a quadrant where patients found within the quadrant almost all have progression, 5/6 patients. **D-F.** Percent change in CTCs by patient with each patient labeled by disease status for **D.** Pre-TX to Week 1, **E.** Pre-TX to Week 4, and **F.** Pre-TX to Week 10 timepoints. **G-H.** Kaplan Meier curves demonstrating the difference in progression free survival (PFS) between patient groups determined by the percent change in CTCs between Pre-TX and Week 4 for two different cutoffs **G.** increasing or decreasing CTCs and **H.** CTCs decreasing by more or less than 75%. **I.** Receiver operator curve for both the percent change in CTCs and GTV between Pre-TX and Week 4. All p-val are two-tailed.

$$\% \, change = \frac{(CTCs \; at \; time \; 1 - CTCs \; at \; time \; 2)}{CTCs \; at \; time \; 1}$$

First, percent change was calculated for GTV and CTCs between Pre-TX and W4, the two timepoints when patients had both tumor imaging scans and CTC enumeration. We found that all the patients had the expected decrease in GTV, while not all patients had a decrease in CTCs, **Figure 4-3B.** One patient had no change in CTCs while 4 patients had an increase in CTCs. The quantity of change does not correlate, however, with some patients having a large decrease in GTV with a minimal decrease in CTCs and the opposite. This analysis does reveal that there are three groups of patients as defined by their percent change in CTCs from Pre-TX to W4: high % decrease, moderate % decrease, and increase.

Percent change in CTCs was correlated to percent change in GTV and each patient was labelled by their clinical status, either (1) stable, (2) locoregional progression, or (3) distant progression, **Figure 4-3C**. All 5 patients who had future progression had an increase in CTCs between timepoints. Interestingly, the percent change in GTV for the progressing patients is widely spread, ranging from 40-80%. This indicates that it is the percent change in CTCs and not GTV that corresponds to the future progression of these patients.

The percent change in CTCs between Pre-TX and W1, **Figure 4-3D**, Pre-TX and W4, **Figure 4-3E**, and Pre-TX and W10, **Figure 4-3F,** were plotted. The percent change in CTCs was plotted for each patient, and each patient was labelled according to the same metrics of progression: stable, locoregional, and distant progression. As shown in **Figure 4-3D, F**, the patients who have future progression were indistinguishable from stable patients at Pre-TX and W10 timepoints. Alternatively, patients who have future progression have a higher percent change in CTCs between Pre-TV and W4, **Figure 4-3C**, indicating that a higher percent change in CTCs between Pre-TV and W4 may be a predictor of future progression.

To perform survival analysis, the patients were first divided based on increasing (n=4) or decreasing (n=16) CTCs between Pre-TX and W4, **Figure 4-3G**. There was a significant difference between the two populations, with the patients who had an increase in CTCs having a PFS time of only 5 months (p=0.0125, log-rank (Mantel-Cox) test). Conversely, among the patients who had a decrease in CTCs, only two of the patients had future progression, most of the data points were censored. The monitoring time was an average of 17 months for the patients with a decrease in CTCs.

A second cutoff, a decrease in CTCs of more (n=8) or less (n=8) than 75%, divided the patients into two even groups. This cutoff shows that patients who had less than a 75% decrease in CTCs had a significantly shorter PFS time of 7 months (p=0.0056, log-rank (Mantel-Cox) test). Among the patients who had a decrease of more than 75%, none of the patients had future progression, so all the data points were censored. The average monitoring time was 21 months. This data strongly indicates that having more CTCs at W4 compared to Pre-TX is an early indicator of future progression.

Finally, receiver operator characteristic curves (ROC) were used to determine which of the two potential predictors of future progression is more accurate between percent change in GTV and CTCs between Pre-TX and W4. ROC curves are used to illustrate the diagnostic or prognostic potential based on a binary outcome. This analysis assesses with what accuracy a new patient who is added to the cohort would be correctly predicted to be stable or progressing based on the specified criteria. Using percent change in GTV to predict future progression led to an area under the curve (AUC) of 0.55, meaning a patient would be correctly predicted to be stable or progressing 55% of the time. Conversely, using percent change in CTCs led to an AUC of 0.88 (p=0.02, AUC), or an 88% chance of correctly classifying a patient.

4.5.4 High percentage of CTCs with programmed death ligand 1 (PD-L1) expression indicates higher chance of future progression

Following RT, many of the patients received the immunotherapy durvalumab, an anti-PD-L1 antibody. We investigated whether the presence of PD-L1 on CTCs was predictive of patient outcome for patients receiving durvalumab. Because durvalumab targets PD-L1 expressed on cancer cells, we hypothesize that having a higher number of PD-L1+ CTCs would be predictive of increased durvalumab efficacy. First, we investigated the presence of PD-L1+ CTCs at each time point, **Figure 4-4A.** Among all the patients, there was a significant decrease in PD-L1+ CTCs from Pre-TX to W1 of RT ($p=0.02$, paired two-tailed t-test), something that has been previously reported.[199] The number of PD-L1+ CTCs was on average dramatically lower at the later timepoints (W18, W30). However, many of the patients who had these final two blood draws coincidentally had very low CTCs at most timepoints, so this finding should be interpreted with caution.

To remove the bias of having varying numbers of total CTCs, the percent of PD-L1+ CTCs was plotted for all patients, **Figure 4-4B**, demonstrating that the percent of PD-L1+ CTCs had a large spread among all patients at all timepoints. To assess the relationship between PD-L1 expression on CTCs and patient outcomes on durvalumab, the analysis was further restricted to only the patients who received durvalumab (n=16), **Figure 4-4C.** As before, the percent of PD-L1+ CTCs at each timepoint was plotted, and the range was still widespread. However, by adding a second variable to the analysis, the three patients who had progression while on durvalumab were labelled in red. It is apparent that these three patients always appear in the upper half of patients at all timepoints for percent of PD-L1+ CTCs. This finding corroborates a

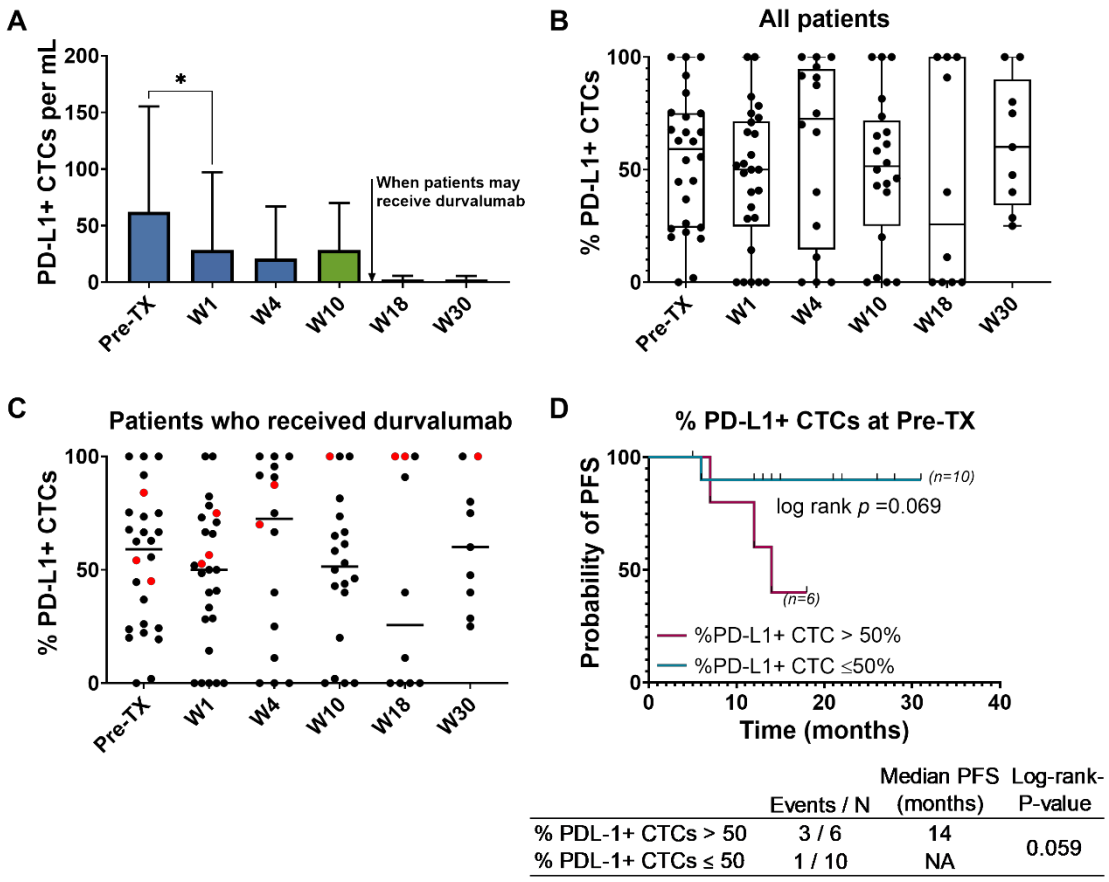

	Events / N	Median PFS (months)	Log-rank-P-value
% PDL-1+ CTCs > 50	3 / 6	14	0.059
% PDL-1+ CTCs ≤ 50	1 / 10	NA	

Figure 4-4 PD-L1 expression on CTCs indicates metastatic potential.

A. Number of PD-L1+ CTCs per mL at each timepoint. **B.** Percent of CTCs that are PD-L1+ at each timepoint. **C.** Percent of CTCs that are PD-L1+ for only the patients who received durvalumab immunotherapy. **D.** Survival analysis for patients who received durvalumab with a cut off of 50% PD-L1+ CTCs.

previous finding that an increase in PD-L1+ CTCs has the potential to act as a marker of resistance to PD-1/PD-L1 inhibitors.[207]

To round out this analysis, survival analysis was performed based on the percent of PD-L1+ CTCs at each time point for patients who had durvalumab, and the most predictive timepoint was Pre-TX. The patients were split by > or < than 50% of CTCs being PD-L1+, and the group that had >50% PD-L1+ CTCs had a shorter PFS time, 14 months compared to 21 months censored (p=0.069, log-rank (Mantel-Cox) test, survival analysis) **Figure 4-4D**. As such,

our finding conflicts with our previous hypothesis, and now see that a higher expression of PD-L1 may be an indicator of poor outcomes on durvalumab.

4.5.5 Differential gene expression analysis using Affymetrix microarrays shows aggressive CTC phenotype

Common methods for high-throughput RNA analysis include PCR panels, RNA-seq, and single-cell sequencing. However, when analyzing CTCs, it is incredibly challenging to achieve adequately high RNA concentration and quality to use these methods. Microarrays, conversely, were originally designed for FFPE samples, which are notoriously challenging to characterize because of their low RNA quality. Additionally, recent advancements have decreased the necessary microarray input to 100pg of RNA, or as few as 10 cells. As such, microarrays offer the optimal combination of needing a low RNA input while still quantifying gene-level expression from >20,000 genes, making them an ideal method for CTC characterization.

Here, we isolated RNA on-chip using the Arcturus PicoPure kit, followed by off-chip purification, and microarray analysis using Affymetrix's Clariom S PICO chips processed by Fisher Scientific. We then developed and used an analysis workflow in R based off common microarray analysis methods using the packages oligo and limma.[208] For the microarray analysis, we used the Pre-TX, W4, and W10 timepoints based on the previous CTC and PD-L1 analyses, and a total of 59 patient CTC samples were processed. This microarray analysis represents a much more thorough RNA profiling than that used in previous GO Chip studies, RT-qPCR using the Fluidigm Biomark.[122,199]

Two main quality control analyses were performed, the normalized unscaled standard error (NUSE) and relative log expression (RLE) before normalization using rma. The NUSE is used to identify samples that have an error outside the range of the rest of the samples and should be centered around 1.0 for all samples. Here, we see that the NUSE has a decent amount of variability, with four samples having a higher NUSE than other samples, **Figure 4-5A**. Typically, we want to remove samples with high errors, however in this type of longitudinal analysis, removing one sample would require us to remove an entire patient from the analysis. As such, we will leave all samples after this analysis. The second analysis, RLE, instead assess how far from 0 the differences in expression level are across each microarray. The RLE shows that the samples are relatively consistent in their expression, and that no samples are distinct

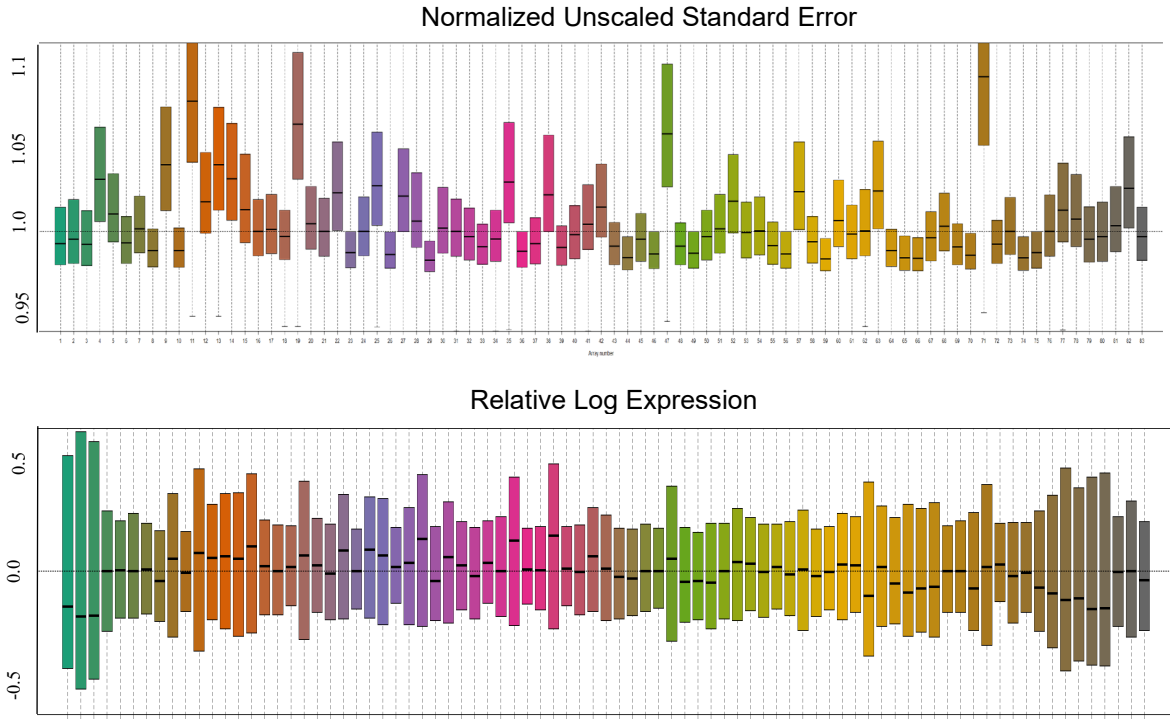

Figure 4-5. Quality control data for Affymetrix microarray samples.

Top. Normalized Unscaled Standard Error (NUSE) plot for the 83 samples included in this analysis, including cell lines and healthy controls. **Bottom.** Relative log error (RLE) for the samples.

outliers. Additionally, principal component analysis (PCA) was performed, although there were no obvious groupings based on timepoint, patient, or progression.

Following QC, the data was normalized, and differentially expressed gene analysis (DEG) was performed. Two types of DEG analyses were used: non-paired and paired. Non-paired analyses group the samples by timepoint, regardless of whether the patient had multiple samples in the progression. The paired analyses consider the patient ID and performs moderated paired t-tests. The number of samples included in each of the two analyses can be found in **Table 4-3.**

Table 4-3 Summary of samples in microarray analysis

Timepoint	Number of samples in non-paired analysis
Pre-TX	23
W4	14
W10	22
Multiple timepoints	**Number of patients included in paired analysis**
Pre-TX & W4	14
Pre-TX & W10	20

Using the two analysis methods, it was found that there were no differentially expressed genes (DEGs) between either Pre-TX or W4 and W10. There were, however, many DEGs between Pre-TX using the eBayes function, empirical Bayesian function, which uses either an input of a paired or unpaired t-test to determine significant genes. Genes were considered differentially expressed if they had a $p < 0.05$ and a false discovery rate (FDR) < 0.05 using the eBayes method. All p-values are reported as adjusted p-val, adjusted using an FDR cutoff of < 0.05. It was found that there are 304 significantly upregulated DEGs, shown in **Table 4-4.** While continued and deeper analysis is still needed, several genes on the list are of particular interest based on their previously shown implications in cancer.

Table 4-4 Upregulated genes between Pre-TX and W4 CTCs

Upregulated Genes: 304, adj P-val < 0.05

F5	DSC2	C19orf38	SNX3	OSTF1	TRIM24
IL4R	METTL9	CACYBP	NLRP12	TMBIM4	SHOC2
ORM1	BASP1	WDR41	DNTTIP1	AGTPBP1	MTF1
APMAP	AGO4	FOLR3	RAB10	NAGK	TIMP1
RGL4	RBP7	HSDL2	CHCHD7	CSF2RA	MYL12A
FAM200B	SMAD4	UBE2J1	SSR2	RBPJ	CDK19
NQO2	FAM157A	FAM157B	CERT1	RAB8B	TMEM167A
S100A12	PGLYRP1	GPCPD1	AQP9	CDC42	DDAH2
CDA	FPR2	CD14	GMFG	SIRPA	E2F3
ALPL	ZFP36L1	CR1	ATP5MPL	H3-3B	TBL1XR1
GDE1	S100A4	CTSH	IL1RN	NFE2	MCTP1
MMP9	CA4	UBLCP1	CEACAM1	FCGR2A	PJA2
CDC42EP3	MICU1	FCGR3A	APBB1IP	KCNE3	SPCS2
RAB27A	WASHC3	ITGB2	LRRC25	PPT1	IFNAR2
EIF4E3	ACSL1	RSL1D1	MMP8	SNAP23	RPS27L
MCEMP1	ZDHHC20	OSBPL8	MYD88	TTC17	SH3KBP1
S100A6	MAPK14	EPB41L3	TALDO1	HSD17B11	STEAP4
HMGB2	PADI4	IL17RA	EFHD2	PYCARD	RAB5IF
QPCT	ZNF438	SHKBP1	RNF24	ZYX	KREMEN1
GBA	DNMT3A	FPR1	PCNX1	GSR	H3C10
TSPO	TXNL1	JPT1	LILRB3	PHF21A	ST20
LAMTOR5	CREB5	STK38	RNF130	UBXN2B	AGTRAP
PLBD1	GABARAPL2	NCOA6	STX10	UHRF1BP1L	RBM22
PGK1	PGAM1	HK3	TBC1D1	HSD11B2	HCK
GAPDH	BLOC1S1	KMT2B	MON1B	RTF1	LMAN2
PXK	TLR1	PLSCR1	TXNDC17	SULT1B1	NDUFB6
S100A9	GCA	RNF123	VCAN	MANSC1	VASP
TXN	NMI	DNAJC25-GNG10	FCGR1A	DDX59	LPXN
DYSF	TES	DHRS7	PSMD9	CIDEB	ACP1
ANXA3	CTSD	SAMSN1	SRGN	PFKFB3	ADGRE2
PYGL	VAPA	RNF141	SCPEP1	PHF12	IFITM1
CYB5R4	MS4A6A	PFN1	BST1	NGLY1	GRB2
CST7	S100P	VNN1	MYL6	MGAM	TRIM8
MTARC1	CYBA	CDKN1B	POMP	LITAF	SRP14
PLP2	VEZF1	TYROBP	ZSWIM6	LRP10	CHTOP
RAC2	ARPC5	FCGR3B	ARHGDIB	RAD23B	ORMDL2
PROK2	PRAMEF10	MARK2	C1D	HTATIP2	ROCK1
ANPEP	NDUFA2	JAML	ABHD12B	ARHGAP15	H2AZ1
ANKRD13D	GNAI2	ALOX5	CKLF	MDH1	CD53
ETS2	RNF10	ADM	TNFAIP6	GNG5	UBL5
KCNJ15	CD58	PLAC8	SLC2A3	ENO1	VPS18
H3C11	NCF4	CLEC4D	LGALS1	CEACAM5	NUAK2
CNIH4	STAT5B	NOP10	SDCBP	CR1L	GTPBP1
CAMP	DEGS1	STXBP5	DR1	IL18RAP	SF3B1
EIF4B	ARPC2	RARA	ARPC1B	S100A10	LYST
VNN2	COPE	DYNLT1	FCER1G	ZFP91-CNTF	ASB7
IFNGR2	RTN3	LTB	SELL	CMTM2	RAB32
ZBTB7B	MSRA	ERO1A	CCDC28A	UBQLN2	LTA4H
PRR13	CFL1	EMB	IFITM2	PPP1CA	NFIL3
NAIP	MIEN1	HEBP2	PELATON	RASGRP4	
S100A11	ATG3	INSIG2	GLT1D1	OTUB1	

Table 4-5 Select DEGs between Pre-TX and W4 with function

Gene	Cancer type	Finding	Refs
STAT5B	Prostate, pancreatic, breast	• Proliferation, differentiation survival, migration, metastasis • Function and development of Tregs • Activated STAT5 is associated with suppression in antitumor immunity and proliferation, invasion, and survival of tumor cells	209–212
ANXA3	Lung adenocarcinoma	• Overexpression found to be significantly associated with metastasis, decreased overall survival, advanced clinical stage	213
S100A6	Gastric, colorectal, pancreatic, HCC	• Promotes cell proliferation and invasion	214–216
S100A12	Papillary thyroid cancer, gastric cancers	• Silencing inhibited cell proliferation, migration, invasion	217,218
RAB27A	NSCLC, renal cell carcinoma	• Regulates tumor microenvironment and promote tumor growth, poor survival • Resistance to chemotherapies	219–221
RAB10	HCC	• Promotes cell survival, proliferation, poor prognosis • Dysregulated RAB mediated vesicle delivery can lead to tumorigenesis	219,222,223

Select genes were chosen because of their functions in cell proliferation, migration, metastasis, and survival of tumor cells, **Table 4-5**. The selected genes were found to be upregulated in CTCs at W4 and represent a CTC phenotype that is more invasive or aggressive compared to those of the Pre-TX. As shown in **Figure 4-6,** the above listed genes, STAT5B, S100A6, S100A12, ANAXA3, RAB27A, and RAB10 are all significantly upregulated in CTCs between Pre-TX and W4 as quantified using the eBayes method in limma, FDR < 0.05.

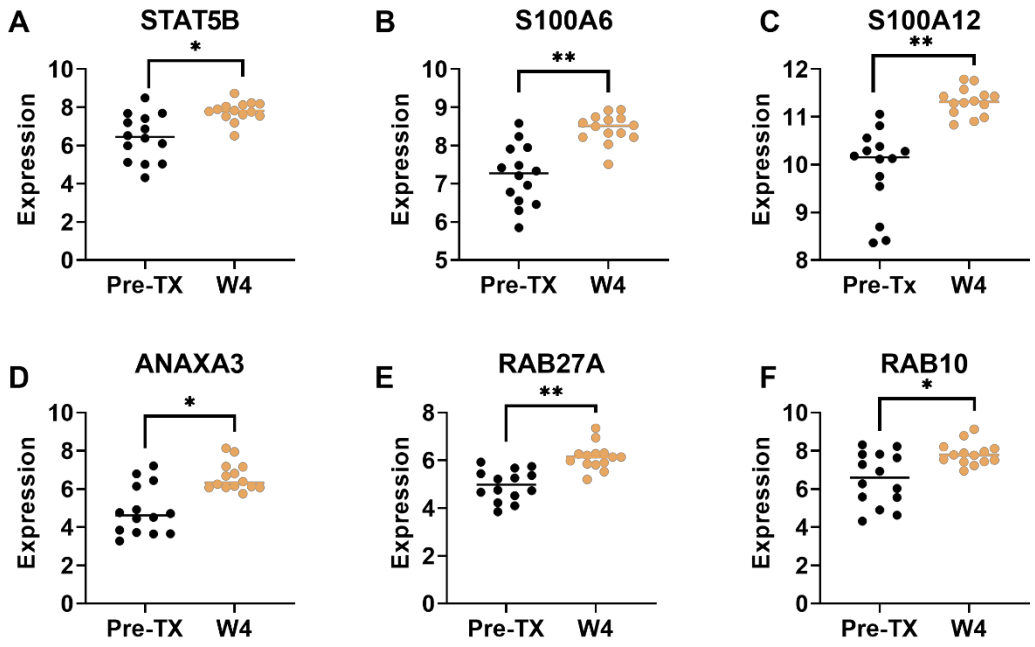

Figure 4-6 Upregulated genes in CTCs from Pre-TX to W4

Expression of upregulated genes: **A.** STAT5B, **B.** S100A6, **C.** S100A12, **D.** ANAXA3, **E.** RAB27A**, F.** RAB10. *p < 0.05, **p < 0.005, empirical Bayesian method, paired t-test FDR <0.05.

4. 6 Discussion

There is a critical need for technologies to monitor lung cancer in a non-invasive, repeatable manor that can predict which patients will have favorable outcomes on radiation therapy. Circulating tumor cells (CTCs) offer the exciting potential to directly profile tumor cells while only needing a peripheral blood draw. The GO Chip is a microfluidic device that uses immunoaffinity to capture CTCs on the surface of the device with high purity and sensitivity. In this work, we present the use of the GO Chip to isolate CTCs in treatment naïve, stage III NSCLC patients through radiation treatment.

We found that CTCs were present in 100% (n=26/26) of patients and in 92.7% (n=102/110) of blood samples, an average of 51.0 ± 94.4 CTCs/mL (range 0-504) across all timepoints. This is dramatically higher than the number of CTCs as determined by the FDA

approved CellSearch[45,224], demonstrating the necessity of using the GO Chip antibody cocktail of EPCAM, CD133, and EGFR, as opposed to just EPCAM like CellSearch.

CTCs were enumerated at six timepoints across radiation therapy and immunotherapy, however the most predictive timepoints were the Pre-TX and W4 of RT timepoints. While we found that the number of CTCs decreased during RT like several previous studies[200], this does not have an clinical implication as the absolute number of CTCs did not correlate with PFS at any timepoint. Instead, we did find that the change in CTCs between Pre-TX and W4 of RT was a promising marker of shorter PFS. Patients with an increase in CTCs only had 5 months of PFS (n=4) compared to 15 months average monitoring time (n=12) for patients with a decrease in CTCs (p=0.011, log-rank (Mantel-Cox) test, survival analysis). Similarly, patients with less than a 75% decrease in CTCs had 7 months of PFS (n=8) compared to 21 mo. average monitoring time (n=8) for patients with a large decrease in CTCs (p=0.0053, log-rank (Mantel-Cox) test, survival analysis). This is a dramatically shorter PFS and indicates the potential to use CTCs as an early predictor of progression. Additionally, because this finding uses the W4 timepoint, there is substantial time to alter patient treatment before progression, approximately 4-6 months.

A second interesting finding is that the patients who will have progression on durvalumab, an anti-PD-L1 immunotherapy, all had higher than average PD-L1+ CTCs at all measured timepoints. Although not statistically significant, we did find that having >50% PD-L1+ CTCs at Pre-TX was indicative of shorter PFS for patients receiving durvalumab, 14 mo. PFS (n=6) compared to 18.8 mo. censored monitoring time (n=10, p=0.069, log-rank (Mantel-Cox) test, survival analysis). Although we were unable to acquire matched tissue samples for this analysis, previous studies have shown high concordance between PD-L1 expression on CTCs and matched tumor samples.[225] The presence of PD-L1+ CTCs could have serious implications

for the efficacy of anti-PD-L1 immunotherapies. As CTCs have been shown to lead to metastasis[226], having high PD-L1 expression, an immune evasion protein[227], on the surface of CTCs may allow them to escape immune surveillance and continue to seed metastasis. One study even found that it was not sufficient to block simply PD-L1 on the surface of CTCs to stop metastasis, but instead it was necessary to block CD47 as well.[228]

Finally, differential gene analysis was performed using Affymetrix Clariom S PICO microarrays. Analysis code was written in R using the oligo and limma packages. There were significantly upregulated genes between Pre-TX and W4 that corresponded to a CTC phenotype that was invasive, proliferative, and potentially immune invasive. These CTCs may represent the cells that are escaping chemotherapy or radiative cell death. By having these highly tumorigenic cells circulating in the bloodstream, this may indicate a potential therapeutic target. This mRNA expression finding may also help explain how PD-L1+ CTCs in the blood stream may lead to future progression, as the CTCs express additional invasive markers. Final steps need to be completed for the RNA analysis of this work. First, DEGs need to be fully profiled and categorized to understand the phenotype of these CTCs, using methods such as gene ontology and gene enrichment analysis. We additionally still need to further subgroup the patients into stable vs progressing, to determine whether any genes are predictive of future progression.

In summary, this work demonstrates the potential to use CTCs to predict patient outcomes in stage III NSCLC using the highly sensitive GO Chip. To continue moving this work forward, a larger validation cohort will be needed to verify the finding of this pilot cohort of 26 patients. Additionally, further work is needed to understand the role of PD-L1 expression on CTCs and the impact of this finding on immunotherapy outcomes.

Chapter 5 Single Cell Droplet Microfluidic CellMag-CARWash to Study NK Cell EV Biogenesis

5. 1 Abstract

Single-cell characterization is becoming increasingly necessary as researchers continue to elucidate the role of cellular heterogeneity in biological processes and diseases, such as cancer. The study of single cells, however, is non-trivial; single-cell isolation and analysis devices need to be incredibly precise and face many challenges. While there are many methods proposed to perform single-cell isolation and analysis, microfluidics are optimal technologies because of their small scale and ability to manipulate fluids on the pico- and micro- scale. Droplet microfluidics offer the opportunity to isolate target cells in aqueous droplets suspended in oil, allowing for single-cell analysis. Combining droplet microfluidics with well-known immunoaffinity magnetic isolation techniques, here we present the adapted CellMag-CARWash droplet microfluidic system and optimized the workflow to isolate single NK92-MI cells into single cell droplets. The isolated NK cells are then used to investigate the heterogeneity in extracellular vesicle excretion in the presence of known NK cell activators.

5. 2 Resulting Publication Information

E. Purcell*, C. Cook*, B. Rupp*, N. Mesyngier, A. Radomski, A. Kaehr, R. Bailey, S. Nagrath. "Droplet microfluidic MagCell-CARWash elucidates single-cell EV heterogeneity in activated NK cells." *In preparation*

5. 3 Introduction

Cellular heterogeneity in diseases such as cancer has become increasingly well studied as researchers begin to understand how cellular differences can affect everything from immune function[229] to drug resistance.[230] As such, a myriad of single cell analysis techniques are being developed, ranging from single cell isolation technologies[231] to single cell functional assays.[232] Technologies that combine both isolation and biological assays allow for shorter processing times, minimal hands-on time, and decreased sample loss compared to needing to isolate and then perform an assay. The most common single cell isolation techniques are fluorescence activated cell sorting (FACS)[233,234], magnetic activated cell sorting (MACS)[235,236], manual cell picking, and microfluidics.[237,238] FACS, MACS, and manual cell picking offer the ability to isolate single cells but require large sample volumes or tissue samples and require post-processing for analysis beyond protein expression. Additionally, after separation using FACS or MACS, downstream applications need to be performed by hand, with reagents added to each well. Microfluidic technologies, however, can alleviate these many of these challenges, allowing for isolation and characterization to be performed in an automated fashion.

Microfluidic technologies for single cell isolation are becoming increasingly promising; the small scale of microfluidic devices allows researchers to manipulate fluids on a pico- and micro- scale, thereby minimizing assay volumes. Commercial single-cell microfluidic technologies are available, the most notable of which is the DEPArray from Menarini Biosystems. This system uses dielectrophoresis to route cells through a microfluidic chamber; cells are selected by the user based on fluorescent antibody attachment, similar to FACS.[239] This technology, however, takes lengthy processing time and has been primarily used for fixed or FFPE samples up until this point.[240] The DEPArray is also not a combined

isolation/characterization system, requiring users to optimize downstream applications separately, such as PCR DNA anlalysis.[241]

A second commercially available microfluidic cell sorter, integrated fluidic circuits (IFCs), were developed by the Quake group and commercialized by Fluidigm.[242] IFCs facilitate isolation of single cells in nanoliter-sized chambers by a system of pressure controlled microfluidic valves that can cut off fluid flow in selected channels. While these circuits have been applied to obtain single-cell level genetic analyses[243–245], they are limited in the total number of cells interrogated based on the size of the device.[246] Additionally, their fabrication and operation require more complex techniques and training, which limits their widespread application.

A popular research-scale example, deterministic lateral displacement (DLD), is a microfluidic cell sorting technique that employs an array of pillars to separate cells into different streamlines as a function of their hydrodynamic diameter.[247] DLD can discriminate between cells based on size, shape, and deformability, and can separate multiple cell types at a time.[237] However, it is subject to low throughput from high fluidic resistances on device as well as issues with clogging that can be difficult to eliminate.[248] Most challengingly, DLD strategies do not yet yield single-cell solutions, despite their label-free and high purity advantages.

A sub-type of microfluidic devices, droplet microfluidic devices are technologies that isolate single cells into aqueous droplets surrounded by an oil phase.[249] Single cell droplet microfluidics allows researchers to isolate single cells in droplets, before manipulating the droplets to isolate cells of interest and perform assays.[250] Cells are either introduced to droplet systems as a pure population and diluted to achieve single-cell concentrations [251,252], or sorted into distinct populations either through passive or active methods.

One successful commercially available single cell droplet microfluidic technology, 10X Genomics, uses serial dilution to achieve single-cell concentrations, meaning target cells need to be a high proportion of the sample to ensure sufficient detection. This technology does offer a wide array of single-cell assay options, ranging from genomics[253] to transcriptomics.[254] On a research scale, DeKosky et al. developed a droplet microfluidic system that uses pure cell populations to sequence antibody repertoires from B-cells.[252] Non-sorting technologies, however, require pure cell populations, which can be challenging to achieve from blood or other complex fluids, and frequently require a large cell volume.

Active sorting methods within single-cell droplet microfluidics frequently use fluorescence-based systems that isolate cells based on the presence of fluorescent signal either directly on cells or using a reporter antibody.[246,255] Active sorting methods, however, are complicated systems, requiring the use of actuatable external fields. The triggering of these fields must be spatially engineered and closely timed with the detection of an appropriate signal, which necessitates droplet ordering and limits the window for observation.[256] Depending on the field used, active droplet sorting may also require expensive equipment to monitor droplets and generate sorting pulses.[257] While active sorting does have many advantages, including being able to isolate cells based on several characteristics, however, it can be challenging to introduce fluorescent molecules or probes into droplets.[258] Active droplet sorting depends on a successful chain of events, including detection of cells/droplets of interest and synchronized timing of external field actuation. This can be challenging to achieve in concert, leading to cell loss.

Passive sorting methods, however, allows for the precise and reliable isolation of specific cell populations, with comparatively simple mechanics. Magnetic sorting is an incredibly common passive sorting mechanism and offers optimal integration into droplet microfluidic

devices. Magnetic-based cell isolation microfluidic devices are common, with groups frequently develop these technologies to isolate rare circulating tumor cells.[259,260] Magnetic-based single-cell droplet microfluidic systems would allow for the isolation of specific cell populations without the need to add fluorescent probes or dyes, thereby expanding the potential downstream assays. Several droplet systems have been developed to isolate magnetic particles, including the CAR-Wash device, created by Doonan et al. The CAR-Wash system accepts an input of particles in droplets, coalesces droplets into a wash buffer, isolates specifically magnetic targets, and then reforms droplets in the product stream.[261] Off-target cells escape through a waste outlet, allowing for the pure isolation of magnetic particles in a clean aqueous medium, like cell culture media. While this device has been used for only magnetic beads up until now, it offers the incredible potential of isolating single cells with high purity.

One of the principal benefits of single-cell droplet microfluidic systems is the ability to combine single-cell isolation and analysis into one stream-lined workflow to study unique aspects of cellular heterogeneity. Natural killer (NK) cells are a type of lymphocyte that works as the body's early defense system to fight against foreign invaders via the innate immune system. As part of this innate immune system, NK cells are known to secrete a variety of signaling molecules including cytokines, chemokines, and extracellular vesicles (EVs).[262,263] EVs are nanoparticles that are secreted from most cell types and contain protein, mRNA, and lipids from the parent cell.[264] After secretion, EVs can circulate through the body and be uptaken by other cells, allowing for intercellular signaling. The signaling pathways of NK cells via cytokines and chemokines has been well explored in previous studies,[262,265] however the study of EVs is a developing area of research.

While initial studies have demonstrated the cytotoxic effects of NK-EVs[156,157,266], there remain many challenges when aiming to use NK-EVs as a therepeutic. One critical question is whether activated NK cells generated more or fewer NK-EVs. Federici et al. showed that NK-EVs further activate additional CD56+ NK cells[267], which would be critical to enhance the efficacy of an NK-EV therapy. It has already been shown that T-cells and B-cells require activation before EV generation.[268–271] As such, we are particularly interested in further expanding the previous knowledge to understand the heterogeneity of NK-EV excretion in the presence of various NK stimulatory molecules, such as IL-12.[272]

Here, we describe the adaptation and use of the droplet microfluidic CARWash system, here called the CellMag-CARWash to isolate single NK cells tagged with anti-CD56 Dynabeads™. This technology is then applied to understand the heterogeneity of EV biogenesis from single NK cells, in droplets, under the presence of NK activating molecules. The CAR-Wash system was originally developed to isolate green fluorescent protein–histone H2B fusion protein bound to magnetic beads, where beads are pulled to the edge of the device using a magnet before being collected into a product stream, allowing off-target protein to be washed away. In this study, NK-92MI cells were isolated from both pure and mixed cell populations using the CellMag-CARWash system. The efficiency and purity of this system was quantified, initial studies were conducted to assess the viability of cells after processing through the CellMag-CARWash system. To further characterize the single cell EV secretion, we performed preliminary analysis demonstrating the potential of using GFP cells to generate GFP-EVs. The CellMag-CARWash system allows for specific isolation of viable target cells, thorough washing of the isolated target cells, re-encapsulation of single cells into single droplets, and has a rapid

processing time, making it an optimal technology for analyzing fragile immune cells, such as NK cells.

5. 4 Methods

5.4.1 Cell culture

NK-92MI cells were cultured in a T75 flask with 10 mL of minimum essential medium (MEM, Thermo Fisher) alpha supplemented with fetal bovine serum, horse serum, and antibiotic-antimycotic. Jurkat cells (T-cells) were cultured in a T75 flask with 10 mL of Roswell Park Memorial Institute (RPMI, Thermo Fisher) supplemented with fetal bovine serum and antibiotic-antimycotic. To better visualize cells and improve the analysis, NK cells and T-cells were fluorescently labelled CellTracker dye (Thermo Fisher). Cells were removed from culture, washed with PBS to ensure no serum remained and resuspended in 5mls of serum free media and 5µL of CellTracker. The cells incubated for 30 minutes at 37℃ before being washed twice with PBS to remove the remaining CellTracker. K562 GFP cells were cultured in a T75 flask with 10 mL of Dulbecco's Modified Eagle medium (DMEM, Thermo Fisher) supplemented with fetal bovine serum and antibiotic-antimycotic.

5.4.2 EV harvesting

To harvest EVs, cells were counted, and 1.5 million cells were added to a dish with 8mLs of the appropriate serum full media, as above. Cells were allowed to recover in media for 24 hours before being washed with PBS to remove EVs from serum and were reseeded in EV free media. Cells were then incubated for 24-72 hours to allow for the secretion of EVs. After incubation, EVs were removed and the isolated using the **Ultracentrifuge** protocol, **Chapter 3.**

5.4.3 Magnetic Bead Attachment to NK cells

To isolate NK cells using magnetic beads, NK-specific antibodies were first conjugated on to magnetic beads before attaching the magnetic beads to the NK cells, **Figure 5-1.** To isolate NK cells using magnetic beads, NK-specific antibodies were first conjugated on to magnetic beads before attaching the magnetic beads to the NK cells. First, the streptavidin coated M280, 2.8µm Dynabeads™ (ThermoFisher) were removed from the sterile bottle and rinsed 5x with 0.2µm filtered PBS by pressing the magnet to the side of the tube, allowing the liquid to be removed and the beads left behind. The clean beads are then resuspended in their original volume of 0.1% BSA in PBS. Biotinylated anti-CD56 antibodies (R&D Systems, cat# BAF2408) are then incubated with the beads at room temperature for 30 minutes on a rocker, allowing the biotinylated antibodies to bind with the streptavidin coated Dynabeads™. Following antibody binding, excess antibody was rinsed off by diluting the bead-antibody solution with 1mL of 0.1% BSA in PBS. The beads are then again trapped using the magnet, allowing the solution to be removed. The anti-CD56 conjugated beads are rinsed 4 times. After conjugation, the anti-CD56 conjugated beads are incubated with the cells of interest for 30 minutes at room temperature on the rocker. Before further experimentation, bead-tagged cells are imaged to ensure effective bead attachment.

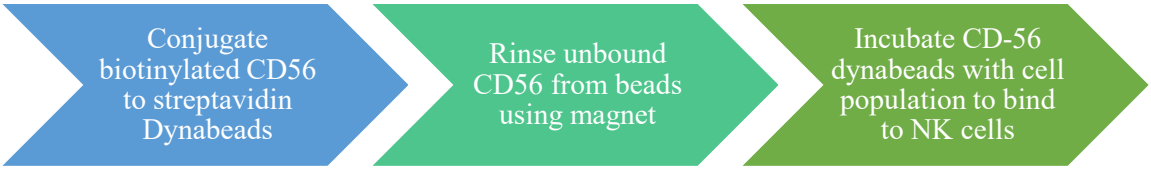

Figure 5-1 Workflow for CD-56 Dynabead conjugation and attachment to NK cells

5.4.4 Droplet generator and CellMag-CARWash device fabrication

Device fabrication has been described previously.[261] Masters are fabricated using standard photolithography techniques. SU-8 2025 negative epoxy photoresist is spin coated to a thickness of ~40 μm on a silicon wafer and baked. It is exposed to UV light through a design mask transparency obtained from CAD/Art Services, Inc. Device designs are constructed using AutoCAD software. Unpolymerized photoresist is removed via development in propylene glycol monomethyl ether acetate. After baking, wafers are treated with tridecafluoro-1,1,2,2-tetrahydrooctyl trichlorosilane using chemical vapor deposition. To fabricate devices, polydimethylsiloxane (PDMS) is mixed at a 10:1 ratio of base to curing agent, degassed, and poured onto the master. Once cured, the PDMS stamp is cut out and ports are punched out using a 30-gauge needle. The stamp is bonded to a glass coverslip via oxygen plasma activation.

5.4.5 Droplet generator and CellMag-CARWash set-up

All devices are treated prior to the experiment with aquapel (Pittsburg Glass Works, cat#47100); this incubates for one minute before being flushed and replaced with FC-40 oil (Sigma Aldrich, cat#F9755). Pieces of tubing are inserted into the device ports then their respective pressure vial. The output tubing of each device leads to a 0.6-mL Eppendorf tube for collection. 1% Fluorosurfactant-008 (RAN Biotechnologies, Inc, 008-FluoroSurfactant-1G) in Novec 7500 oil (The 3M Company; Novec 7500) comprises the oil samples flowed on device.

Reagents are delivered on device using a custom-built pressure controller. Nitrogen gas is directed into two splitting manifolds that connect to several two-stage regulators. These regulators allow for pressure selection. The gas then passes through an array of LHDA0531115H solenoid valves that actuate in response to LabView signals from an NI PCIE-6251 multifunction

data acquisition device. The headspace of reagent vials is pressurized via steel pins, and reagent is driven onto the devices via 20-centimeter long pieces of #30 PTFE tubing. Both the droplet generation and CellMag-CARWash devices are imaged on a Leica DMi8 light microscope, and videos are captured using a VEO 640L high-speed camera from Vision Research Inc. Image processing occurs using ImageJ software from the NIH.

5.4.6 Single cell droplet generation

We have previously described the droplet generation process, *Steve et al*, thus here we described the specifications for this system. The cell solution is pipetted to mix the contents before 30-50 µL is aspirated to load into the "sample hopper". The hopper consists of a cut 200 µL pipette tip placed inside a pressure vial and connected to the device via 5 cm length of #30 PTFE tubing and 5 mm length of connector tubing. This vial is positioned upside down so the sample remains inside the pipette tip. The pressures are set according to the following table and applied on device via a custom pressure controller.

Table 5-1 Droplet generation specifications

Pressure Vial	**Port**	**Pressure (kPa)**
1-2	Oil	75
1-3	Cell Sample	60

Device operation takes between 5 and 15 minutes, depending on sample size. At the end of operation, air enters the device, at which point the sample pressure (1-3) is turned off to allow the oil to rinse the sample hopper. At this point, sample loading and device operation can be repeated. The device can be re-used several times for samples of the same identity. Device

usability is determined through brightfield imaging of the device to check for blockages or contamination.

5.4.7 CellMag-CARWash processing

After connecting the tubing of each port to the device, electrode syringes containing 3M sodium chloride are connected to the electrode ports. Eight Neodymium magnets are installed on the device, approximately 400 µm away from the washing channel, with four above and four below the coverslip. At this point, each piece of tubing from the device is inserted into its respective pressure vial:

Table 5-2 CellMag-CARWash specifications

Pressure Vial	Port	Pressure (kPa)
1-1	PBS or cell media	45
1-2	Oil coflow	40
1-3	Droplets	35
1-4	Oil spacer	45
2-5	Oil resegmenter	30
2-6	Waste	15

A platinum wire is placed into the low salt buffer vial and connected to the working electrode. The ground electrode is attached to the needle of one of the electrode syringes.

Droplet samples are rinsed by drawing up the oil phase in a syringe and injecting it onto the top of the droplets. Much of the oil phase is removed before using a razor blade to cut off the neck of the tube. The cut tube is then set inside the sample pressure vial (1-3). Pressures are applied and adjusted as necessary to achieve smooth flow within the device. Once all droplets have traveled

through the device, the sample and waste pressures are turned off, so the wash buffer and oil can rinse the sample input tubing and carry all resegmented droplets into collection. Operation time typically takes between 15 and 45 minutes, depending on sample size. Similar to the droplet generator, the CellMag-CARWash can be reused for replicate samples, but a new device is set up for different sample types.

5.4.8 Post CellMag-CARWash droplet processing

Following droplet generation and CellMag-CARWash processing, cells in droplets (referred to as simply droplets) are stored on ice during transport, ~30 minutes. The droplets are either kept intact to investigate droplet stability and cell viability in live cell experiments, or coalesced using 1H, 1H, 2H, 2H-perfluoro-1-octanol (Sigma Aldrich, cat# 370533) to gather the cells into the aqueous phase for ease of counting.

Droplet coalescing

Droplets that have been coalesced separate into an aqueous or oil phase. The cells are removed from the aqueous phase and put into a well plate for imaging.

Intact droplet imaging

To study droplet stability, or cells in droplets, droplets are then either incubated in a 1.5mL tube or loaded into a microfluidic incubation chamber. The incubation chamber is the same PDMS top that is used in the GO Chips from **Chapter 4,** but briefly is a 50µm tall single chamber that is approximately the dimensions of a 1”x3” glass slide**.** The difference here is that the PDMS chamber is bonded using an O2 plasma etcher directly to a glass slide, creating one large chamber. Incubation chambers are first primed with oil before loading the droplets using a Harvard syringe pump at 10µL/min. Droplets in either tubes or incubation chambers are stored at 37°C until imaging.

5.4.9 Live/Dead analysis

Live/Dead Viability Kit (Invitrogen Kit #L3224) was used to determine the viability of cells within the droplets. However, it was not possible to easily introduce the assay to the droplets. Instead, a portion of the droplets were placed in a well plate and excess PBS was added. By mixing the droplets with the excess PBS this caused the droplets to break and cells to gather in the PBS solution. The PBS solution was then removed from the oil, placed in a new well and 0.5ul of calcein-AM and 0.25ul of ethidium homodimer-1 was added to the cell suspension. The solution incubated for 30 minutes in the dark before being imaged using fluorescent microscopy. Cells were counted as either live or dead based on the presence of green (calcein/live stain), red (ethidium homodimer-1/dead stain), or both.

5.4.10 Fluorescent imaging and analysis

Droplets with cells are imaged using a Nikon Ti2 Eclipse inverted microscope. Droplets are imaged at 6x magnification to assess overall droplet stability and at 60x magnification when looking at cell stability and viability, or EVs in droplets. Images are taken in brightfield to look at the droplets and cell morphology, and fluorescent channels to quantify pre-fluoresced cells and EVs.

5. 5 Results

The CellMag-CARWash system presented an optimal solution for isolating clean, pure target cell populations using immunoaffinity magnetic beads. In this study, we present the adaptation of the CAR-Wash droplet microfluidic system to isolate single NK cells in droplet. We then aim to use these single, live NK cells to study EV excretion rate between individual cells, **Figure 5-2**. As a brief overview, magnetic beads are first attached to cells before being processed through the droplet generator device. This device isolates each cell into an individual aqueous droplet separated by oil using a common T-junction, one of the hallmark droplet generation techniques. The droplets are then processed through the CellMag-CARWash device where the magnetic bead tagged cells are reintroduced in droplets after positive selection isolation. These single-cell droplets are then incubated to generate EVs for quantification.

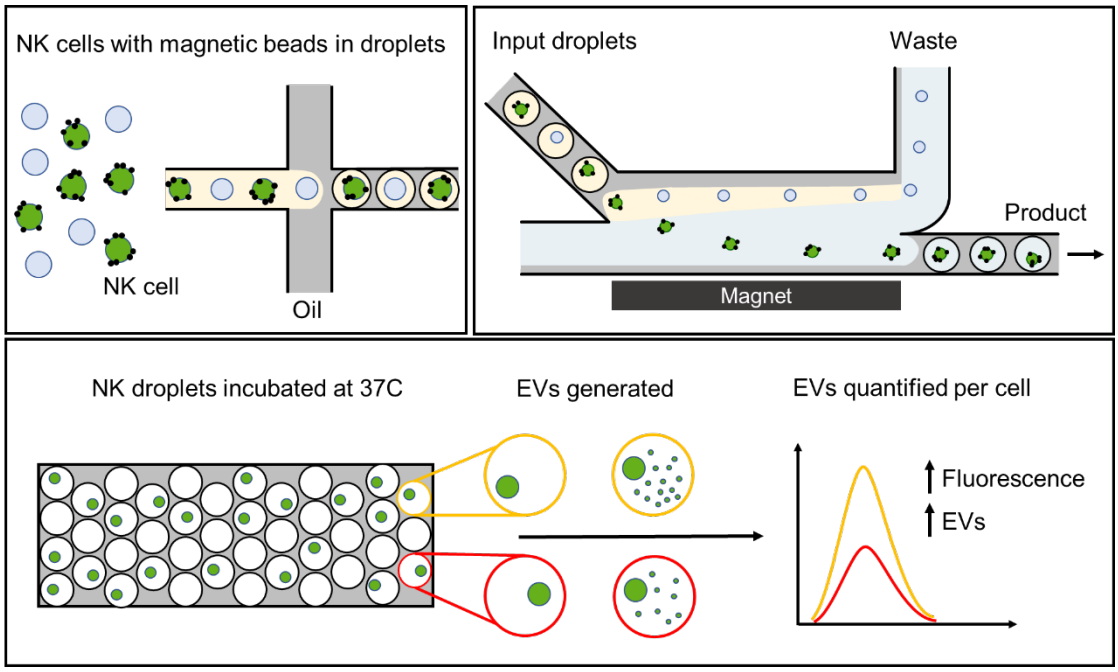

Figure 5-2 Overview of the droplet CellMag-CARWash system.

5.5.1 Magnetic Bead Attachment Optimization

In this study, we attached antibody-conjugated magnetic Dynabeads™ to cells to mimic the magnetic particles used in the original CAR-Wash study. These magnetic beads need to be attached to the cells of interest with high specificity, ensuring we only isolate the target cells—NK92-MI cells—while letting non-specific cells pass through. Additionally, we need to ensure adequate bead attachment to capture cells using the CellMag-CARWash, while not having excess unbound beads in the solution.

Several parameters were optimized to ensure the effective bead attachment, including antibody concentration, bead concentration, and incubation concentration and duration. Briefly, M-280 streptavidin conjugated Dynabeads™ were incubated with anti-CD56 antibodies for 30 minutes at room temperature. Following incubation, excess antibodies were rinsed from the beads using a magnet. The anti-CD56 Dynabeads were then incubated with the cells for 30 minutes on a rocker at room temperature. Optimization experiments were performed using the NK-92mi cell line. It was found that the optimal concentration of antibodies:beads is 1:2 by volume, and a 30 minute incubation was sufficient for the anti-CD56 conjugated Dynabeads to

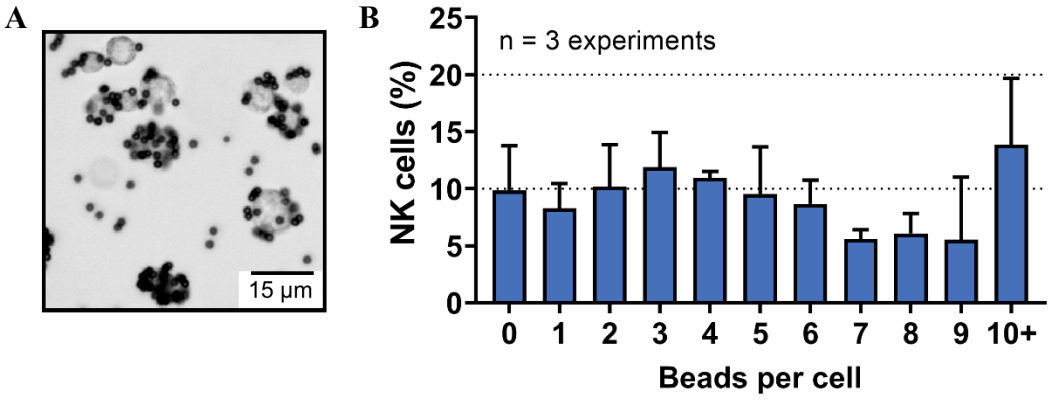

Figure 5-3 Anti-CD56 Dynabead™ attachment to NK92-MI cells

A. Representative image of bead attachment on NK cells **B.** Quantification of the number of beads per cell per NK cell, shown here as a percent of the NK cells in the sample. Mean is plotted, error bars show standard deviation, n = 3 experiments.

bind to cells. Representative images are seen in **Figure 5-3A.** Finally, the number of anti-CD56 Dynabeads per cell was quantified. It was found that there was an even spread between 0-10+ beads per cell, **Figure 5-3B**. It was not however known whether this would be sufficient beads attachment to capture cells using the magnet within the CellMag-CARWash system.

5.5.2 NK isolation using CellMag-CARWash

To determine the potential of the CellMag-CARWash system to isolate NK cells using the anti-CD56 Dynabeads™, we first used a pure population of NK-92MI cells. To start the experiment, NK cells were fluoresced using CellTracker before being incubated with the anti-CD56 Dynabeads and fixed with PFA. The cells were processed through the droplet generator device before being sent through the CellMag-CARWash; both the product and waste streams were collected. As seen in **Figure 5-4**, NK cells with sufficient beads attachment are collected into the bottom, product stream.

To determine how many beads are needed to successfully isolate NK-92MI cells, we quantified the number of NK cells in both product and waste streams, as well as the number of

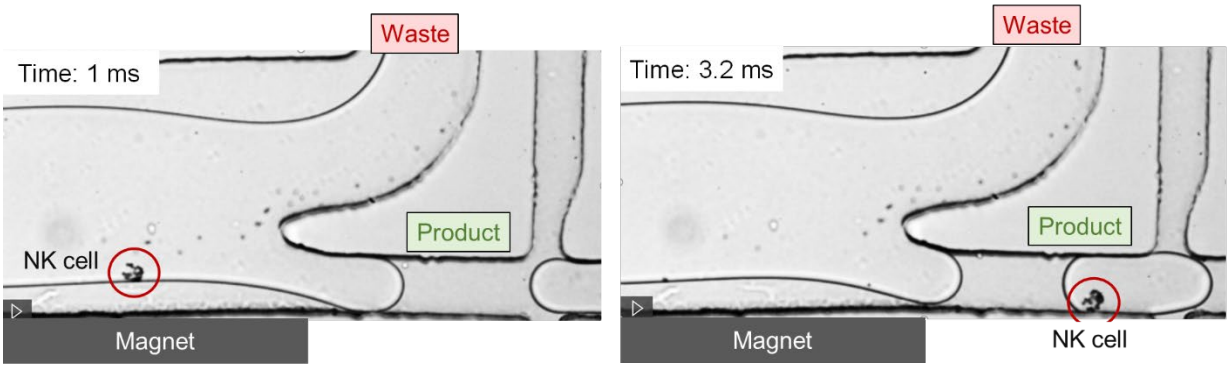

Figure 5-4 Images of NK-92MI cells isolation in the CellMag-CARWash device.

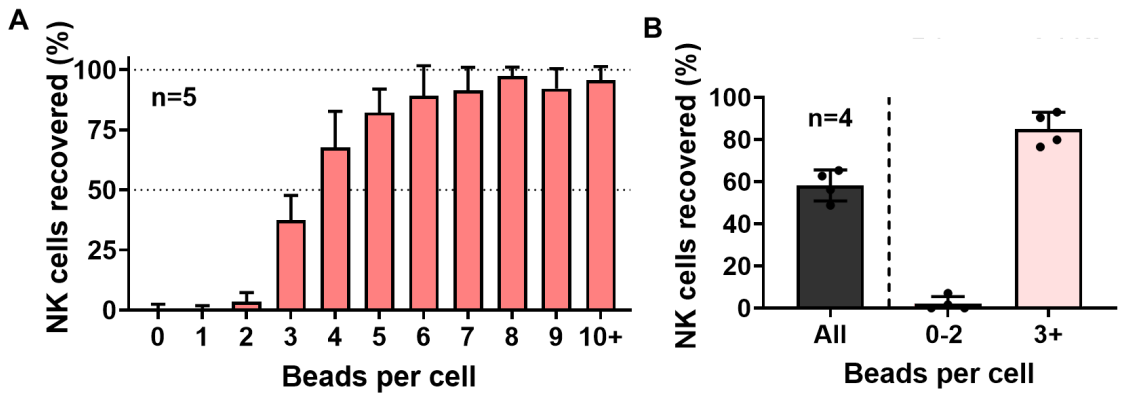

Figure 5-5 Quantification of cells in product stream after CellMag-CARWash.

A. Number of beads per cell in the product stream, shown as percent of cells with the given number of beads found in the product stream. **B.** Overall recovery of NK92-MI cells and recovery of NK cells split into cells with 0-2 beads and 3+ beads. Mean is shown, error bars are standard deviation, n=5 and n=4 experiments.

beads per cell in both streams. By first looking at solely the product stream, it was found that 3 beads per cell led to an isolation rate of 37% ± 10 (n=5), with the rate increasing for each additional bead attached, **Figure 5-5A.** We then calculated the percent recovery for all NK cells, regardless of the number of the beads attached, **Equation 1**. The overall percent recovery of the NK-92MI cells was 58% ± 7 (n=4), **Figure 5-5B**. However, for cells above the threshold of 3 beads per cell, as found above, the recovery was 85% ±9 (n=4). We did find that for cells with 0-2 beads, the recovery was a dismal 2% ± 3 (n=4).

$$\%\, recovery = \left(\frac{\#\ of\ cells\ in\ product}{\#\ cells\ in\ product + \#\ cells\ in\ waste}\right) \times 100 \qquad (1)$$

We then investigated mathematically whether the system, as is, has a physical limitation of only capturing cells with 3+ beads. To perform this analysis, we used the framework laid out by Jack et al who was inspired by Derec et al, Kokkinis et al, and Schneider et al.[273–276] The number of beads can be calculated based on the time it takes for a bead to traverse the width of

the CellMag-CARWash device and the time it takes for a cell to migrate the length of the CellMag-CARWash device.

First, the residence time of unbound NK cells in the CellMag-CARWash is calculated by flowing clean cells, in droplets, through the CellMag-CARWash device. It was measured that the NK cells flow at a linear velocity, u_x, of 111±8 μm/ms. Therefore, it takes an unbound cell 107±7 ms to travel a length of 12mm through the CellMag-CARWash, or the typical residence time of a cell in CellMag-CARWash is 107 ms. The residence time is the maximum available time within which a target cell must be pulled from the top of the channel at the entrance of the CellMag-CARWash to the bottom of the channel at the product outlet stream. Using the vertical distance of the device, L_y = 120 μm, we calculate that the linear y-velocity of a cell needs to be 1.02±0.07 μm/ms for an NK cell to be captured.

In the CellMag-CARWash, all linear y-velocity is achieved by the magnetic pull on the NK cells from the attached magnetic Dynabeads, F_M. Jack et al. state that the velocities of superparamagnetic microparticles are proportional to the magnetic field gradient.[273] Assuming negligible electrostatic and Van der Waals forces, we can then say that the magnetic force F_M, and the drag force F_D acting on the particle are balanced. Applying Stokes law under laminar flow,

$$3\pi\eta u_t D_{bead} = F_{Dbead} = F_{Mbead} \quad (2)$$

where η is fluid viscosity, u_t is terminal velocity in the y-direction, D_{bead} is particle particle diameter, and F_D is drag force. If we assume that the beads do not significantly change the

diameter of the cell, then we can approximate the magnetic force on a cell as the sum of the magnetic beads attached to that cell.

$$F_{Mcell} = [N \times F_{MBead}] \quad (3)$$

By then applying Stokes law, **Eq 2**, we can state that

$$[D_{cell} \times u_{ycell}] = [N \times D_{bead} \times u_{ybead}] \quad (4)$$

where D_{cell} is the diameter of the cell, u_{ycell} is the linear y-velocity needed to traverse the width of the channel as calculated above, D_{bead} is the diameter of the bead, and u_{ybead} is the linear y-velocity of a Dynabead™. The final variable, u_{ybead} , was also calculated experimentally as 3.0 ± 0.7 μm/ms; pure M-280 Dynabeads were flowed into the CellMag-CARWash and their y-velocity was calculated by simply measuring the difference in y-distance between two timepoints.

Through our calculations we determined that 1.8 ± 0.4 M280 Dynabeads™ are needed per NK cell to achieve capture into the product stream. This is only ~1.2 beads fewer than we determined through our experiments, indicating that there are other factors affecting the collection of NK-cells in the CellMag-CARWash.

5.5.3 NK isolation using CellMag-CARWash from mixed cell sample

To quantify the isolation specificity and purity of the CellMag-CARWash system, we then created a mixed sample of NK-92mi and Jurkat T-cells to mimic cells found in blood. First, we incubated anti-CD56 Dynabeads™ with the mixture of cells to ensure that the antibody is specific to NK cells. A representative image is seen in **Figure 5-6A,** with no beads found on the T-cells and the usual number of beads found on the NK-cells. Following bead attachment, the cells were processed into droplets and then through the CellMag-CARWash system. The input mixture was 55% ± 5 NK cells and 44% ± 5 T-cells. Following CellMag-CARWash, the product stream was an excellent 94% ± 2 NK cells and only 6% ± 2 T-cells, **Figure 5-6B**. The overall recovery of NK-cells was 42% ± 14, **Figure 5-6C.**

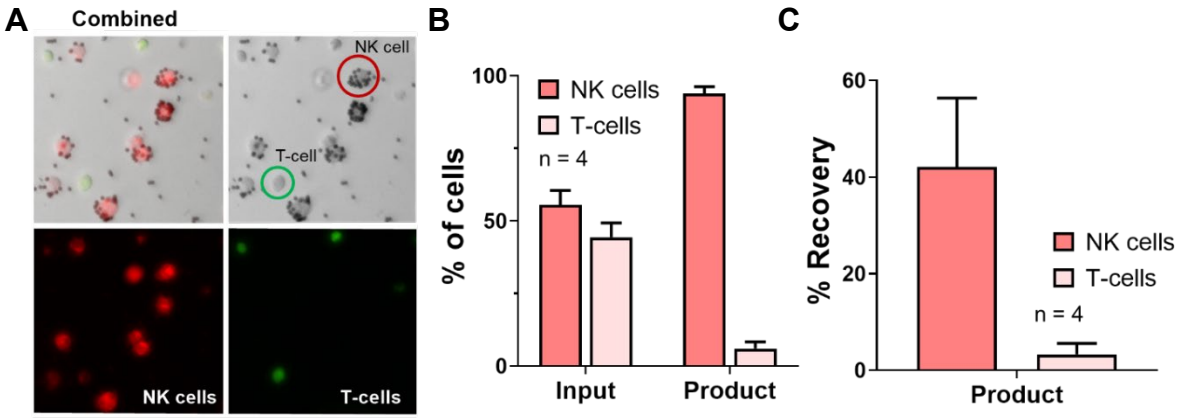

Figure 5-6 Isolation of NK92-MI cells from a mixed NK and T-cell population.

A. Brightfield and fluorescent images of the cell mixture after bead attachment. The NK cells have the usual number of beads while the T-cells have no beads. **B.** The components of the input and product stream, or before and after CellMag-CARWash processing. **C.** Percent recovery of NK and T-cell after CellMag-CARWash device. Mean is graphed, with error bars denoting standard deviation, n=4 experiments.

5.5.4 Droplet stability and NK cell viability

Following the isolation of pure NK cells, we then investigated the stability of those single-cell droplets. To image the droplets, it is necessary to load the droplets into single layers,

otherwise the droplets overlap each other, making imaging impossible. We used the PDMS chamber (top) of the previously described GO chip, however here we simply bonded the chamber to a glass slide to form a chamber, called here an incubation device. The droplets are loaded into the incubation device after first filling the device with oil to ensure smooth droplet loading.

We first investigated two workflows for droplet incubation and loading. NK cells were processed into droplets through the CellMag-CARWash before either being (1) stored in the incubator in a 1.5 mL Eppendorf tube in suspension or (2) loaded into a primed incubation device. Both methods, in-tube and on-chip, were stored at 37°C, with no added CO_2. At four time points a new incubation device was loaded using droplets stored in a tube and the droplets stored on-chip were imaged, **Figure 5-7.** At times 2 and 8 hours, the droplets are sturdy in both methods, with well-defined borders and filling approximately the same amount of the incubation

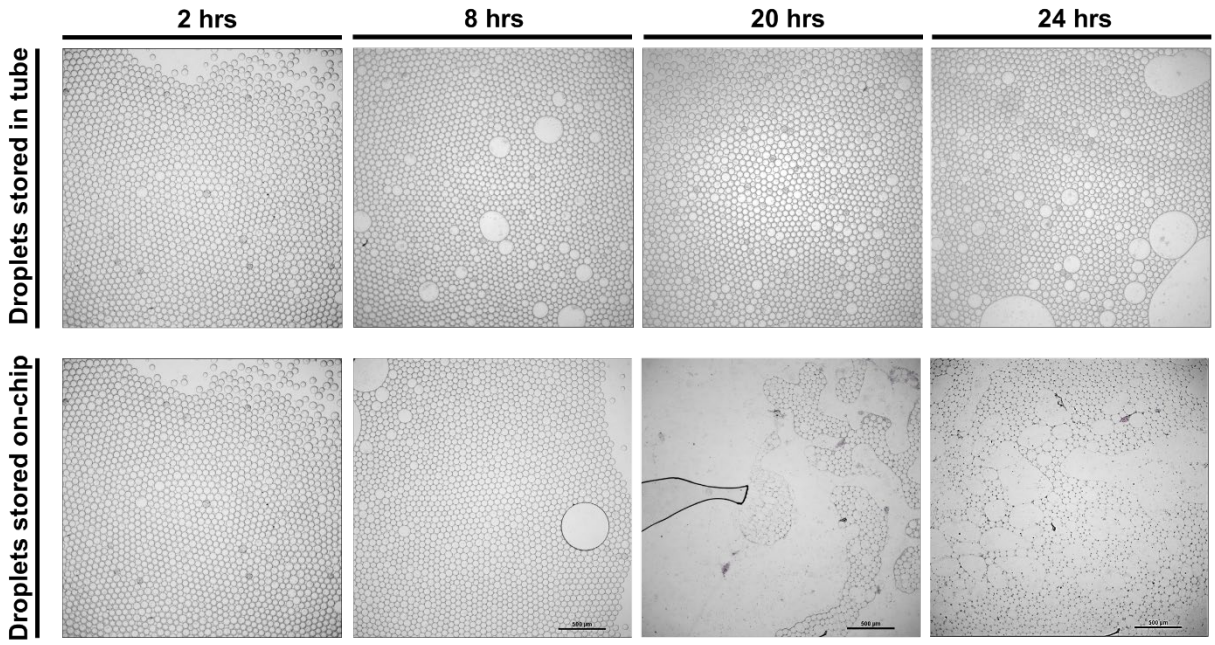

Figure 5-7 Droplet stability in tube and on-chip.

A time course of 2-24hrs (**left to right**) was performed for both droplets incubated in a tube (**top**) and droplets stored in an incubation device, on-chip (**bottom**), both were stored at 37°C.

device as at the first timepoint. However, by time 20 and 24 hours, the droplets stored in the tube were significantly more stable compared to the droplets stored on chip. Hence, the droplets will need to be stored elsewhere and then loaded into an incubation chamber.

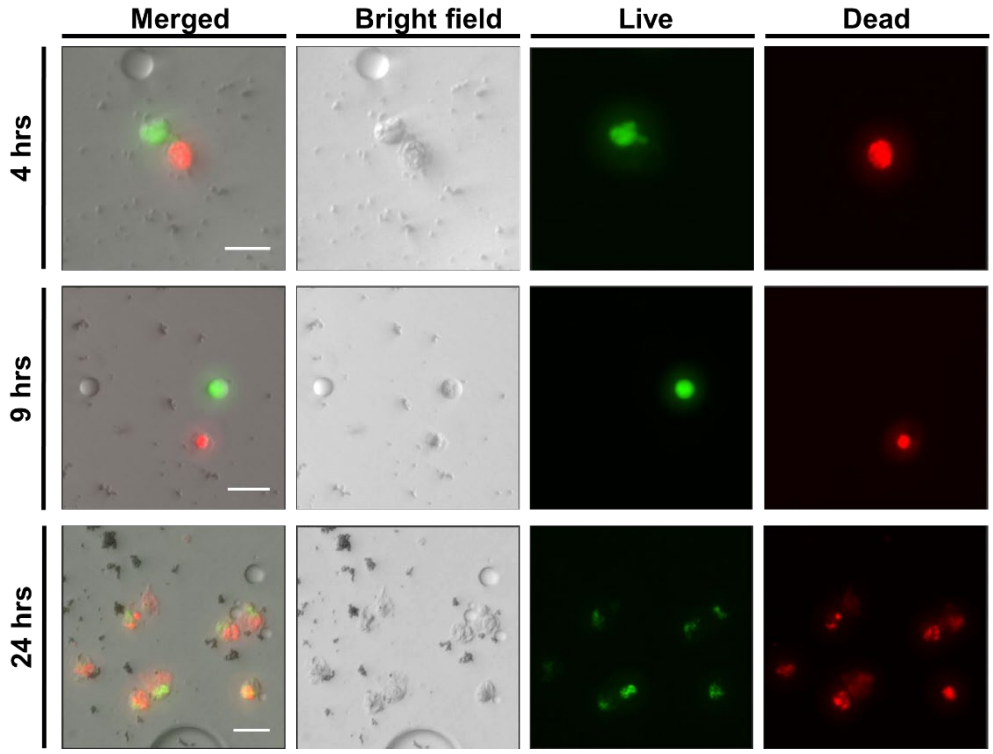

Figure 5-8. Cell viability as tested with live/dead assay.

However, there were concerns about the viability of the cells; single cells are challenging to culture and the gas exchange through oil is already low before encapsulating the cells in a tube or device. To assess the viability of the cells in droplets, droplets were stored in a tube at 37°C. At 4, 9, and 24 hours after droplet generation, a portion of the droplets were removed from the tube and excess PBS was added to coalesce the droplets. The aqueous layer was then removed, and a live/dead viability assay was performed, **Figure 5-8.**

At 4 hours, the cells were either distinctly alive, green, or dead, red. This held true at 9 hours, where most of the cells were either dead or alive. However, at 24 hours, there was a new population of cells: cells with compromised cell membranes, indicating recent cell death. This is shown in **Figure 5-8** as the partially red, partially green cells. We then quantified the number of each population of cells: live, dead, and recently dead. We found that at 4 hours, 77% of cells were alive, but by 24 hours only 6% of the NK cells were alive, **Figure 5-9**. At 24 hours we do see a large portion of the cells we have termed recently dead cells, 42%, these cells indicate that there is room for improvement in incubation strategy that could lead to longer viability than 9 hours.

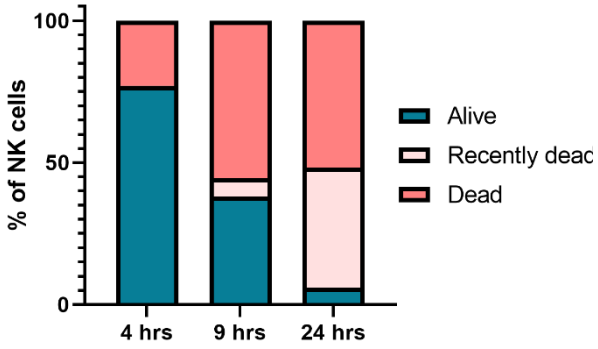

Figure 5-9 Live/dead results from NK cells following the CellMag-CARWash system.

The single NK cells were isolated into droplets of whole media following the CellMag-CARWash system, meaning the cells have the necessary nutrients for growth. However, they were stored in a tube, and hence there was no gas exchanged. Cells are normally cultured with 5% CO_2. We think that altering the storage conditions of the droplets, maybe in a well plate or a culture dish, will allow us to incubate the droplets in a CO_2 rich environment. Additionally, it has been shown that gasses diffuse more slowly through oil, so increasing the CO_2 concentration may create a more aggressive gradient, allowing more CO_2 penetration into the droplets. We hope that these changes will allow us to increase the viability of the cells in droplets.

5.5.5 EV quantification in droplets

Finally, we began investigating the feasibility of quantifying EVs in droplets. We did not want to add anything to the droplets, such as a reporter, for fear of EV loss. Additionally, every additional processing step is more time that the cells are either off ice or out of the incubator—leading to more potential cell death. We then turned to using dyed or stained cells, with the hypothesis that a dye found within the cytoplasm would naturally get excreted into the EVs. However, dyes can be shed from cells, making it almost impossible to determine what fluorescent signal was from EVs and what came from free dye in the droplets. As such, we have landed on using GFP-cells to excrete GFP-EVs, which has recently been demonstrated by Joshi et al.[277]

GFP-K562 cells were used to determine whether this method would be feasible for EV detection in droplets. Initial experiments were performed by isolating K562-GFP EVs using ultracentrifugation. The EVs were then loaded into droplets and into an incubation chamber. Fluorescence was then imaged and quantified using the Nikon Ti2 Eclipse microscope and analysis software, **Figure 5-10**. As a comparison, fluorescent 190nm polystyrene beads (Bangs

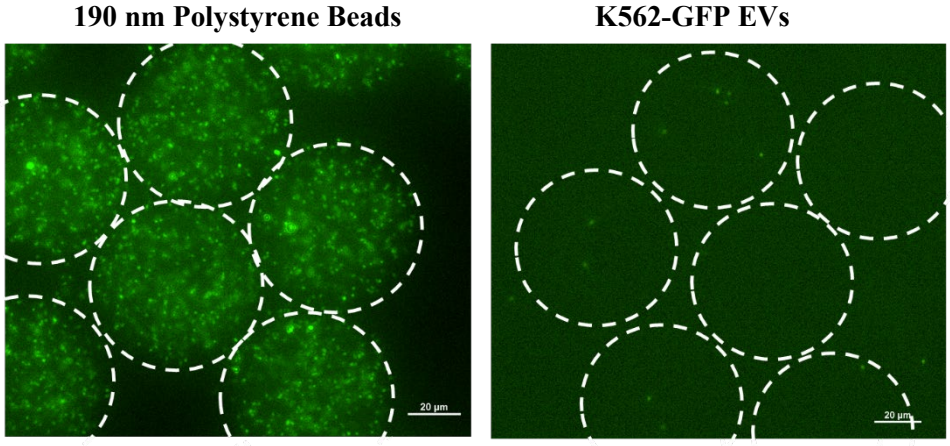

Figure 5-10 Comparison of 190nm polystyrene beads with GFP-EVs.

This comparison demonstrates the appearance of EV-sized fluorescent particles and confirm feasibility of the imaging method.

Lab), were processed into droplets, **Figure 5-10.** The comparison indicates the size range and appearance that the GFP-EVs should have, which we do see in the K562-GFP EVs.

5. 6 Discussion

In this work, we present the adaptation and application of the CellMag-CARWash droplet microfluidic device system for the isolation of pure NK-92MI cells. We then apply this device to begin understanding the heterogeneity of EV excretion among NK-92MI cells. The original CAR-Wash system was highly effective at separating magnetic beads with bound protein; however, the system had never been used to isolate live cells. We harnessed the CellMag-CARWash's ability to isolate magnetic beads and attached anti-CD56 magnetic Dynabeads™ to NK-92mi cells and isolated them from both pure and mixed cell populations.

Preliminary testing found that NK cells with 3 or more anti-CD56 Dynabeads attached were able to be captured by the CellMag-CARWash system with 85% ± 9 efficiency. Using bead and cellular velocities measured experimentally in the CellMag-CARWash device, we were able to calculate that the system should capture cells with ~1.8 beads attached, which is slightly different than our empirical finding that we needed 3 beads per cell for capture. This difference could be for several reasons. First, the calculations assume that the cell with beads attached is essentially just a magnetic sphere the size of a cell with a magnetism corresponding to the number of beads attach. This assumption does not consider the location of the beads on the cell: if all the beads are evenly spread out, this cell may have less pull towards the magnet as some of the beads are blocked by the cell. Additionally, the presence of many beads on the surface of a cell will increase the apparent size of the cell, further decreasing the measured linear velocity of a cell across the channel. Another potential cause is blockages in the device. Because we are processing cells, there is always going to be cellular debris. One of the benefits of the CellMag-

CARWash is the horizontal buffer exchange flow, however, cellular debris still occasionally becomes stuck to the device, causing cells to reroute to a suboptimal streamline, i.e. cells may be pushed away from the product stream along the bottom of the device.

Finally, for this system we used anti-CD56 conjugated Dynabeads, where CD56 is the hallmark protein marker for NK cells. However, it has been found that not all NK cell express CD56 at high level; Angelo et al. investigated NK cell phenotypes using flow cytometry and began by grouping NK cells into CD56 bright and CD56 dim.[278] In the future, we could consider adding a second NK cell antibody to our Dynabeads, such as CD49b or NKp46[279], allowing for bead attachment to cells that have lower expression of CD56.

We feel, however, that capturing only cells with 3+ beads may not be a problem, and in fact could even be beneficial. While we found very low nonspecific binding—in mixed cell populations T-cells rarely had beads attached, and if they did, it was always only one—the current system would allow these nonspecific cells to be released to the waste. Because of the high number of NK cells in the blood, accounting for ~10% of leukocytes in the blood, we are more concerned about the purity of the product sample and less about the recovery. In fact, we found that for mixed NK and T-cell populations, the purity of the product was 95%.

After validating the recovery of the system, we began investigating the stability of both the droplet and cells over 24 hours. We found that incubating droplets in an incubation device led to droplet destabilization and dissolvement whereas droplets stored in an Eppendorf tube remained stable and intact after 24 hours. Preliminary results show that after 24 hours, approximately 50% of the cells in droplets were dead while 45% were termed recently dead. This is a promising result, and we feel that with alterations to the droplet storage conditions, such as

storing them in a high concentration of gaseous CO_2, we could achieve high cell viability during the 24-hour incubation time.

This project is ongoing with several main thrusts needing work. First, we need to further investigate optical methods for quantifying EV production from the single cells. We found that GFP tagged cells excrete GFP EVs, however, quantifying the EVs per droplet poses an interesting challenge. We will additionally need to validate that attaching the magnet beads does not significantly alter the cells' ability to excrete EVs. Finally, we plan to use this system to profile the EVs from NK cells in the presence of various known NK activators, such as IL-12.

Chapter 6 Conclusions

6. 1 Research Summary

In this work I present the development of workflows for the isolation and characterization of biomarkers from stage III and stage IV non-small cell lung cancer patients. In NSCLC, it can be challenging to know what treatment will be the most effective for patients, with the standard of care being largely patient-independent. There is a critical need for technologies that can be used to predict treatment outcomes to ensure patients receive the most precise, personal therapies. Liquid biopsies offer the potential to fill this need, with two of the most common biomarkers being circulating tumor cells (CTCs) and extracellular vesicles (EVs). The pathway to develop a liquid biopsy requires isolation of a biomarker, characterization of that biomarker, correlating the biomarker to clinical data, and finally validation in a larger cohort.

In the second chapter of my thesis, I describe the development of workflows to isolate and analyze EVs using microfluidics. Several microfluidic technologies were introduced that take advantage of different isolation strategies to isolate EVs from human plasma. One of the main benefits of using EVs, as opposed to ctDNA or CTCs, is that they are incredibly durable while still allowing for multianalyte testing, which we take advantage of in these microfluidic devices. The first described device, the ^{new}ExoChip, uses the presentation of phosphatidylserine (PS) on the outer leaflet of tumor derived EVs (TDEVs) to capture TDEVs using Annexin V tethered to the device surface. This device steps outside of the bounds of typical EV capture, using a lipid as opposed to a tetraspanin protein as the target to capture EVs. We did have concerns, however, about the yield of this (and all) microfluidic device. Yield is incredibly

important in EV research because of the numerous characterizations that are needed to validate the presence of EVs. The ^{new}ExoChip was the first system where we developed and validated workflows to characterize EVs following on-chip isolation and release, with a heavy focus on protein assays. The presence of specific proteins is the hallmark to identify specific subpopulations of EVs or validate the presence of EVs from a specific source. In this first work, I optimized assays for CD9 and FLOT1 using output of the ^{new}ExoChip device, demonstrating the sufficient output of these technologies.

We took advantage of the newly developed EV-Protein workflows in the second work described, the "On-Chip Biogenesis of NK-EVs". In this system, we captured NK cells using the GO chip and incubated the captured, pure NK cells to generate NK-EVs which were then isolated using magnetic Dynabeads. In this system, I used western blots to demonstrate the presence of NK-EVs using CD56 (NK specific marker), FLOT1 and ALIX. This was significantly different than the proteins used for TDEVs, which contain the tetraspanin CD9, that is not expressed in NK cell derived EVs. In this work, the EVs were generated ex-vivo as opposed to direct capture, thereby testing our protein workflows again.

Finally, I presented the DICE device, to isolate and characterize EV protein on-chi. This device was slightly different, where we biotinylated all the EVs before attaching them to the device. We then characterized the captured EVs for four common proteins (EGFR, EPCAM, N-CAD, and PD-L1). The inter-person protein variability was corroborated using the Wes system, where quantified protein expression allows for easy comparison between samples. While these fundamental EV isolation and characterization methods are critical for EV research to move from benchtop to clinic, they are just the foundation and deeper characterizations are needed.

In my third chapter I did just that, we moved beyond fundamental EV characterizations to investigate whether EVs contained EGFR mutations and whether these could be correlated to clinical outcomes. The presence of EGFR mutations in metastatic lung cancer allows for the use of specific therapies, however, testing for these mutations in the primary tumor is highly invasive and therefore minimally repeatable. Additionally, it has been shown that mutation profiles of a tumor can change through therapy; developing resistance mutations frequently necessitates a change in treatment. Liquid biopsies are the optimal technology to solve the need for a highly repeatable EGFR mutation profiling technology. In the third chapter of my thesis, I demonstrated the presence of EGFR mutations in EVs, quantified the mutations, and correlated the mutation burden to disease status. First, I established the assays for both activating, L858R and exon 19 del, and resistance, T790M, mutations in EV-RNA using droplet digital PCR and activating mutations in EV-Protein using western blots. The assays had high specificity and sensitivity, as found using cell lines. The assays were then applied to a cohort of 10 metastatic NSCLC patients. EV-RNA mutations were found in 9/10 patients while EV-Protein was found in the four patients tested. Additionally, EV-RNA mutation burden, especially exon-19 deletion, was found to correlate to disease status; patients with increasing exon 19 del burden had progression and death, while patients with decreasing exon 19 del remained clinically stable. However, this was just a proof-of-concept study, demonstrating the potential of EVs for clinical use.

Compared to EVs, CTCs are significantly farther along in their path to clinical application. Because of the already FDA approved CellSearch™, their path to clinical utility is clearer and their use in clinical trials has already begun. CellSearch™ is not a perfect technology, and improvements are necessary, especially for investigating NSCLC CTCs which do not ubiquitously express the necessary EpCAM protein. In my fourth chapter, I present the use of the

GO Chip to isolate CTCs from treatment naïve stage III NSCLC patients. Here, CTCs were isolated from 26 NSCLC patients, before treatment, during radiation therapy, between therapies, and during immunotherapy. Two GO Chips were processed at each timepoint, with one being used to enumerate the number of CTCs per mL of blood and the second for microarray processing and differential gene analysis. The enumeration data allowed us to correlate the number of CTCs, change in number of CTCs, number of PD-L1+ CTCs and similar data to clinical metrics including gross tumor volume (GTV) and progression free survival (PFS). We found that between pre-treatment and week 4 of radiation having a percent change in CTCs therapy of less than 75% led to a significantly shorter PFS (7 mo. vs 21 mo. monitoring, $p = 0.0075$, log-rank (Mantel-Cox) test). We additionally found that the patients with progression while on anti-PD-L1 immunotherapy, durvalumab, had >50% PD-L1+ CTCs at all timepoints. Using survival analysis, we found that having >50% PD-L1+ CTCs at pre-treatment led to a shorter PFS, though not quite statistically significantly ($p < 0.06$, log-rank (Mantel-Cox) test).

While these metrics are incredibly exciting and offer the potential to screen patients either before treatment or very early during radiation therapy, we were additionally interested in the molecular profile of the CTCs. Previous GO Chip studies performed RT-qPCR to profile the CTC-RNA, however, in this study we moved to investigate whether a more comprehensive RNA profiling technique would be used. As such, we used the RNA isolated from the second GO chip to perform microarray analysis using ThermoFisher's Clariom S PICO chip. We used the R programming language to develop a code to process the data, from raw data through quality control (QC) and resulting in differential gene analysis. After comparing unpaired to paired analysis, we used a paired analysis to identify a list of >300 genes that were significantly differentially expressed between pre-treatment and week 4 of radiation based on $p < 0.05$ and

false discovery rate < 0.05 as determined using the empirical Bayesian method in either a paired or unpaired t-test. While our analysis is a critical addition to the journey to bring CTCs to clinical use, this is still a bulk analysis, and research has shown that cellular heterogeneity is critical to understand.

One area of research in which cellular heterogeneity is still poorly understood is EV biogenesis. In the fifth, and final, chapter of my thesis, I collaborated with the Bailey Lab to adapt their droplet microfluidic CellMag-CARWash system to isolate single, live cells. Droplet microfluidics are systems that use oil to generate aqueous droplets, allowing for manipulations and reactions on a micro- and pico- scale. In this work, we first processed cells through the microfluidic droplet generator before putting the single-cell droplets through the microfluidic CellMag-CARWash system. Positively tagged cells were encapsulated into fresh droplets in the product stream, leading to a pure cell population in droplets. In this work, we used NK-92MI cells to investigate the heterogeneity of EV generation among NK cells. After demonstrating the antitumoral response of NK-EVs ("On-Chip EV Biogenesis", Chapter 2), we aimed to understand the differences in EV generation. We found that the adapted CellMag-CARWash system isolates NK cells with 3+ anti-CD56 magnetic Dynabeads and using a previously developed mathematical framework to calculated that based on our system we should be able to capture cells with > 1.8 beads per cells. We then moved to demonstrate that the CAR-Was system isolates NK cells with 95% purity from a mix of NK and T-cells. Finally, because we are interested in using this system to investigate EV biogenesis, it was critical to demonstrate the droplet stability and cell viability after the CAR-Wash. We found that droplets need to be stored in solution as opposed to in a microfluidic device. However, while storing the droplets in an

Eppendorf tube led to droplet stability, there was minimal gas exchange which likely led to faster cell death.

6. 2 Limitations and Future Work

While the above work demonstrates the potential for introducing EVs and CTCs into clinical settings, there are still many challenges that need to be addressed before these biomarkers and subsequent technologies are adapted at a large scale.

EVs are definitively further away from clinical application, with no FDA approved isolation or characterization technologies being on the market. However, I feel that they offer more potential as prognostic and diagnostic biomarker in many cancers, especially lung cancer. The primary benefit of EVs is their robustness, their lipid bilayer makes them incredibly stable compared to other options. However, low concentration of target EVs in the background of non-specific EVs, i.e. tumor-derived EVs in white blood cell EVs, or NK-derived EVs in white blood cell EVs, is a monumental hurdle. The most common solution to isolate a specific subpopulation of EVs is to perform antibody-based capture using a marker that should be cell-type specific. This is essentially the principle we used in Chapter 2 designing the ^{new}ExoChip, however newer technologies, such as the ^{EV}HB-Chip screened several different glioblastoma specific markers to select the most effective for tumor-derived EV isolation, including EGFRvIII, one of the hallmarks proteins of glioblastoma.[145] While this is a reasonable solution to isolate cell-type specific EVs, each cancer or cell type would need to have its own antibody validated, which becomes not feasible when looking at using EVs for diagnostics, where the cancer type is unknown. Additionally, some patients may not express the specific marker of interest, for instance only 24%-67% of glioblastoma patients have the EGFRvIII mutation, so an EGFRvIII-specific test would be ineffective for those patients[280]. Similar advancements have led to the

generation of EV-protein screening assays to begin building knowledge about EV protein expression across cancers, however these efforts have been largely focused in lung cancer[93,94]. So while there has been much progress in finding tumor, or cell-type specific proteins, to target for EV isolation, there is still critical work that needs to be done before we have libraries of proteins to isolate or identify cancer type specific EVs.

A second option for a diagnostic or prognostic EV assay, besides isolating a tumor-derived EVs, would be to instead target a specific molecule found within EVs that is known to be generated from the tumor, such as tumor-specific mutations. This was the approach we took in Chapter 3, where we profiled EGFR mutations. While we found that our assay had high sensitivity and specificity with a potentially clinically interesting finding, the methods are not suitable for clinical use. First, the EV isolation method here was ultracentrifugation, which takes ~5 hours for EV isolation[46], and the machine would likely not even exist at a non-research hospital. Instead, an isolation method would need to be used that was either already commercially developed or could be easily commercialized. Current commercial isolation methods, such as PEG precipitation kits suffer from high cost and lower purity[47], while microfluidic technologies may not have a high enough yield to investigate rare mutations. Additionally, highly sensitive techniques are needed to profile these rare mutations if the isolated EVs are bulk EVs from blood. Droplet digital PCR, as used in Chapter 3, offers high sensitivity and the ability to achieve single-transcript resolution, but is minimally multiplexable, making it expensive and low throughput.[281] Therefore, the combination of ultracentrifugation followed by droplet digital PCR is unreasonable for a clinical setting, and both aspects of the workflow need improvements.

Where EVs are far from reaching clinical utility as diagnostic or prognostic technologies, CTCs are dramatically closer. The work in Chapter 4, using the GO chip to isolate CTCs across radiation therapy demonstrated prognostic potential early during treatment. There remain several challenges that need addressing before such a technology could be used in clinic. First, our findings were generated in a relatively small pilot cohort, a larger validation cohort is needed to ensure the accuracy of the data and power the study. However, the challenge in generating a larger cohort is additionally the second challenge for using this system in a clinical setting: fabricating and processing blood on a GO chip is a lengthy, hands on process.

Fabrication of the device is currently performed in 6 device batches, which would need to be significantly scaled up if used in a validation cohort. Of the two components of the device, the substrate is essentially a silicon wafer base with graphene oxide adhesion; this process is like other silicon fabrications used commercially and should be straightforward to scale up. The chamber is made of PDMS, which is an optimal material for this application[282], and would likely need to be purchased from a company to achieve the throughput needed. Finally, the functionalization of these devices is time intensive, and automation would be needed to truly scale up this process. However, this process does mimic other microchip platforms, and could be done commercially in theory.

Even once scale-up challenges are alleviated for GO Chip manufacturing to allow for large cohort processing, the downstream analyses of GO Chip workflows need automating. The results found in Chapter 4 were largely based on counting the number CTCs bound to the GO Chip as DAPI+/CK+/CD45- cells based on immunofluorescent staining. And while this enumeration was performed quantitatively based on fluorescent intensity, it was done manually, with each cell being measured and decided upon by a human, similar to pathological

identification of tissues. It has been shown that even among trained pathologists, human processing does added variability to these types of analyses.[283] Automated counting will be a critical addition to a clinical GO Chip workflow. Easily available software includes ImageJ and even potentially Nikon's proprietary NIS Elements software. However, these are still semi-manual, with the user needing to alter many settings. This can become very challenging when working with immunofluorescent CTCs, where fluorescent intensity can have high variability patient to patient. Machine learning techniques offer a more robust method for automated CTC counting, with several groups making significant headway in this effort, however researchers still note the need to be incredibly diligent when choosing algorithms and defining training sets because of the inherently noisy data created from cellular variability.[284,285]

Finally, one of the main challenges when working with both EVs and primary cells is their heterogeneity. In Chapter 5, I present an approach to use the droplet microfluidic CellMag-CARWash system to isolate NK cells into single-cell suspensions in droplets to investigate EV biogenesis. While this system offers many advantages for our application, there are several limitations to the setup. First, the system uses CD56 to bind magnetic beads to NK cells. However, if the goal is to investigate cellular heterogeneity, we have already preselected a population of NK cells that is likely to have a high expression of CD56; it has been shown that there are really two NK cell populations, $CD56^{bright}$ and $CD56^{dim}$ as shown by flow cytometry[286]. The creation of an NK cell-specific cocktail would enhance the variety of isolated NK cell phenotypes, and could include targets such as CD16 and NKp46.[287] Adding additional NK cell antibodies would also help reduce the number of NK cells with 0-1 beads attached, which accounted for ~20% of NK-92MI cells.

Besides increasing the heterogeneity of NK cells isolated, the post-CellMag-CARWash workflows face several limitations. First, the optical configuration of our EV-imaging is inherently challenging. Because of their small size, EVs are smaller than the wavelength of light, making their imaging extremely challenging. We are using fluorescence, which makes it possible, but imaging EVs is an on-going challenge in the field, especially when they are free to move about in a solution, causing them to be dilute and in many focus planes.[288] Typically, in droplet microfluidic systems, researchers either use fluorescent microscopes using either lasers (like confocal microscope) or LED light sources, or they insert optical fibers into the device to increase detection[289]. We feel that our Nikon Ti2 Eclipse microscope offers a sufficient combination of ease of use, low-background, and low-detection limit for this application as fluorescent microscopy has been used for single-cell cytokine detection[290], and instead need to think about the geometry of our incubation chamber and the image analysis of the gathered data. One challenge is removing the fluorescence of the cell from the droplet to only count the fluorescence of the EVs, this could be done using the cell counting software described above, likely ImageJ. We also need to worry about the EVs being on different focus planes: the current incubation chamber is 50μm tall. As such, we need to consider taking a z-stack, or scanning the droplets in the z-direction, in addition to the x- and y- coordinates of the device.

A second limitation is that the current scheme of using fluorescent imaging to quantify EVs will essentially only be useful to answer questions about EV generation because we do not add or remove anything from the droplets. The addition of more complex droplet manipulation devices downstream will open our system up to a wide array of applications. To give a couple of examples, many droplet microfluidic systems use picoinjectors, first ideated by the lab of David Weitz, to inject droplets with small amount of liquid.[291] Adding one or more picoinjectors to a

system vastly increases the applications of the system, with groups using picoinjectors to add reporter molecules to monitor reactions or the accumulation of secreted products.[292] Another option to increase the versatility of this system would be to include a K-Channel, whereby droplets are split into two smaller droplets[293], therefore the introduction of a magnet in one product stream would allow us to remove the tagged-cells, leaving droplets filled with only EVs for further analysis.

6. 3 Conclusions

In this work, I present several projects aiming to push the use of a blood-based liquid biopsy in lung cancer forward. From the development of EV isolation technologies and fundamental assays for EV characterization to the detection of EGFR mutations in EVs, this work helps move EVs towards clinical application. Then moving to CTCs, I demonstrate a direct clinical application of CTCs in stage III NSCLC, where changes in the number of CTCs predicts patient outcomes, but the technology would need to be overhauled for commercial scale-up to be reasonable. Finally, I introduce a droplet microfluidic technology to isolate pure cell populations using immunoaffinity magnet binding and am working to apply the technology to understand the heterogeneity of NK cell EV biogenesis.

Bibliography

1. American Cancer Society. Lung Cancer Survival Rates. (2021).

2. Network, N. C. C. *National Comprehensive Cancer Network Clinical practice in Oncology (NCCN Guidelines): Non-small cell lung cancer, Version 3*. (2020).

3. Herbst, R. S. *et al.* Pembrolizumab versus docetaxel for previously treated, PD-L1-positive, advanced non-small-cell lung cancer (KEYNOTE-010): A randomised controlled trial. *Lancet* **387**, 1540–1550 (2016).

4. Iwai, Y. *et al.* Involvement of PD-L1 on tumor cells in the escape from host immune system and tumor immunotherapy by PD-L1 blockade. *Proc. Natl. Acad. Sci.* **99**, 12293–12297 (2002).

5. Antonia, S. J. *et al.* Durvalumab after chemoradiotherapy in stage III non–small-cell lung cancer. *N. Engl. J. Med.* **377**, 1919–1929 (2017).

6. Rosell, R. *et al.* Erlotinib versus standard chemotherapy as first-line treatment for European patients with advanced EGFR mutation-positive non-small-cell lung cancer (EURTAC): A multicentre, open-label, randomised phase 3 trial. *Lancet Oncol.* **13**, 239–246 (2012).

7. Pao, W. *et al.* Acquired resistance of lung adenocarcinomas to gefitinib or erlotinib is associated with a second mutation in the EGFR kinase domain. *PLoS Med.* **2**, 0225–0235 (2005).

8. Balak, M. N. *et al.* Novel D761Y and common secondary T790M mutations in epidermal growth factor receptor-mutant lung adenocarcinomas with acquired resistance to kinase inhibitors. *Clin. Cancer Res.* **12**, 6494–6501 (2006).

9. Clark, J., Cools, J. & Gilliland, D. G. EGFR inhibition in non-small cell lung cancer: Resistance, once again, rears its ugly head. *PLoS Med.* **2**, 0195–0197 (2005).

10. Patel, H., Pawara, R., Ansari, A. & Surana, S. Recent updates on third generation EGFR inhibitors and emergence of fourth generation EGFR inhibitors to combat C797S resistance. *Eur. J. Med. Chem.* **142**, 32–47 (2017).

11. Alix-Panabieѐres, C. & Pantel, K. Circulating tumor cells: Liquid biopsy of cancer. *Clin. Chem.* **59**, 110–118 (2013).

12. Diaz, L. A. & Bardelli, A. Liquid biopsies: Genotyping circulating tumor DNA. *J. Clin. Oncol.* **32**, 579–586 (2014).

13. Yoshioka, Y. *et al.* Ultra-sensitive liquid biopsy of circulating extracellular vesicles using ExoScreen. *Nat. Commun.* **5**, 3591 (2014).

14. Thierry, A. R., El Messaoudi, S., Gahan, P. B., Anker, P. & Stroun, M. Origins, structures, and functions of circulating DNA in oncology. *Cancer Metastasis Rev.* **35**, 347–376 (2016).

15. Vasioukhin, V. *et al.* Point mutations of the N-ras gene in the blood plasma DNA of patients with myelodysplastic syndrome or acute myelogenous leukaemia. *Br. J. Haematol.* **86**, 774–779 (1994).

16. Mouliere, F. *et al.* High fragmentation characterizes tumour-derived circulating DNA. *PLoS One* **6**, e23418 (2011).

17. Diehl, F. *et al.* Detection and quantification of mutations in the plasma of patients with colorectal tumors. *Proc. Natl. Acad. Sci. U. S. A.* **102**, 16368–16373 (2005).

18. Théry, C., Zitvogel, L. & Amigorena, S. Exosomes: composition, biogenesis and function. *Nat. Rev. Immunol.* **2**, 569–579 (2002).

19. Théry, C. *et al.* Minimal information for studies of extracellular vesicles 2018 (MISEV2018): a position statement of the International Society for Extracellular Vesicles and update of the MISEV2014 guidelines. *J. Extracell. Vesicles* (2018) doi:10.1080/20013078.2018.1535750.

20. Théry, C. Exosomes: secreted vesicles and intercellular communications. *F1000 Biol. Rep.* **3**, 1–8 (2011).

21. Simons, M. & Raposo, G. Exosomes--vesicular carriers for intercellular communication. *Curr. Opin. Cell Biol.* **21**, 575–581 (2009).

22. Tkach, M. & Théry, C. Communication by Extracellular Vesicles: Where We Are and Where We Need to Go. *Cell* **164**, 1226–1232 (2016).

23. Liu, C. *et al.* Murine Mammary Carcinoma Exosomes Promote Tumor Growth by Suppression of NK Cell Function. *J. Immunol.* **176**, 1375–1385 (2006).

24. Abusamra, A. J. *et al.* Tumor exosomes expressing Fas ligand mediate CD8+ T-cell apoptosis. *Blood Cells, Mol. Dis.* **35**, 169–173 (2005).

25. Costa-Silva, B. *et al.* Pancreatic cancer exosomes initiate pre-metastatic niche formation in the liver. *Nat Cell Biol* **17**, 816–826 (2015).

26. Bellavia, D. *et al.* Interleukin 3-receptor targeted exosomes inhibit in vitro and in vivo Chronic Myelogenous Leukemia cell growth. *Theranostics* **7**, 1333 (2017).

27. Srivastava, A. *et al.* Nanosomes carrying doxorubicin exhibit potent anticancer activity against human lung cancer cells. *Sci. Rep.* **6**, 38541 (2016).

28. Liu, J. *et al.* Functional extracellular vesicles engineered with lipid-grafted hyaluronic acid effectively reverse cancer drug resistance. *Biomaterials* **223**, 119475 (2019).

29. Shtam, T. A. *et al.* Exosomes are natural carriers of exogenous siRNA to human cells in vitro. *Cell Commun. Signal.* **11**, 1–10 (2013).

30. Kim, S. M. *et al.* Cancer-derived exosomes as a delivery platform of CRISPR/Cas9 confer cancer cell tropism-dependent targeting. *J. Control. Release* **266**, 8–16 (2017).

31. Alvarez-Erviti, L. *et al.* Delivery of siRNA to the mouse brain by systemic injection of targeted exosomes. *Nat. Biotechnol.* **29**, 341–345 (2011).

32. Kim, H. *et al.* Cardiac-specific delivery by cardiac tissue-targeting peptide-expressing exosomes. *Biochem. Biophys. Res. Commun.* **499**, 803–808 (2018).

33. Ohno, S. I. *et al.* Systemically injected exosomes targeted to EGFR deliver antitumor microrna to breast cancer cells. *Mol. Ther.* **21**, 185–191 (2013).

34. Liang, G. *et al.* Engineered exosomes for targeted co-delivery of miR-21 inhibitor and chemotherapeutics to reverse drug resistance in colon cancer. *J. Nanobiotechnology* **18**, 1–15 (2020).

35. Yang, C., Zhang, M. & Merlin, D. Advances in plant-derived edible nanoparticle-based lipid nano-drug delivery systems as therapeutic nanomedicines. *J. Mater. Chem. B* **6**, 1312–1321 (2018).

36. Iravani, S. & Varma, R. S. Plant-Derived Edible Nanoparticles and miRNAs: Emerging Frontier for Therapeutics and Targeted Drug-Delivery. *ACS Sustain. Chem. Eng.* **7**, 8055–8069 (2019).

37. Wang, Q. *et al.* Grapefruit-derived nanovectors use an activated leukocyte trafficking pathway to deliver therapeutic agents to inflammatory tumor sites. *Cancer Res.* **75**, 2520–2529 (2015).

38. Si, Y. *et al.* Targeted Exosomes for Drug Delivery: Biomanufacturing, Surface Tagging, and Validation. *Biotechnol. J.* **15**, 1900163 (2020).

39. Hessvik, N. P. & Llorente, A. Current knowledge on exosome biogenesis and release. *Cell. Mol. Life Sci.* **75**, 193–208 (2018).

40. Rabinowits, G., Gerçel-Taylor, C., Day, J. M., Taylor, D. D. & Kloecker, G. H. Exosomal microRNA: a diagnostic marker for lung cancer. *Clin. Lung Cancer* **10**, 42–6 (2009).

41. Hanahan, D. & Weinberg, R. A. Review Hallmarks of Cancer : The Next Generation. *Cell* **144**, 646–674 (2011).

42. Cristofanilli, M. *et al.* Circulating tumor cells, disease progression, and survival in metastatic breast cancer. *... Engl. J. ...* **351**, 781–791 (2004).

43. De Bono, J. S. *et al.* Circulating tumor cells predict survival benefit from treatment in metastatic castration-resistant prostate cancer. *Clin. Cancer Res.* **14**, 6302–6309 (2008).

44. Cohen, S. J. *et al.* Relationship of circulating tumor cells to tumor response, progression-free survival, and overall survival in patients with metastatic colorectal cancer. *J. Clin. Oncol.* **26**, 3213–3221 (2008).

45. Krebs, M. G. *et al.* Evaluation and prognostic significance of circulating tumor cells in patients with non-small-cell lung cancer. *J. Clin. Oncol.* **29**, 1556–1563 (2011).

46. Thery, C., Amigorena, S., Raposo, G. & Clayton, A. Isolation and characterization of exosomes from cell culture supernatants and biological fluids. *Curr. Protoc. cell Biol.* **Chapter 3**, Unit 3.22 (2006).

47. Van Deun, J. *et al.* The impact of disparate isolation methods for extracellular vesicles on downstream RNA profiling. *J. Extracell. Vesicles* **3**, (2014).

48. Lobb, R. J. *et al.* Optimized exosome isolation protocol for cell culture supernatant and human plasma. *J. Extracell. Vesicles* (2015) doi:10.3402/jev.v4.27031.

49. Zhou, M., Weber, S. R., Zhao, Y., Chen, H. & Sundstrom, J. M. Chapter 2 - Methods for exosome isolation and characterization. in (eds. Edelstein, L., Smythies, J., Quesenberry, P. & Noble, D. B. T.-E.) 23–38 (Academic Press, 2020). doi:https://doi.org/10.1016/B978-0-12-816053-4.00002-X.

50. Lane, R. E., Korbie, D., Trau, M. & Hill, M. M. Optimizing Size Exclusion Chromatography for Extracellular Vesicle Enrichment and Proteomic Analysis from Clinically Relevant Samples. *Proteomics* **19**, e1800156 (2019).

51. Soares Martins, T., Catita, J., Martins Rosa, I., A B da Cruz E Silva, O. & Henriques, A. G. Exosome isolation from distinct biofluids using precipitation and column-based approaches. *PLoS One* **13**, e0198820–e0198820 (2018).

52. Tang, Y. *et al.* Comparison of isolation methods of exosomes and exosomal RNA from cell culture medium and serum. 834–844 (2017) doi:10.3892/ijmm.2017.3080.

53. Wu, X. *et al.* Exosome-templated nanoplasmonics for multiparametric molecular profiling. *Sci. Adv.* **6**, eaba2556 (2020).

54. Liu, C. *et al.* Single-Exosome-Counting Immunoassays for Cancer Diagnostics. *Nano Lett.* **18**, 4226–4232 (2018).

55. Hisey, C. L., Dorayappan, K. D. P., Cohn, D. E., Selvendiran, K. & Hansford, D. J. Microfluidic affinity separation chip for selective capture and release of label-free ovarian cancer exosomes. *Lab Chip* **18**, 3144–3153 (2018).

56. Chen, W., Li, H., Su, W. & Qin, J. Microfluidic device for on-chip isolation and detection of circulating exosomes in blood of breast cancer patients. *Biomicrofluidics* **13**, 54113

(2019).

57. Dorayappan, K. D. P. *et al.* A Microfluidic Chip Enables Isolation of Exosomes and Establishment of Their Protein Profiles and Associated Signaling Pathways in Ovarian Cancer. *Cancer Res.* **79**, 3503–3513 (2019).

58. Dudani, J. S. *et al.* Rapid inertial solution exchange for enrichment and flow cytometric detection of microvesicles. *Biomicrofluidics* **9**, 1–9 (2015).

59. Xu, H., Liao, C., Zuo, P., Liu, Z. & Ye, B.-C. Magnetic-Based Microfluidic Device for On-Chip Isolation and Detection of Tumor-Derived Exosomes. *Anal. Chem.* **90**, 13451–13458 (2018).

60. Kanwar, S. S., Dunlay, C. J., Simeone, D. M. & Nagrath, S. Microfluidic device (ExoChip) for on-chip isolation, quantification and characterization of circulating exosomes. *Lab Chip* **14**, 1891–1900 (2014).

61. Lo, T. *et al.* Microfluidic device for high-throughput affinity-based isolation of extracellular vesicles. *Lab Chip* (2020) doi:10.1039/c9lc01190k.

62. Zhang, P. *et al.* Ultrasensitive detection of circulating exosomes with a 3D-nanopatterned microfluidic chip. *Nat. Biomed. Eng.* **3**, 438–451 (2019).

63. Kang, Y.-T. *et al.* Isolation and Profiling of Circulating Tumor-Associated Exosomes Using Extracellular Vesicular Lipid-Protein Binding Affinity Based Microfluidic Device. *Small* **15**, e1903600 (2019).

64. Zhang, P., Zhou, X. & Zeng, Y. Multiplexed immunophenotyping of circulating exosomes on nano-engineered ExoProfile chip towards early diagnosis of cancer. *Chem. Sci.* **10**, 5495–5504 (2019).

65. Raposo, G. & Stoorvogel, W. Extracellular vesicles: Exosomes, microvesicles, and friends. *J. Cell Biol.* **200**, 373–383 (2013).

66. Lötvall, J. *et al.* Minimal experimental requirements for definition of extracellular vesicles and their functions: A position statement from the International Society for Extracellular Vesicles. *J. Extracell. Vesicles* **3**, (2014).

67. Sharma, S. *et al.* Structural-mechanical characterization of nanoparticle exosomes in human saliva, using correlative AFM, FESEM, and force spectroscopy. *ACS Nano* **4**, 1921–1926 (2010).

68. Wu, Y., Deng, W. & Klinke, D. J. Exosomes: improved methods to characterize their morphology, RNA content, and surface protein biomarkers. *Analyst* **140**, 6631–42 (2015).

69. Hartjes, T. A., Mytnyk, S., Jenster, G. W., van Steijn, V. & van Royen, M. E. Extracellular Vesicle Quantification and Characterization: Common Methods and Emerging Approaches. *Bioeng. (Basel, Switzerland)* **6**, (2019).

70. Bachurski, D. *et al.* Extracellular vesicle measurements with nanoparticle tracking analysis–An accuracy and repeatability comparison between NanoSight NS300 and ZetaView. *J. Extracell. Vesicles* **8**, (2019).

71. Okoye, I. S. *et al.* MicroRNA-containing T-regulatory-cell-derived exosomes suppress pathogenic T helper 1 cells. *Immunity* **41**, 89–103 (2014).

72. Hou, Y. *et al.* Exosome-related lncRNAs as predictors of HCC patient survival: A prognostic model. *Am. J. Transl. Res.* **10**, 1648–1662 (2018).

73. Thakur, B. K. *et al.* Double-stranded DNA in exosomes: A novel biomarker in cancer detection. *Cell Res.* **24**, 766–769 (2014).

74. Demory Beckler, M. *et al.* Proteomic Analysis of Exosomes from Mutant KRAS Colon Cancer Cells Identifies Intercellular Transfer of Mutant KRAS. *Mol. Cell. Proteomics* **12**, 343–355 (2013).

75. Gerlach, J. Q. & Griffin, M. D. Getting to know the extracellular vesicle glycome. *Mol. BioSyst.* **12**, 1071–1081 (2016).

76. Zebrowska, A., Skowronek, A., Wojakowska, A., Widlak, P. & Pietrowska, M. Metabolome of exosomes: Focus on vesicles released by cancer cells and present in human body fluids. *Int. J. Mol. Sci.* **20**, (2019).

77. Lo, T.-W. *et al.* Microfluidic Device for High-Throughput Affinity-based Isolation of Extracellular Vesicles. *Lab Chip* (2020) doi:10.1039/c9lc01190k.

78. Tauro, B. J. *et al.* Comparison of ultracentrifugation, density gradient separation, and immunoaffinity capture methods for isolating human colon cancer cell line LIM1863-derived exosomes. *Methods* **56**, 293–304 (2012).

79. J.P.J.J., H. *et al.* Proteomic Analysis of Exosomes Secreted by Human Mesothelioma Cells. *Am. J. Pathol.* **164**, 1807–1815 (2004).

80. Lin, S. Y. *et al.* Proteome profiling of urinary exosomes identifies alpha 1-antitrypsin and H2B1K as diagnostic and prognostic biomarkers for urothelial carcinoma. *Sci. Rep.* **6**, 1–12 (2016).

81. Vlassov, A. V., Magdaleno, S., Setterquist, R. & Conrad, R. Exosomes: Current knowledge of their composition, biological functions, and diagnostic and therapeutic potentials. *Biochim. Biophys. Acta - Gen. Subj.* **1820**, 940–948 (2012).

82. Kang, Q. *et al.* Comparative analysis of circulating tumor DNA stability In K3EDTA, Streck, and CellSave blood collection tubes. *Clin. Biochem.* **49**, 1354–1360 (2016).

83. Jin, Y. *et al.* DNA in serum extracellular vesicles is stable under different storage conditions. *BMC Cancer* **16**, 1–9 (2016).

84. Liu, Q. *et al.* Circulating exosomal microRNAs as prognostic biomarkers for non-small-cell lung cancer. *Oncotarget* **8**, 13048–13058 (2017).

85. Xue, X., Zhao, Y., Wang, X., Qin, L. & Hu, R. Development and validation of serum exosomal microRNAs as diagnostic and prognostic biomarkers for hepatocellular carcinoma. *J. Cell. Biochem.* **120**, 135–142 (2019).

86. Lee, Y. R. *et al.* Circulating exosomal noncoding RNAs as prognostic biomarkers in human hepatocellular carcinoma. *Int. J. Cancer* **144**, 1444–1452 (2019).

87. Peng, Z. Y., Gu, R. H. & Yan, B. Downregulation of exosome-encapsulated miR-548c-5p is associated with poor prognosis in colorectal cancer. *J. Cell. Biochem.* **120**, 1457–1463 (2019).

88. Fengming, L. A. N., Xiao, Y. U. E. & Tingyi, X. I. A. Exosomal microRNA–210 is a potentially non–invasive biomarker for the diagnosis and prognosis of glioma. *Oncol. Lett.* **19**, 1967–1974 (2020).

89. Foj, L. *et al.* Exosomal and Non-Exosomal Urinary miRNAs in Prostate Cancer Detection and Prognosis. *Prostate* **77**, 573–583 (2017).

90. Jin, X. *et al.* Evaluation of tumor-derived exosomal miRNA as potential diagnostic biomarkers for early-stage non-small cell lung cancer using next-generation sequencing. *Clin. Cancer Res.* **23**, 5311–5319 (2017).

91. Lux, A., Kahlert, C., Grützmann, R. & Pilarsky, C. c-Met and PD-l1 on circulating exosomes as diagnostic and prognostic markers for pancreatic cancer. *Int. J. Mol. Sci.* **20**, 1–12 (2019).

92. Manda, S. V. *et al.* Exosomes as a biomarker platform for detecting epidermal growth factor receptor-positive high-grade gliomas. *J. Neurosurg.* **128**, 1091–1101 (2018).

93. Sandfeld-Paulsen, B. *et al.* Exosomal proteins as prognostic biomarkers in non-small cell lung cancer. *Mol. Oncol.* **10**, 1234 (2016).

94. Sandfeld-Paulsen, B. *et al.* Exosomal proteins as diagnostic biomarkers in lung cancer. *J. Thorac. Oncol.* **11**, 1701–1710 (2016).

95. Wang, X. *et al.* Exosomal protein CD82 as a diagnostic biomarker for precision medicine for breast cancer. *Mol. Carcinog.* **58**, 674–685 (2019).

96. Melo, S. A. *et al.* Glypican-1 identifies cancer exosomes and detects early pancreatic cancer. *Nature* **523**, 177–182 (2015).

97. Jakobsen, K. R. *et al.* Exosomal proteins as potential diagnostic markers in advanced non-small cell lung carcinoma. *J Extracell Vesicles* **4**, 26659 (2015).

98. Leo W. Jenkins Cancer Center. A Pilot Study of Tumor-Derived Exosomes as Diagnostic

and Prognostic Markers in Breast Cancer Patients Receiving Neoadjuvant Chemotherapy. (2017).

99. Yuwen, D. *et al.* Prognostic role of circulating exosomal miR-425-3p for the response of NSCLC to platinum-based chemotherapy. *Cancer Epidemiol. Biomarkers Prev.* **28**, 163–173 (2019).

100. Jin, G. *et al.* A panel of serum exosomal microRNAs as predictive markers for chemoresistance in advanced colorectal cancer. *Cancer Chemother. Pharmacol.* **84**, 315–325 (2019).

101. Del Re, M. *et al.* PD-L1 mRNA expression in plasma-derived exosomes is associated with response to anti-PD-1 antibodies in melanoma and NSCLC. *Br. J. Cancer* **118**, 820–824 (2018).

102. Zhang, L. *et al.* Meta-analysis of the prognostic value of circulating tumor cells in breast cancer. *Clin. Cancer Res.* **18**, 5701–5710 (2012).

103. Miller, M. C., Doyle, G. V & Terstappen, L. W. M. M. Significance of Circulating Tumor Cells Detected by the CellSearch System in Patients with Metastatic Breast Colorectal and Prostate Cancer. *J. Oncol.* **2010**, (2010).

104. Okumura, Y. *et al.* Circulating Tumor Cells in Pulmonary Venous Blood of Primary Lung Cancer Patients. *Ann. Thorac. Surg.* **87**, 1669–1675 (2009).

105. Tamminga, M. *et al.* Circulating tumor cells in advanced non-small cell lung cancer patients are associated with worse tumor response to checkpoint inhibitors. *J. Immunother. Cancer* **7**, (2019).

106. Hanssen, A. *et al.* Characterization of different CTC subpopulations in non-small cell lung cancer. *Sci. Rep.* **6**, 1–9 (2016).

107. Alix-Panabières, C. & Pantel, K. *Challenges in circulating tumour cell research*. *Nature Reviews Cancer* vol. 14 www.nature.com/reviews/cancer (2014).

108. Lin, E. *et al.* High-Throughput Microfluidic Labyrinth for the Label-free Isolation of Circulating Tumor Cells. *Cell Syst.* **5**, 295-304.e4 (2017).

109. Zeinali, M. *et al.* High-throughput label-free isolation of heterogeneous circulating tumor cells and CTC clusters from non-small-cell lung cancer patients. *Cancers (Basel).* **12**, 1–17 (2020).

110. Sollier, E. *et al.* Size-selective collection of circulating tumor cells using Vortex technology. *Lab Chip* **14**, 63–77 (2014).

111. Lin, H. K. *et al.* Portable filter-based microdevice for detection and characterization of circulating tumor cells. *Clin. Cancer Res.* **16**, 5011–5018 (2010).

112. Sequist, L. V., Nagrath, S., Toner, M., Haber, D. A. & Lynch, T. J. The CTC-Chip: An Exciting New Tool to Detect Circulating Tumor Cells in Lung Cancer Patients. *J. Thorac. Oncol.* **4**, 281–283 (2009).

113. Allard, W. J. *et al.* Tumor Cells Circulate in the Peripheral Blood of All Major Carcinomas but not in Healthy Subjects or Patients With Nonmalignant Diseases Tumor Cells Circulate in the Peripheral Blood of All Major Carcinomas but not in Healthy Subjects or Patients With Non. *Clin. Cancer Res.* **10**, 6897–6904 (2005).

114. Stott, S. L. *et al.* Isolation of circulating tumor cells using a microvortex-generating herringbone-chip. *October* **107**, 18392–7 (2010).

115. Murlidhar, V. *et al.* Poor Prognosis Indicated by Venous Circulating Tumor Cell Clusters in Early Stage Lung Cancers. *Cancer Res.* **77**, canres.2072.2016 (2017).

116. Talasaz, A. H. *et al.* Isolating highly enriched populations of circulating epithelial cells and other rare cells from blood using a magnetic sweeper device. *Proc. Natl. Acad. Sci. U. S. A.* **106**, 3970–3975 (2009).

117. Fachin, F. *et al.* Monolithic Chip for High-throughput Blood Cell Depletion to Sort Rare Circulating Tumor Cells. *Sci. Rep.* **7**, 1–11 (2017).

118. Yoon, H. J. *et al.* Sensitive capture of circulating tumour cells by functionalized graphene oxide nanosheets. *Nat Nano* **8**, 735–741 (2013).

119. Wang, Y. *et al.* PD-L1 Expression in Circulating Tumor Cells Increases during Radio (chemo) therapy and Indicates Poor Prognosis in Lung Cancer. **1**, 1–25.

120. Day, K. C. *et al.* HER2 and EGFR overexpression support metastatic progression of prostate cancer to bone. *Cancer Res.* **77**, 74–85 (2017).

121. Yoon, H. J. *et al.* Tunable Thermal-Sensitive Polymer–Graphene Oxide Composite for Efficient Capture and Release of Viable Circulating Tumor Cells. *Adv. Mater.* 4891–4897 (2016) doi:10.1002/adma.201600658.

122. Kozminsky, M. *et al.* Detection of CTC Clusters and a Dedifferentiated RNA- Expression Survival Signature in Prostate Cancer. (2018) doi:10.1002/advs.201801254.

123. Kim, T. H. *et al.* Characterizing Circulating Tumor Cells Isolated from Metastatic Breast Cancer Patients Using Graphene Oxide Based Microfluidic Assay. *Adv. Biosyst.* **3**, 1800278 (2019).

124. Nagrath, S. *et al.* Isolation of rare circulating tumour cells in cancer patients by microchip technology. *Nature* **450**, 1235–1239 (2007).

125. Maheswaran, S. *et al.* Detection of Mutations in EGFR in Circulating Lung-Cancer Cells. *N. Engl. J. Med.* **359**, 366–377 (2008).

126. Hayes, D. C. *et al.* Multigene real-time PCR detection of circulating tumor cells in peripheral blood of lung cancer patients. *Anticancer Res.* **26**, 1567–1575 (2006).

127. Chen, T. F. *et al.* CK19 mRNA expression measured by reverse-transcription polymerase chain reaction (RT-PCR) in the peripheral blood of patients with non-small cell lung cancer treated by chemo-radiation: An independent prognostic factor. *Lung Cancer* **56**, 105–114 (2007).

128. Sher, Y.-P. *et al.* Prognosis of non-small cell lung cancer patients by detecting circulating cancer cells in the peripheral blood with multiple marker genes. *Clin. Cancer Res.* **11**, 173–179 (2005).

129. Shyamala, M. *et al.* Detection of Mutations in EGFR in Circulating Lung-Cancer Cells. *N. Engl. J. Med.* **359**, 366–377 (2008).

130. Ilie, M. *et al.* ALK-gene rearrangement: A comparative analysis on circulating tumour cells and tumour tissue from patients with lung adenocarcinoma. *Ann. Oncol.* **23**, 2907–2913 (2012).

131. Tang, Y. T. *et al.* Comparison of isolation methods of exosomes and exosomal RNA from cell culture medium and serum. *Int. J. Mol. Med.* **40**, 834–844 (2017).

132. Théry, C., Amigorena, S., Raposo, G. & Clayton, A. Isolation and Characterization of Exosomes from Cell Culture Supernatants. *Curr. Protoc. Cell Biol.* **Chapter 3**, 1–29 (2006).

133. Zhang, P. *et al.* Ultrasensitive detection of circulating exosomes with a 3D-nanopatterned microfluidic chip. *Nat. Biomed. Eng.* **3**, 438–451 (2019).

134. Wang, J. *et al.* Chemically Edited Exosomes with Dual Ligand Purified by Microfluidic Device for Active Targeted Drug Delivery to Tumor Cells. *ACS Appl. Mater. Interfaces* **9**, 27441–27452 (2017).

135. He, M., Crow, J., Roth, M., Zeng, Y. & Godwin, A. K. Integrated immunoisolation and protein analysis of circulating exosomes using microfluidic technology. *Lab Chip* **14**, 3773–3780 (2014).

136. Im, H. *et al.* Label-free detection and molecular profiling of exosomes with a nano-plasmonic sensor. *Nat. Biotechnol.* **32**, 490–495 (2014).

137. Kwizera, E. A. *et al.* Molecular detection and analysis of exosomes using surface-enhanced Raman scattering gold nanorods and a miniaturized device. *Theranostics* **8**, 2722–2738 (2018).

138. Kang, Y. T. *et al.* High-purity capture and release of circulating exosomes using an exosome-specific dual-patterned immunofiltration (ExoDIF) device. *Nanoscale* **9**, 13495–13505 (2017).

139. Im, H. *et al.* Label-free detection and molecular profiling of exosomes with a nano-plasmonic sensor. *Nat. Biotechnol.* **32**, 490–495 (2014).

140. Qi, R. *et al.* Microfluidic device for the analysis of MDR cancerous cell-derived exosomes' response to nanotherapy. *Biomed. Microdevices* **21**, 35 (2019).

141. Fang, S. *et al.* Clinical application of a microfluidic chip for immunocapture and quantification of circulating exosomes to assist breast cancer diagnosis and molecular classification. *PLoS One* **12**, (2017).

142. Chen, C. *et al.* Microfluidic isolation and transcriptome analysis of serum microvesicles. *Lab Chip* **10**, 505–511 (2010).

143. Lee, K. *et al.* Multiplexed Profiling of Single Extracellular Vesicles. *ACS Nano* acsnano.7b07060 (2018) doi:10.1021/acsnano.7b07060.

144. Sandfeld-Paulsen, B. *et al.* Exosomal proteins as prognostic biomarkers in non-small cell lung cancer. *Mol. Oncol.* **10**, 1595 (2016).

145. Reátegui, E. *et al.* Engineered nanointerfaces for microfluidic isolation and molecular profiling of tumor-specific extracellular vesicles. doi:10.1038/s41467-017-02261-1.

146. An, T. *et al.* Exosomes serve as tumour markers for personalized diagnostics owing to their important role in cancer metastasis. doi:10.3402/jev.v4.27522.

147. Sina, A. A. I. *et al.* Real time and label free profiling of clinically relevant exosomes. *Sci. Rep.* **6**, 30460 (2016).

148. Théry, C., Clayton, A., Amigorena, S., Raposo, G. & Clayton, A. Isolation and Characterization of Exosomes from Cell Culture Supernatants. *Curr. Protoc. Cell Biol.* **Chapter 3**, 1–29 (2006).

149. He, M., Crow, J., Roth, M., Zeng, Y. & Godwin, A. K. Integrated immunoisolation and protein analysis of circulating exosomes using microfluidic technology. *Lab Chip* **14**, 3773–3780 (2014).

150. Sharma, P. *et al.* Immunoaffinity-based isolation of melanoma cell-derived exosomes from plasma of patients with melanoma. *J. Extracell. Vesicles* **7**, 1435138 (2018).

151. Koga, K. *et al.* Purification, characterization and biological significance of tumor-derived exosomes. *Anticancer Res.* **25**, 3703–3707 (2005).

152. Clayton, A. *et al.* Analysis of antigen presenting cell derived exosomes, based on immuno-magnetic isolation and flow cytometry. *J. Immunol. Methods* **247**, 163–174 (2001).

153. Shtam, T. A. *et al.* Exosomes are natural carriers of exogenous siRNA to human cells in vitro. *Cell Commun. Signal.* **11**, 1–10 (2013).

154. Long, L. *et al.* Tissue-specific and exosomal miRNAs in lung cancer radiotherapy: From regulatory mechanisms to clinical implications. *Cancer Manag. Res.* **11**, 4413–4424 (2019).

155. Munich, S., Sobo-Vujanovic, A., Buchser, W. J., Beer-Stolz, D. & Vujanovic, N. L. Dendritic cell exosomes directly kill tumor cells and activate natural killer cells via TNF superfamily ligands. *Oncoimmunology* **1**, 1074–1083 (2012).

156. Wu, C. H. *et al.* Extracellular vesicles derived from natural killer cells use multiple cytotoxic proteins and killing mechanisms to target cancer cells. *J. Extracell. Vesicles* **8**, (2019).

157. Kang, Y. T. *et al.* On-Chip Biogenesis of Circulating NK Cell-Derived Exosomes in Non-Small Cell Lung Cancer Exhibits Antitumoral Activity. *Adv. Sci.* **8**, (2021).

158. Oosthuyzen, W. *et al.* Quantification of human urinary exosomes by nanoparticle tracking analysis. *J. Physiol.* **591**, 5833–5842 (2013).

159. Eldh, M. *et al. MicroRNA in exosomes isolated directly from the liver circulation in patients with metastatic uveal melanoma*. *BMC Cancer* vol. 14 http://www.biomedcentral.com/1471-2407/14/962 (2014).

160. Logozzi, M. *et al.* High levels of exosomes expressing CD63 and caveolin-1 in plasma of melanoma patients. *PLoS One* **4**, (2009).

161. Melo, S. A. *et al.* Glypican-1 identifies cancer exosomes and detects early pancreatic cancer. (2015) doi:10.1038/nature14581.

162. Tian, Y. *et al.* Protein Profiling and Sizing of Extracellular Vesicles from Colorectal Cancer Patients via Flow Cytometry. *ACS Nano* **12**, 671–680 (2018).

163. Brown, M. J., Hallam, J. A., Colucci-Guyon, E. & Shaw, S. Rigidity of Circulating Lymphocytes Is Primarily Conferred by Vimentin Intermediate Filaments. *J. Immunol.* **166**, 6640–6646 (2001).

164. Collisson, E. A. *et al.* Comprehensive molecular profiling of lung adenocarcinoma: The cancer genome atlas research network. *Nature* **511**, 543–550 (2014).

165. Zhang, Y. L. *et al.* The prevalence of EGFR mutation in patients with non-small cell lung cancer: A systematic review and meta-analysis. *Oncotarget* **7**, 78985–78993 (2016).

166. Alix-Panabières, C. & Pantel, K. Clinical applications of circulating tumor cells and circulating tumor DNA as liquid biopsy. *Cancer Discov.* (2016) doi:10.1158/2159-8290.CD-15-1483.

167. Jahr, S. *et al.* DNA fragments in the blood plasma of cancer patients: Quantitations and evidence for their origin from apoptotic and necrotic cells. *Cancer Res.* **61**, 1659–1665 (2001).

168. Kustanovich, A., Schwartz, R., Peretz, T. & Grinshpun, A. Life and death of circulating cell-free DNA. *Cancer Biol. Ther.* **20**, 1057–1067 (2019).

169. Gauthier, V. J., Tyler, L. N. & Mannik, M. Blood clearance kinetics and liver uptake of mononucleosomes in mice. *J. Immunol.* **156**, 1151–6 (1996).

170. Lobb, R. J. *et al.* Exosomes derived from mesenchymal non-small cell lung cancer cells promote chemoresistance. *Int. J. Cancer* **141**, 614–620 (2017).

171. Chen, W. W. *et al.* Beaming and droplet digital pcr analysis of mutant idh1 mrna in glioma patient serum and cerebrospinal fluid extracellular vesicles. *Mol. Ther. - Nucleic Acids* **2**, e109 (2013).

172. Thakur, B. K. *et al.* Double-stranded DNA in exosomes: A novel biomarker in cancer detection. *Cell Res.* **24**, 766–769 (2014).

173. Figueroa, J. M. *et al.* Detection of wild-Type EGFR amplification and EGFRvIII mutation in CSF-derived extracellular vesicles of glioblastoma patients. *Neuro. Oncol.* **19**, 1494–1502 (2017).

174. Castellanos-Rizaldos, E. *et al.* Exosome-based detection of EGFR T790M in plasma from non–small cell lung cancer patients. *Clin. Cancer Res.* **24**, 2944–2950 (2018).

175. Krug, A. K. *et al.* Improved EGFR mutation detection using combined exosomal RNA and circulating tumor DNA in NSCLC patient plasma. *Ann. Oncol.* (2018) doi:10.1093/annonc/mdx765.

176. Dong, J. *et al.* Bio-Inspired NanoVilli Chips for Enhanced Capture of Tumor-Derived Extracellular Vesicles: Toward Non-Invasive Detection of Gene Alterations in Non-Small Cell Lung Cancer. *ACS Appl. Mater. Interfaces* **11**, 13973–13983 (2019).

177. Owen, S. *et al.* Simultaneous Single Cell Gene Expression and EGFR Mutation Analysis of Circulating Tumor Cells Reveals Distinct Phenotypes in NSCLC. *Adv. Biosyst.* **2000110**, 1–11 (2020).

178. Yoshioka, Y. *et al.* Comparative marker analysis of extracellular vesicles in different human cancer types. *J. Extracell. Vesicles* **2**, 1–9 (2013).

179. Rivero-Gutiérrez, B., Anzola, A., Martínez-Augustin, O. & De Medina, F. S. Stain-free detection as loading control alternative to Ponceau and housekeeping protein immunodetection in Western blotting. *Anal. Biochem.* **467**, 1–3 (2014).

180. Gilda, J. E. & Gomes, A. V. Stain-Free total protein staining is a superior loading control to b-actin for Western blots. *Anal. Biochem.* **440**, 186–188 (2013).

181. Kang, Y. T. *et al.* Multiplex isolation and profiling of extracellular vesicles using a microfluidic DICE device. *Analyst* **144**, 5785–5793 (2019).

182. Kang, Y. T. *et al.* Isolation and Profiling of Circulating Tumor-Associated Exosomes Using Extracellular Vesicular Lipid–Protein Binding Affinity Based Microfluidic Device. *Small* **15**, 1–14 (2019).

183. Li, M. *et al.* Analysis of the RNA content of the exosomes derived from blood serum and urine and its potential as biomarkers. *Philos. Trans. R. Soc. B Biol. Sci.* **369**, 20130502–20130502 (2014).

184. Neu, B., Wenby, R. & Meiselman, H. J. Effects of dextran molecular weight on red blood cell aggregation. *Biophys. J.* **95**, 3059–3065 (2008).

185. Ray, P. *et al.* Differential protein stability of EGFR mutants determines responsiveness to tyrosine kinase inhibitors. *Oncotarget* **19**, (2016).

186. Odogwu, L. *et al.* FDA Benefit-Risk Assessment of Osimertinib for the Treatment of Metastatic Non-Small Cell Lung Cancer Harboring Epidermal Growth Factor Receptor T790M Mutation. *Oncologist* **23**, 353–359 (2018).

187. Alix-Panabières, C. & Pantel, K. Clinical prospects of liquid biopsies. *Nat. Biomed. Eng.* **1**, (2017).

188. Reinert, T. *et al.* Analysis of circulating tumour DNA to monitor disease burden following colorectal cancer surgery. *Gut* **65**, 625–634 (2016).

189. Uchida, J. *et al.* Dynamics of circulating tumor DNA represented by the activating and resistant mutations in epidermal growth factor receptor tyrosine kinase inhibitor treatment. *Cancer Sci.* **107**, 353–358 (2016).

190. Théry, C. Exosomes: secreted vesicles and intercellular communications. *Biol. Reports* **33410**, 15–3 (2011).

191. Bracht, J. W. P., Mayo-de-Las-Casas, C., Berenguer, J., Karachaliou, N. & Rosell, R. The Present and Future of Liquid Biopsies in Non-Small Cell Lung Cancer: Combining Four Biosources for Diagnosis, Prognosis, Prediction, and Disease Monitoring. *Curr. Oncol. Rep.* **20**, 70 (2018).

192. Mathivanan, S. & Simpson, R. J. ExoCarta: A compendium of exosomal proteins and RNA. *Proteomics* **9**, 4997–5000 (2009).

193. Nicolazzo, C. *et al.* Monitoring PD-L1 positive circulating tumor cells in non-small cell lung cancer patients treated with the PD-1 inhibitor Nivolumab. *Sci. Rep.* **6**, 1–8 (2016).

194. Krebs, M. G. *et al.* Analysis of circulating tumor cells in patients with non-small cell lung cancer using epithelial marker-dependent and -independent approaches. *J. Thorac. Oncol.* **7**, 306–315 (2012).

195. Yoon, H. J. *et al.* Sensitive capture of circulating tumour cells by functionalized graphene oxide nanosheets. *Nat. Nanotechnol.* **8**, 735–41 (2013).

196. Nel, I., Jehn, U., Gauler, T. & Hoffmann, A. C. Individual profiling of circulating tumor cell composition in patients with non-small cell lung cancer receiving platinum based treatment. *Transl. Lung Cancer Res.* **3**, 100–106 (2014).

197. Kapeleris, J. *et al.* The prognostic role of circulating tumor cells (CTCs) in lung cancer. *Frontiers in Oncology* vol. 8 311 (2018).

198. Guibert, N. *et al.* Lung Cancer PD-L1 expression in circulating tumor cells of advanced non-small cell lung cancer patients treated with nivolumab ☆. *Lung Cancer* **120**, 108–112 (2018).

199. Wang, Y. *et al.* PD-L1 Expression in Circulating Tumor Cells Increases during Radio(chemo)therapy and Indicates Poor Prognosis in Non-small Cell Lung Cancer. *Sci. Rep.* **9**, 1–25 (2019).

200. Dorsey, J. F. *et al.* Tracking viable circulating tumor cells (CTCs) in the peripheral blood of non-small cell lung cancer (NSCLC) patients undergoing definitive radiation therapy: Pilot study results. *Cancer* **121**, 139–149 (2015).

201. Irizarry, R. A. *et al.* Exploration, normalization, and summaries of high density oligonucleotide array probe level data. *Biostatistics* **4**, 249–264 (2003).

202. Bertolini, G. *et al.* Highly tumorigenic lung cancer CD133+ cells display stem-like features and are spared by cisplatin treatment. *Proc. Natl. Acad. Sci.* **106**, 16281–16286 (2009).

203. Fu, L. *et al.* Incorporation of circulating tumor cells and whole-body metabolic tumor volume of 18F-FDG PET/CT improves prediction of outcome in IIIB stage small-cell lung cancer. *Chinese J. Cancer Res.* **30**, 596–604 (2018).

204. Oklu, R. *et al.* Relationship between hepatocellular carcinoma circulating tumor cells and tumor volume. *Cancer Converg.* **2**, 2 (2018).

205. Hristozova, T. *et al.* The presence of circulating tumor cells (CTCs) correlates with lymph node metastasis in nonresectable squamous cell carcinoma of the head and neck region (SCCHN). *Ann. Oncol.* **22**, 1878–1885 (2011).

206. Fitzgerald, J. E. *et al.* Heterogeneity of circulating tumor cell dissemination and lung metastases in a subcutaneous Lewis lung carcinoma model. *Biomed. Opt. Express* **11**, 3633 (2020).

207. Janning, M. *et al.* Determination of PD-L1 Expression in CirculatingTumor Cells of NSCLC Patients and Correlation withResponse to PD-1/PD-L1 Inhibitors. *Cancers (Basel).* **11**, 835 (2019).

208. Sánchez, A. & Villa, M. C. R. De. A Tutorial Review of Microarray Data Analysis. *Bioinformatics* 1–55 (2008).

209. Rani, A. & Murphy, J. J. STAT5 in Cancer and Immunity. *J. Interf. Cytokine Res.* **36**, 226–237 (2016).

210. Gu, L. *et al.* Stat5 promotes metastatic behavior of human prostate cancer cells in vitro and in vivo. *Endocr. Relat. Cancer* **17**, 481–493 (2010).

211. Bernaciak, T. M., Zareno, J., Parsons, J. T. & Silva, C. M. A novel role for signal transducer and activator of transcription 5b (STAT5b) in β1-integrin-mediated human breast cancer cell migration. *Breast Cancer Res.* **11**, R52 (2009).

212. Moser, C. *et al.* STAT5b as molecular target in pancreatic cancer-inhibition of tumor growth, angiogenesis, and metastases. *Neoplasia (United States)* **14**, 915–925 (2012).

213. Liu, Y. F. *et al.* Quantitative proteome analysis reveals annexin A3 as a novel biomarker in lung adenocarcinoma. *J. Pathol.* **217**, 54–64 (2009).

214. Cross, S. S., Hamdy, F. C., Deloulme, J. C. & Rehman, I. Expression of S100 proteins in normal human tissues and common cancers using tissue microarrays: S100A6, S100A8, S100A9 and S100A11 are all overexpressed in common cancers. *Histopathology* **46**, 256–269 (2005).

215. Wang, X. H. *et al.* Increased expression of S100A6 promotes cell proliferation in gastric cancer cells. *Oncol. Lett.* **13**, 222–230 (2017).

216. Komatsu, K. *et al.* Increased expression of S100A6 at the invading fronts of the primary lesion and liver metastasis in patients with colorectal adenocarcinoma. *Br. J. Cancer* **83**, 769–774 (2000).

217. Wang, X. *et al.* S100A12 is a promising biomarker in papillary thyroid cancer. *Sci. Rep.* **10**, 1–11 (2020).

218. Nasser, M. W., Elbaz, M., Ahirwar, D. K. & Ganju, R. K. Conditioning solid tumor microenvironment through inflammatory chemokines and S100 family proteins. *Cancer Letters* vol. 365 11–22 (2015).

219. Tzeng, H. T. & Wang, Y. C. Rab-mediated vesicle trafficking in cancer. *J. Biomed. Sci.* **23**, 1–7 (2016).

220. Li, X. *et al.* Effects of silencing Rab27a gene on biological characteristics and chemosensitivity of non-small cell lung cancer. *Oncotarget* **8**, 94481–94492 (2017).

221. An, H. J. *et al.* RAB27A is an independent prognostic factor in clear cell renal cell carcinoma. *Biomark. Med.* **13**, 239–247 (2019).

222. Wang, W., Jia, W. D., Hu, B. & Pan, Y. Y. RAB10 overexpression promotes tumor growth and indicates poor prognosis of hepatocellular carcinoma. *Oncotarget* **8**, 26434–26447 (2017).

223. He, H. *et al.* Identification and characterization of nine novel human small GTPases showing variable expressions in liver cancer tissues. *Gene Expr.* **10**, 231–242 (2002).

224. Gorges, T. M. *et al.* Enumeration and Molecular Characterization of Tumor Cells in Lung Cancer Patients Using a Novel In Vivo Device for Capturing Circulating Tumor Cells. *Clin. Cancer Res.* **22**, 2197–2206 (2016).

225. Ilié, M. *et al.* Detection of PD-L1 in circulating tumor cells and white blood cells from patients with advanced non-small-cell lung cancer. *Ann. Oncol.* **29**, 193–199 (2018).

226. Baccelli, I. *et al.* Identification of a population of blood circulating tumor cells from breast cancer patients that initiates metastasis in a xenograft assay. *Nat. Biotechnol.* **31**, 539–544 (2013).

227. Topalian, S. L., Drake, C. G. & Pardoll, D. M. Targeting the PD-1/B7-H1(PD-L1) pathway to activate anti-tumor immunity. *Current Opinion in Immunology* vol. 24 207–212 (2012).

228. Lian, S. *et al.* Dual blockage of both PD-L1 and CD47 enhances immunotherapy against circulating tumor cells. *Sci. Rep.* **9**, 1–7 (2019).

229. Papalexi, E. & Satija, R. Single-cell RNA sequencing to explore immune cell heterogeneity. *Nat. Publ. Gr.* **18**, (2017).

230. Stewart, C. A. *et al.* Single-cell analyses reveal increased intratumoral heterogeneity after the onset of therapy resistance in small-cell lung cancer. *Nat. Cancer* **1**, 423–436 (2020).

231. Gross, A. *et al.* Technologies for Single-Cell Isolation. *Int. J. Mol. Sci.* **16**, 16897–16919 (2015).

232. Hu, P., Zhang, W., Xin, H. & Deng, G. Single cell isolation and analysis. *Frontiers in Cell and Developmental Biology* vol. 4 116 (2016).

233. Basu, S., Campbell, H. M., Dittel, B. N. & Ray, A. Purification of specific cell population by fluorescence activated cell sorting (FACS). *J. Vis. Exp.* 1546 (2010) doi:10.3791/1546.

234. Hines, W. C., Su, Y., Kuhn, I., Polyak, K. & Bissell, M. J. Commentary Sorting Out the FACS: A Devil in the Details. (2014) doi:10.1016/j.celrep.2014.02.021.

235. Miltenyi, S., Müller, W., Weichel, W. & Radbruch, A. High gradient magnetic cell separation with MACS. *Cytometry* **11**, 231–238 (1990).

236. Sutermaster, B. A. & Darling, E. M. Considerations for high-yield, high-throughput cell enrichment: fluorescence versus magnetic sorting. *Sci. Rep.* **9**, 1–9 (2019).

237. Chen, Y. *et al.* Rare cell isolation and analysis in microfluidics. *Lab on a Chip* vol. 14 626–645 (2014).

238. Wyatt Shields Iv, C., Reyes, C. D. & López, G. P. Microfluidic cell sorting: A review of the advances in the separation of cells from debulking to rare cell isolation. *Lab Chip* **15**, 1230–1249 (2015).

239. Di Trapani, M., Manaresi, N. & Medoro, G. DEPArray™ system: An automatic image-based sorter for isolation of pure circulating tumor cells. *Cytom. Part A* **93**, 1260–1266 (2018).

240. Lee, J. W., Shin, J. Y. & Seo, J. S. Identification of novel mutations in FFPE lung adenocarcinomas using DEPArray sorting technology and next-generation sequencing. *J. Appl. Genet.* **59**, 269–277 (2018).

241. Williamson, V. R., Laris, T. M., Romano, R. & Marciano, M. A. Enhanced DNA mixture deconvolution of sexual offense samples using the DEPArray™ system. *Forensic Sci. Int. Genet.* **34**, 265–276 (2018).

242. Unger, M. A., Chou, H. P., Thorsen, T., Scherer, A. & Quake, S. R. Monolithic microfabricated valves and pumps by multilayer soft lithography. *Science (80-.).* **288**, 113–116 (2000).

243. Lecault, V. *et al.* High-throughput analysis of single hematopoietic stem cell proliferation in microfluidic cell culture arrays. *Nat. Methods* **8**, 581–589 (2011).

244. Fan, H. C., Wang, J., Potanina, A. & Quake, S. R. Whole-genome molecular haplotyping of single cells. *Nat. Biotechnol.* **29**, 51–59 (2011).

245. Weinstein, J. A., Jiang, N., White, R. A., Fisher, D. S. & Quake, S. R. High-throughput sequencing of the zebrafish antibody repertoire. *Science (80-.).* **324**, 807–810 (2009).

246. Mazutis, L. *et al.* Single-cell analysis and sorting using droplet-based microfluidics. *Nat. Protoc.* **8**, 870–891 (2013).

247. Huang, L. R., Cox, E. C., Austin, R. H. & Sturm, J. C. Continuous Particle Separation Through Deterministic Lateral Displacement. *Science (80-.).* **304**, 987–990 (2004).

248. Salafi, T., Zhang, Y. & Zhang, Y. A Review on Deterministic Lateral Displacement for Particle Separation and Detection. *Nano-Micro Letters* vol. 11 3 (2019).

249. Lagus, T. P. & Edd, J. F. A review of the theory, methods and recent applications of high-throughput single-cell droplet microfluidics. *Journal of Physics D: Applied Physics* vol. 46 114005 (2013).

250. Matuła, K., Rivello, F. & Huck, W. T. S. Single-Cell Analysis Using Droplet Microfluidics. *Adv. Biosyst.* **4**, 1900188 (2020).

251. Debs, B. El, Utharala, R., Balyasnikova, I. V., Griffiths, A. D. & Merten, C. A. Functional single-cell hybridoma screening using droplet-based microfluidics. *Proc. Natl. Acad. Sci. U. S. A.* **109**, 11570–11575 (2012).

252. DeKosky, B. J. *et al.* In-depth determination and analysis of the human paired heavy- and light-chain antibody repertoire. *Nat. Med.* **21**, 86–91 (2015).

253. Coombe, L. *et al.* Assembly of the Complete Sitka Spruce Chloroplast Genome Using 10X Genomics' GemCode Sequencing Data. *PLoS One* **11**, e0163059 (2016).

254. Wang, X., He, Y., Zhang, Q., Ren, X. & Zhang, Z. Direct Comparative Analyses of 10X Genomics Chromium and Smart-seq2. *Genomics. Proteomics Bioinformatics* (2021) doi:10.1016/j.gpb.2020.02.005.

255. Wu, L., Chen, P., Dong, Y., Feng, X. & Liu, B. F. Encapsulation of single cells on a microfluidic device integrating droplet generation with fluorescence-activated droplet sorting. *Biomed. Microdevices* **15**, 553–560 (2013).

256. Dobson, C., Zielke, C., Pan, C., Feit, C. & Abbyad, P. Method for Passive Droplet Sorting after Photo-Tagging. *Micromachines* **11**, 964 (2020).

257. Xi, H.-D. *et al.* Featuring the collaborative work between Active droplet sorting in microfluidics: a review. *Lab Chip* **17**, 751 (2017).

258. Payne, E. M., Holland-Moritz, D. A., Sun, S. & Kennedy, R. T. High-throughput screening by droplet microfluidics: Perspective into key challenges and future prospects. *Lab on a Chip* vol. 20 2247–2262 (2020).

259. Jack, R. M. *et al.* Ultra-Specific Isolation of Circulating Tumor Cells Enables Rare-Cell RNA Profiling. *Adv. Sci.* **3**, 1–8 (2016).

260. Hoshino, K., Chen, P., Huang, Y. Y. & Zhang, X. Computational analysis of microfluidic immunomagnetic rare cell separation from a particulate blood flow. *Anal. Chem.* **84**, 4292–4299 (2012).

261. Doonan, S. R., Lin, M. & Bailey, R. C. Droplet CAR-Wash: Continuous picoliter-scale immunocapture and washing. *Lab Chip* **19**, 1589–1598 (2019).

262. Vivier, E., Nunès, J. A. & Vély, F. Natural killer cell signaling pathways. *Science* vol. 306 1517–1519 (2004).

263. Lugini, L. *et al.* Immune Surveillance Properties of Human NK Cell-Derived Exosomes. *J. Immunol.* **189**, 2833–2842 (2012).

264. Van Niel, G., D'Angelo, G. & Raposo, G. Shedding light on the cell biology of extracellular vesicles. *Nat. Rev. Mol. Cell Biol.* (2018) doi:10.1038/nrm.2017.125.

265. Chen, Y., Lu, D., Churov, A. & Fu, R. Research Progress on NK Cell Receptors and Their Signaling Pathways. *Mediators of Inflammation* vol. 2020 (2020).

266. Hu, W., Wang, G., Huang, D., Sui, M. & Xu, Y. Cancer immunotherapy based on natural killer cells: Current progress and new opportunities. *Frontiers in Immunology* vol. 10

1205 (2019).

267. Federici, C. *et al.* Natural-Killer-Derived Extracellular Vesicles: Immune Sensors and Interactors. *Front. Immunol.* **11**, 262 (2020).

268. Li, L., Jay, S. M., Wang, Y., Wu, S. W. & Xiao, Z. IL-12 stimulates CTLs to secrete exosomes capable of activating bystander CD8+ T cells. *Sci. Rep.* **7**, 1–10 (2017).

269. Colombo, M., Raposo, G. & Théry, C. Biogenesis, Secretion, and Intercellular Interactions of Exosomes and Other Extracellular Vesicles. *Annu. Rev. Cell Dev. Biol* **30**, 255–89 (2014).

270. Blanchard, N. *et al.* TCR Activation of Human T Cells Induces the Production of Exosomes Bearing the TCR/CD3/ζ Complex. *J. Immunol.* **168**, 3235–3241 (2002).

271. Muntasell, A., Berger, A. C. & Roche, P. A. T cell-induced secretion of MHC class II-peptide complexes on B cell exosomes. *EMBO J.* **26**, 4263–4272 (2007).

272. Zwirner, N. W. & Ziblat, A. Regulation of NK cell activation and effector functions by the IL-12 family of cytokines: The case of IL-27. *Frontiers in Immunology* vol. 8 25 (2017).

273. Jack, R. *et al.* Microfluidic continuum sorting of sub-populations of tumor cells via surface antibody expression levels. *Lab Chip* **17**, 1349–1358 (2017).

274. Derec, C., Claire, A. E., Ae, W., Servais, J. & Bacri, J.-C. Local control of magnetic objects in microfluidic channels. doi:10.1007/s10404-009-0486-6.

275. Kokkinis, G., Keplinger, F. & Giouroudi, I. On-chip microfluidic biosensor using superparamagnetic microparticles. doi:10.1063/1.4826546.

276. Schneider, T. *et al.* Sequential CD34 cell fractionation by magnetophoresis in a magnetic dipole flow sorter †. (2009) doi:10.1039/b908210g.

277. Joshi, B. S., De Beer, M. A., Giepmans, B. N. G. & Zuhorn, I. S. Endocytosis of Extracellular Vesicles and Release of Their Cargo from Endosomes. *ACS Nano* **14**, 4455 (2020).

278. Mozzoni, P. *et al.* Plasma and EBC microRNAs as early biomarkers of non-small-cell lung cancer. *Biomarkers Biochem. Indic. Expo. response, susceptibility to Chem.* **18**, 679–686 (2013).

279. Meinhardt, K. *et al.* Influence of NK cell magnetic bead isolation methods on phenotype and function of murine NK cells. *J. Immunol. Methods* **378**, 1–10 (2012).

280. Heimberger, A. B. *et al.* Prognostic effect of epidermal growth factor receptor and EGFRvIII in glioblastoma multiforme patients. *Clin. Cancer Res.* **11**, 1462–1466 (2005).

281. Quan, P. L., Sauzade, M. & Brouzes, E. DPCR: A technology review. *Sensors*

(Switzerland) vol. 18 (2018).

282. Berthier, E., Young, E. W. K. & Beebe, D. Engineers are from PDMS-land, biologists are from polystyrenia. *Lab on a Chip* vol. 12 1224–1237 (2012).

283. Brunyé, T. T., Mercan, E., Weaver, D. L. & Elmore, J. G. Accuracy is in the eyes of the pathologist: The visual interpretive process and diagnostic accuracy with digital whole slide images. *J. Biomed. Inform.* **66**, 171–179 (2017).

284. Lannin, T. B., Thege, F. I. & Kirby, B. J. Comparison and optimization of machine learning methods for automated classification of circulating tumor cells. *Cytom. Part A* **89**, 922–931 (2016).

285. Svensson, C. M., Krusekopf, S., Lücke, J. & Thilo Figge, M. Automated detection of circulating tumor cells with naive Bayesian classifiers. *Cytom. Part A* **85**, 501–511 (2014).

286. Angelo, L. S. *et al.* Practical NK cell phenotyping and variability in healthy adults. *Immunol. Res.* **62**, 341–356 (2015).

287. Sivori, S. *et al.* TLR/NCR/KIR: Which one to use and when? *Frontiers in Immunology* vol. 5 105 (2014).

288. Reclusa, P. *et al.* Improving extracellular vesicles visualization: From static to motion. *Sci. Rep.* **10**, (2020).

289. Cheng, L., Sun, X., Scicluna, B. J., Coleman, B. M. & Hill, A. F. Characterization and deep sequencing analysis of exosomal and non-exosomal miRNA in human urine. *Kidney Int.* **86**, 433–444 (2013).

290. Son, K. J. *et al.* Microfluidic compartments with sensing microbeads for dynamic monitoring of cytokine and exosome release from single cells. *Analyst* **141**, 679–688 (2016).

291. Abate, A. R., Hung, T., Marya, P., Agresti, J. J. & Weitz, D. A. High-throughput injection with microfluidics using picoinjectors using picoinjectors. *Proc. Natl. Acad. Sci. U. S. A.* **107**, 19163–19166 (2010).

292. Sjostrom, S. L., Joensson, H. N. & Svahn, H. A. Multiplex analysis of enzyme kinetics and inhibition by droplet microfluidics using picoinjectors. *Lab Chip* **13**, 1754–1761 (2013).

293. Doonan, S. R. & Bailey, R. C. K-Channel: A Multifunctional Architecture for Dynamically Reconfigurable Sample Processing in Droplet Microfluidics. *Anal. Chem.* **89**, 4091–4099 (2017).